

- 
- 1 - Using short-period surface waves to study seismic source and structure.
  - 2 - Source complexity of large strike-slip earthquakes.

Thesis by  
Hong Kie Thio

In Partial Fulfillment of the Requirements  
for the Degree of  
Doctor of Philosophy

California Institute of Technology  
Pasadena, California  
1996  
(Submitted June 16, 1995)

---

---

© 1996  
Hong Kie Thio  
All rights reserved

---

## Acknowledgments

First and foremost I would like to thank my advisor, Hiroo Kanamori, for his support, patience and tolerance during my entire stay at the Caltech Seismo Lab. I feel very privileged to have worked with him and thanks to him I have always felt at home at the Lab. I can think of no better person to instill an enthusiasm in seismology, or science in general, in a person than him.

I enjoyed working and talking with Toshiro Tanimoto, and wish we could have shared more time together at the Seismo Lab. Don Helmberger was always ready to give advice, ideas or to cheer me up.

Rob Clayton was an ideal academic advisor and I enjoyed talking and listening (primarily the latter) to him and the other faculty members, all of whom I respect and whose presence I have enjoyed. I have always been impressed how Dave Harkrider could enliven seismology with tales of deceased seismologists, and the diseases that eventually did them in.

I greatly enjoyed and appreciated the help of, and collaboration with, Dr. Masayuki Kikuchi and Dr. Kenji Satake.

The timers of the Southern California Seismic Network were always ready to share their work with me and have always been very helpful.

David Wald was the first fellow student that I encountered after I arrived in Pasadena, and has remained a very good friend since. I thank him and Lisa for their friendship and hospitality, which endured despite my slight "European" attitude, and despite showing up real late at Thanksgiving.

Joanne Yoshimura, Doug Dreger, Brad Woods, Helen Qian and Yushen Zhang helped me survive my first year, both in the class-room and outside. Cathy and Andrea introduced me to those remote and unknown parts of Southern California, some of which were real gems, others not, and I thank Sharon for showing me on of those occasions how to teach a baby-raccoon table manners.

---

Craig, Paul, Shingo and Blair were great friends and lunch and movie companions, and were always ready to help. Many more people have contributed to my well-being here in Southern California and thanks to them, I have come to appreciate Southern California very much.

My parents and family have always been supportive, in many different ways, of my exploits as professional student. I thank my aunt Yvonne (tante Bobo) for her enthusiastic moral and material support.

The great burden of living with an eternal student trying to graduate was carried by Jascha, who brought joy to my life in a way I could never have foreseen before. I thank her for that, and for her tremendous help in reaching the end of my studies.

I dedicate this thesis to her and to my parents.

---

## Abstract

The availability of high dynamic range very broad band seismic data in recent years has greatly increased the level of detail and the speed with which we can study the seismic source. The work presented in this thesis draws heavily on the deployment of broad-band seismometers, both on a worldwide scale, with networks like IRIS, IRIS/IDA and GEOSCOPE, as well as on a local scale, using data from the TERRAScope network.

The routine study of seismicity in Southern California, like in other seismically active regions, has traditionally been carried out using dense arrays of high-gain short-period seismometers. With the addition of the very broad band instrumentation of TERRAScope we can improve this pursuit in several ways, one of which being the use of short period surface waves to study local earthquakes as described in chapter 1 of this thesis. Over the years, surface waves have proved to be very reliable and stable for moment tensor inversions. The method is very rapid, and because of the longer periods used they are more reliable for consistent estimation of earthquake moment. At short distances the surface waves arrive within a few minutes after an event has occurred at the stations, and with real-time telemetry we can obtain the size and mechanism for local earthquakes within minutes. The propagation corrections for surface waves are very straightforward so that this procedure can be made completely automatic. Armed with the results from above procedure, we can determine travel time residuals for a dense distribution of raypaths across Southern California. In chapter 2 we present tomographic inversions of these residuals, for Love and Rayleigh waves at periods between 10 and 50 seconds. The results indicate that lateral variations of phase velocity of up to 10% exist in the area, and that these anomalies can have relatively short wavelengths.

The 1994 Northridge earthquake provided a wealth of data to apply our moment tensor inversion to, and in chapter 3 we present a detailed analysis of the aftershock mechanisms

---

in relation to the source complexity of the mainshock. We show that the orientation of the aftershock mechanisms changes away from the zone where rupture took place. We suggest that this change in mechanism reflects changes in fault geometry which have limited the extent of the Northridge rupture, leading to a high static stress drop.

The issue of source complexity is discussed further in chapter 4, where we present a systematic study of the rupture of three large strike-slip earthquakes and compare these results with observation on the surface rupture. We find a very good correlation which suggests that the source complexity can be attributed to fault geometry, which tends to become simpler as slip accumulates along a fault. This provides an explanation for the high stress drops that are observed for earthquakes which occur along faults with low strain rates.

Finally, in chapter 5 we compiled energy and moment estimates for earthquakes in Southern California, based on the results in the previous chapters. We find that the radiated seismic energy is not linearly related to the seismic moment, but that instead the energy-moment ratio increases as a function of moment. We provide some suggestions as to the cause of this relationship, including a moment dependence of the specific fracture energy and a non-similarity of the frictional stress between different size earthquakes.

---

---

## Table of contents:

<b>Acknowledgments</b>	<b>iii</b>
<b>Abstract</b>	<b>v</b>
<b>Table of contents</b>	<b>vii</b>
<b>Chapter 1 - Moment tensor inversions for local earthquakes using surface waves recorded at TERRAScope</b>	<b>1</b>
<b>Chapter 2 - Lateral variation of surface wave velocities in Southern California</b>	<b>26</b>
<b>Chapter 3 - Source complexity of the January 1994 Northridge earthquake and its relation with aftershock mechanisms</b>	<b>33</b>
<b>Chapter 4 - Source complexity of large strike-slip earthquakes: the 1990 Rudbar (Iran), Luzon (Philippines) and 1992 Landers (California) earthquakes</b>	<b>50</b>
<b>Chapter 5 - A short note on earthquake energy</b>	<b>82</b>
<b>Appendix A - Moment tensor solutions for the years 1990 to 1995</b>	<b>94</b>
<b>Appendix B - Maps of lateral phase velocity variations in Southern California</b>	<b>103</b>

## List of figures:

### Chapter 1

---

1.	<b>Map of Southern California.</b>	<b>2</b>
2.	Rayleigh wave excitation functions.	5
3.	Velocity models.	6
4.	Dispersion curves.	7
5.	Regionalized velocity model.	8
6.	Dispersion curves for the subregions.	9
7.	Comparison of data and synthetic seismograms.	10
8.	Variation of the solution with depth.	11-12
9.	Moment tensor solution	14
10.	Comparison of moment tensors and fist motions.	16
11.	Solutions for the Joshua Tree sequence.	18
12.	Solutions for the Landers sequence.	18-19
13.	Relation between $M_L$ and $M_0$	20
<b>Chapter 2</b>		
1.	Path coverage	28
2.	Travel-time residuals for Rayleigh waves	29
3.	Travel-time residuals for Love waves.	30
4.	Examples of lateral phase velocity variations.	31
<b>Chapter 3</b>		
1.	Map of Southern California.	35
2.	Stations distribution.	36
3.	P-wave recorded at NNA (Chile).	37
4.	Source-time function and mechanisms after the	

---

---

	first inversion.	38
5.	Data and synthetic seismograms.	39
6.	Final source-time function and mechanism.	40
7.	Data and synthetic seismograms.	41
8.	Cross-section through the Northridge aftershock zone.	41
9.	Moment tensor solution for the Northridge earthquake.	43
10.	Aftershock mechanisms.	44
11.	Variation of $M_L$ and $M_0$ .	45
<b>Chapter 4</b>		
1.	Locations of the earthquakes.	52
2.	Azimuthal station distributions.	54
3.	Map of NW Iran.	56
4.	Distribution of subevents.	57
5.	Source-time function for the Rudbar earthquake.	58
6.	Data and synthetic seismograms.	59
7.	Map of Central Luzon.	61
8.	Comparison of main-, and aftershock waveforms.	63
9.	Data and synthetic seismograms.	64
10.	Source-time function for the Luzon earthquake.	65
11.	Map of the Landers area.	67
12.	Data and synthetic seismograms.	67
13.	Source-time function for the Landers earthquake.	68
14.	Energy vs. moment.	71

---

---

15.	Relation between moment, rupture length and repeat time.	74
<b>Chapter 5</b>		
1.	Moment vs. radiated energy.	85
2.	Moment vs. energy for Mexican events.	87
3.	Crack energy.	88
4.	Energy diagrams for crack energy.	89
5.	Energy diagrams for variable frictional stress.	90
 <b>List of tables:</b>		
<b>Chapter 1</b>		
1.	TERRAscope stations	2
2.	Sierra Madre earthquake.	17
3.	Joshua Tree earthquake.	17
4.	Big Bear earthquake.	17
<b>Chapter 3</b>		
1.	Velocity model.	37
<b>Chapter 4</b>		
1.	Source parameters for the Rudbar subevents.	58
2.	Source parameters for the Rudbar mainshock and largest aftershock.	60
3.	Source parameters for the Luzon mainshock and aftershocks.	64
4.	Subevents of the Luzon mainshock.	66
5.	Subevents for the Landers mainshock.	69

---

<b>6.</b>	Source parameters for Landers mainshock.	<b>69</b>
<b>7.</b>	Energy and stress drops for the Rudbar earthquake.	<b>72</b>

## Chapter 1:

# Moment tensor inversions for local earthquakes using surface waves recorded at TERRAScope

### Abstract

We have developed a method to determine moment tensors for local earthquakes using short-period (10-50 sec.) surface waves recorded at TERRAScope stations. To correct for the substantial lateral variations in crustal structure, we applied phase corrections to the data using a regionalized phase velocity model. We have determined moment tensors for over 180 events in the last three years in Southern California for magnitudes as small as 3.2 and as large as 6.5. The results are consistent with those obtained from first-motion data as well as other waveform inversions. When continuous data telemetry from the stations becomes available this method can yield moment-tensors for earthquakes in Southern California and adjacent regions within minutes after the occurrence of an event.

Our results confirm the relation  $\log M_0$  (seismic moment)  $\propto 1.5 M_L$  (local magnitude) obtained by an earlier study.

### Introduction

With the deployment of dense digital broad-band networks like TERRAScope, we are now capable of carrying out rapid determinations of source parameters using a variety of methods. In this paper we present one such method, viz. moment tensor inversion using regional surface-waves. The advantage of this method over others using body-waves is that it is very rapid and does not require manual intervention, so that it can be made into an

---

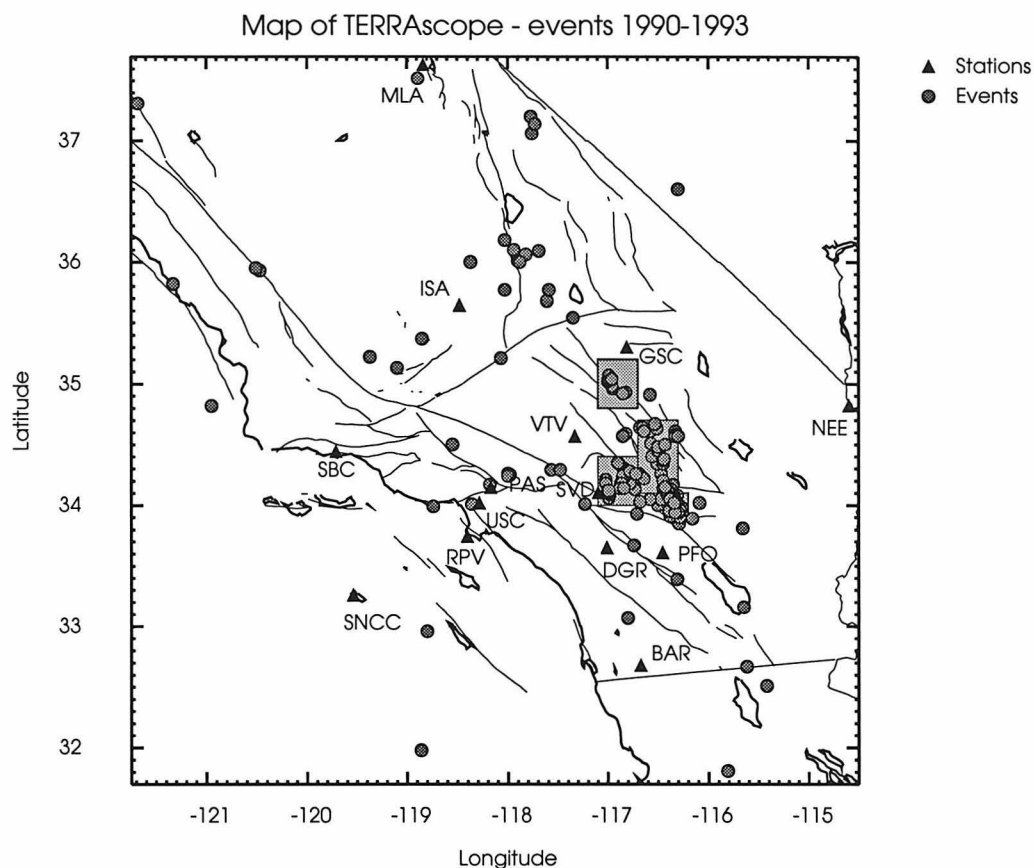


Figure 1. Map of Southern California with the location of events included in this study and the stations of the TERRAScope network. The shaded blocks represent aftershock zones of the 1992 Joshua Tree and Landers-Big Bear earthquakes and are blown-up in figures 11 and 12.

TERRAScope stations			
Station	Latitude	Longitude	Type
PAS	34.148	-118.172	STS-1
GSC	35.300	-116.810	STS-1
ISA	35.643	-118.480	STS-1
PFO	33.609	-116.455	STS-1
SBC	34.442	-119.713	STS-1
BAR	32.680	-116.672	STS-1
NEE	34.823	-114.596	STS-2
MLA	37.634	-118.838	STS-2
USC	34.019	-118.286	STS-2
SVD	34.104	-117.098	STS-2
VTV	34.567	-117.333	STS-2
RPV	33.744	-118.403	STS-2
DGR	33.650	-117.009	STS-2
SNCC	33.248	-119.524	STS-1

Table 1. List of TERRAScope stations used in this study. All stations are equipped with Streckeisen instruments (STS-1 or STS-2) as well as CMG-1 strong motion accelerographs.

---

automatic process suitable for real-time purposes. Real-time analysis of earthquakes can be very important, since it can help us estimate the damage after an earthquake even before reports from the field come in, potentially increasing the efficiency of rescue operations. Knowledge of the mechanism also helps us to determine on which fault the earthquake occurred, which is important for the analysis of short-term seismic hazard.

We can analyze smaller events better with surface waves, since body-waves, with their shorter periods, tend to be more contaminated with noise than surface waves. Surface waves have already been used successfully in the determination of source parameters of earthquakes (e.g. Aki, 1966; Mendiguren, 1977; Kanamori & Given, 1981; Dziewonski & Woodhouse, 1983; Romanowicz and Monfret, 1986; Patton, 1980). In general, they are used to study larger earthquakes since these events generate sufficiently large surface waves at longer periods. The use of shorter periods ( $< 50$  seconds) was hampered by the fact that these waves are sensitive to lateral inhomogeneity in the earth's velocity structure and are therefore difficult to model over large distances. On the other hand, local arrays which are used to study smaller earthquakes in seismically active regions usually do not have sufficiently long-period response to record even short-period surface waves. Regional broad-band networks like TERRAScope (fig. 1, table 1) enable us to use these methods to their fullest advantage even for smaller earthquakes (Romanowicz et al., 1993; Patton & Zandt, 1991, Ritsema and Lay, 1993).

Since the spring of 1992 we have had a prototype of this system in operation at the Caltech Seismo Lab and we now routinely analyze events with magnitude larger than 3.2 in Southern California. In this paper we discuss the inversion method and its implementation; we will show results for local earthquakes and compare them with results from first motion and body-wave studies.

---

## Theory

Moment tensor inversions using surface waves are carried out either in the frequency domain (Mendiguren, 1977; Kanamori & Given, 1981; Romanowicz & Monfret, 1986) or in the time domain (Dziewonski & Woodhouse, 1983; Kawakatsu, 1989). The latter method includes the higher modes, which give additional constraints on the mechanism and especially the depth of deep events. The spectral method only uses fundamental mode surface waves, but since these dominate the waveforms this is not regarded as a severe drawback. In this case the inverse problem becomes particularly simple and straightforward as described by Kanamori & Given (1981), henceforth to be referred to as K&G. The method we used closely follows their paper and we refer to that paper for the formulations and derivations. In essence, we take the complex spectrum of the surface waves at various stations, and correct them for propagation effects. We can write the corrected spectrum,  $V(w)$ , as a linear combination of the moment tensor elements, for Rayleigh waves:

$$V_R(\omega) = -P_R \left[ M_{xy} \sin 2\varphi - \frac{1}{2}(M_{yy} - M_{xx}) \cos 2\varphi \right] - \frac{1}{2}S_R(M_{yy} + M_{xx}) \\ + iQ_R(M_{yz} \sin \varphi + M_{xz} \cos \varphi)$$

(K&G eq. 5) and for Love waves:

$$V_L = P_L \left[ \frac{1}{2}(M_{xx} - M_{yy}) \sin 2\varphi - M_{xy} \cos 2\varphi \right] + iQ_L \left[ -M_{xz} \sin \varphi + M_{yz} \cos \varphi \right]$$

(K&G eq. 14).

$V_{L,R}$  are the corrected spectra (at the source),  $P_{L,R}$ ,  $Q_{L,R}$ ,  $S_R$  are the excitation functions (see also fig. 2) and  $\varphi$  the azimuth to the station measured from the fault strike. We obtain the

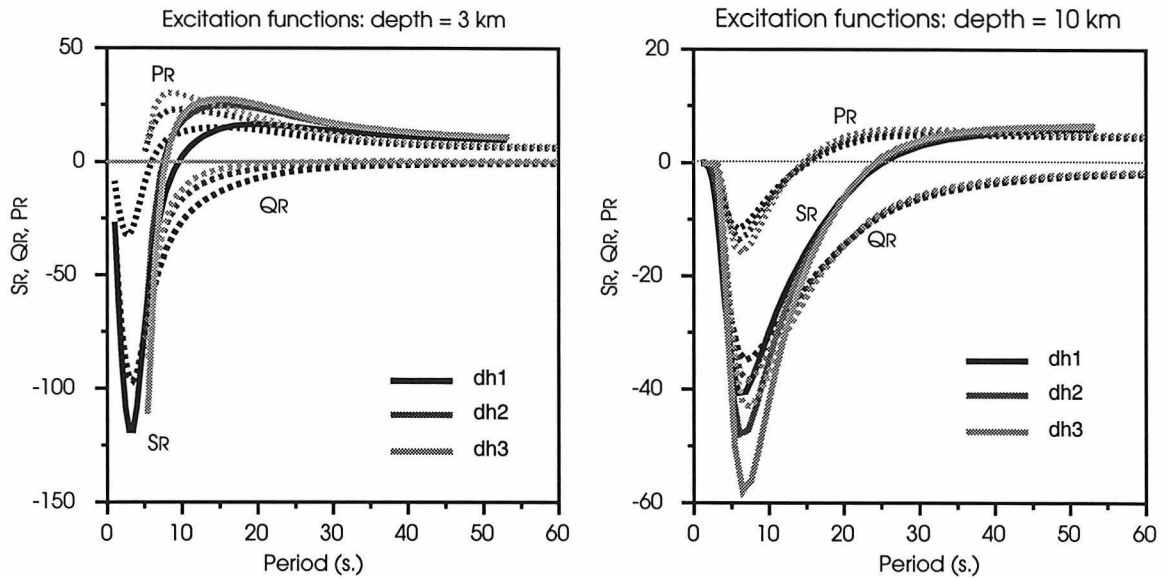


Figure 2. Rayleigh wave excitation functions calculated for three velocity models (fig. 3). The functions have been calculated for (a) a depth of three kilometers and (b) a depth of ten kilometers.

moment tensor by solving:

$$\mathbf{A}\mathbf{m} = \mathbf{v}$$

(K&G eq. 7) in the least squares sense. Here  $\mathbf{A}$  is a matrix containing the excitation functions and the azimuthal ( $\varphi$ ) terms, for the different frequencies,  $\mathbf{m}$  is a vector containing the moment tensor elements  $M_{ij}$  and  $\mathbf{v}$  a vector containing the real and imaginary parts of the spectral data,  $V_{L,R}$ .

To reduce the noise, both instrumental and from higher modes, we apply a group-velocity window (between 2.5 and 4.5 km/s) to the data before the Fourier transformation. In the frequency domain we then pick the spectrum at four or five periods between 10 and 50 seconds for the inversion. At periods shorter than 10 seconds the influence of lateral inhomogeneity and body-wave phases becomes too large. For small events there is very little energy at periods longer than 30 seconds, so that for routine purposes we use this period interval. However, if the need arises in case of a large event, we can always extend this period range upward.

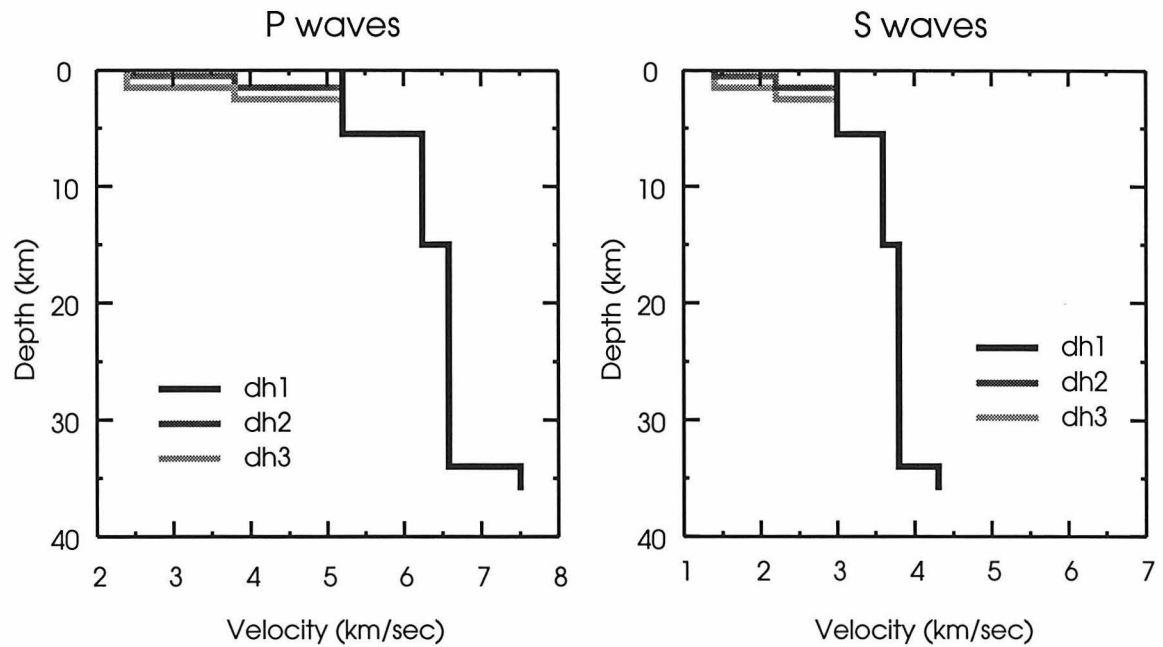


Figure 3. Velocity models (a- P waves, b- S waves) used to calculate the excitation functions (fig. 2) and the dispersion curves of fig. 4. The difference between the models is in the upper three kilometers where dh1 has no slow layers whereas dh2 and dh3 have low velocity layers with increasing thickness.

This method is valid if the source dimension and duration are small compared with the epicentral distance and the period of the surface wave, respectively. The source duration for events smaller than  $M_w = 6$  is usually much smaller than the periods of the surface waves used in this inversion; we use a duration of 1 second for routine processing. For larger events, we can either increase the source duration or the periods we use. If the source dimensions become very large, simple time-corrections are not valid anymore and we would have to take directivity effects into account as well. If the stations are very close to the earthquake the point-source approximation is also violated, but including finite rupture dimensions would necessitate some major changes of the method.

Although it is evident that there is strong lateral inhomogeneity in Southern California, we use a single set of eigenfunctions to calculate the excitation functions. Changes in velocity model have only second order effects on the eigenfunctions; the lateral inhomogeneity, as we shall see later, is concentrated in the upper 4 to 5 kilometers of the crust, whereas many earthquakes occur at larger depths. In figure 2 we present excitation functions calculated

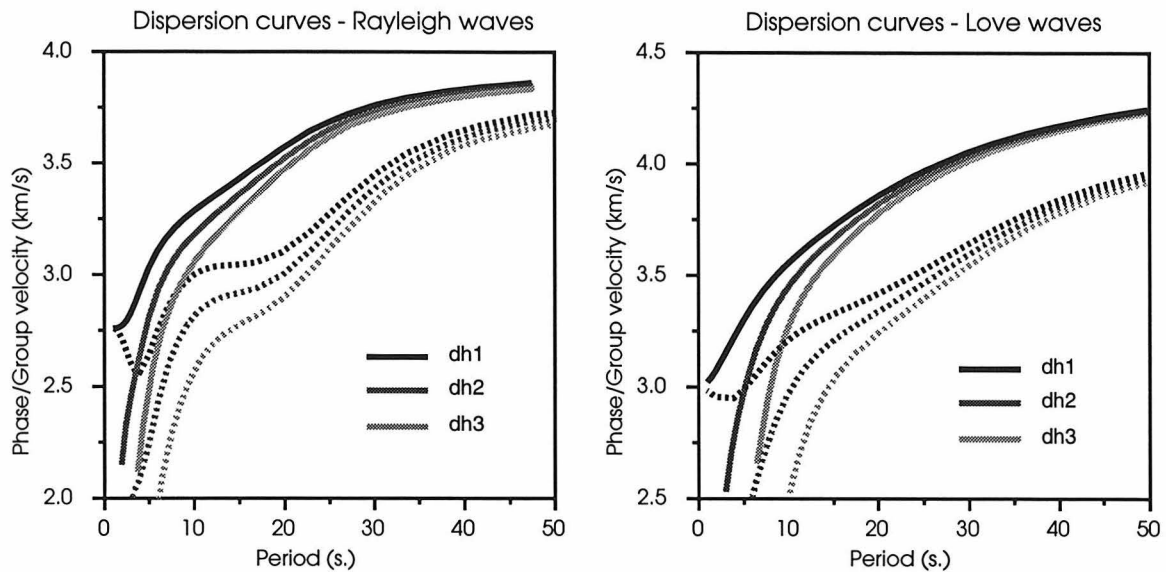


Figure 4. Dispersion curves for the velocity models in fig. 3. Both phase (solid lines) and group (dashed lines) velocities are plotted for (a) Rayleigh waves and (b) Love waves.

for three crustal models (fig. 3) which are only different from each other in the upper three kilometers. It is clear that for events at a depth of 10 km the difference is marginal, especially at periods longer than 15 seconds, whereas for a depth of 3 km the difference in amplitude is more substantial. However, the shape of the excitation functions and the location of the zero crossings, which are important in determining the mechanisms and depth are not very different for any depth. Therefore, we only expect the moment for shallow events to be influenced by our use of a single crustal model. This conclusion has been substantiated by running some inversions with the different crustal models.

As the phase velocities are very different for the 3 different crustal structures (fig. 4), we do have to include a phase correction based on a laterally inhomogeneous (phase) velocity model.

### Velocity model

We constructed a preliminary velocity model for Southern California by analyzing some of

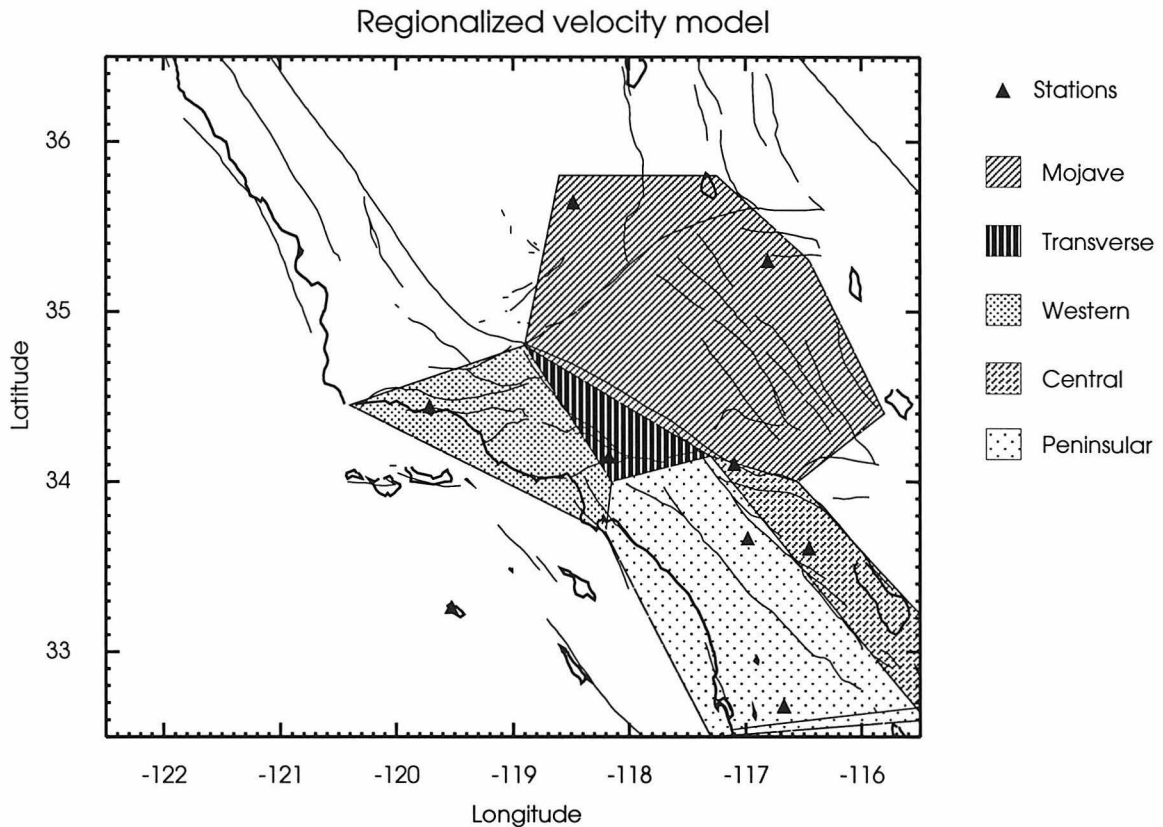


Figure 5. Regionalized velocity model for Southern California. The labels correspond to the dispersion curves in fig. 6.

the larger local events for which well-constrained mechanism solutions are available. We calculated the source phase for these events and subtracted it from the phase of the surface waves at the stations. The phase velocity was then determined by using:

$$c(T) = \frac{\Delta}{(\varphi_1 - \varphi_s + 2n\pi)T}$$

where  $T$  is the period,  $\varphi_1$ , data phase,  $\varphi_s$ , the source phase,  $\Delta$  the distance and  $n$  an integer. The value for  $n$  was chosen at longer periods assuming that the phase velocities determined here are close to some model phase velocities.

On the basis of the velocity curves thus obtained for every path, we divided Southern California into five regions (fig. 5) with distinct dispersion curves (fig 6). This regionalized model is used to correct the phase of the data for the propagation delay. An example of this

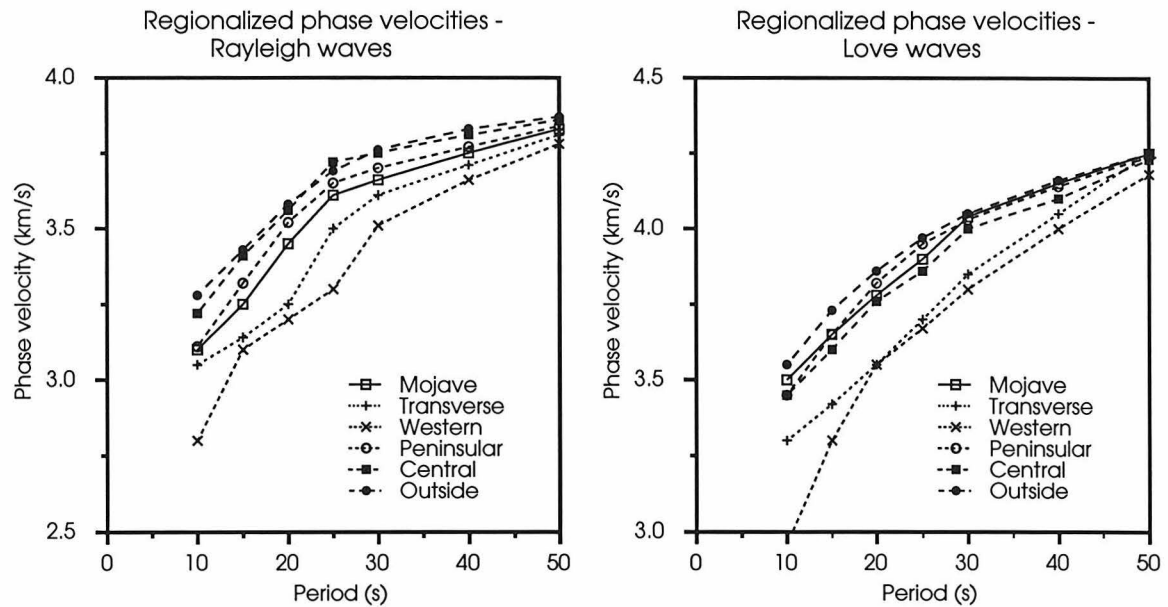


Figure 6. Dispersion curves for the different subregions. "Outside" refers to areas outside these regions. These velocities have been determined using some well-constrained master events. (a) Rayleigh waves, (b) Love waves.

correction is given in figure 7 (b,c) which shows the difference in waveform between a seismogram calculated using an average model and a seismogram which has been corrected for lateral phase velocity variations. For areas outside these subregions we assume a generic dispersion curve based on the model used by Dreger and Helmberger (1991). From a comparison of the dispersion curves of the various paths, we can see that there is a variation in phase velocity of up to 10 percent between the different paths. The most pronounced anomalies are in the western and northwestern areas involving paths to the Santa Barbara station (SBC) and paths from the Central Valley as well as the Sierra Nevada. The seismograms show complicated waveforms with long coda wavetrains after the surface wave, which suggests that multipathing has occurred along those paths.

From the modelling of regional broad-band body-waves, Dreger & Helmberger (1991) concluded that these can be reproduced accurately with one-dimensional models, i.e., without lateral variations. This implies that the lateral variations that we found are concentrated in the upper few kilometers of the crust for which the body-waves are not very sensitive. When we calculate dispersion curves for different crustal models (fig. 3), it is

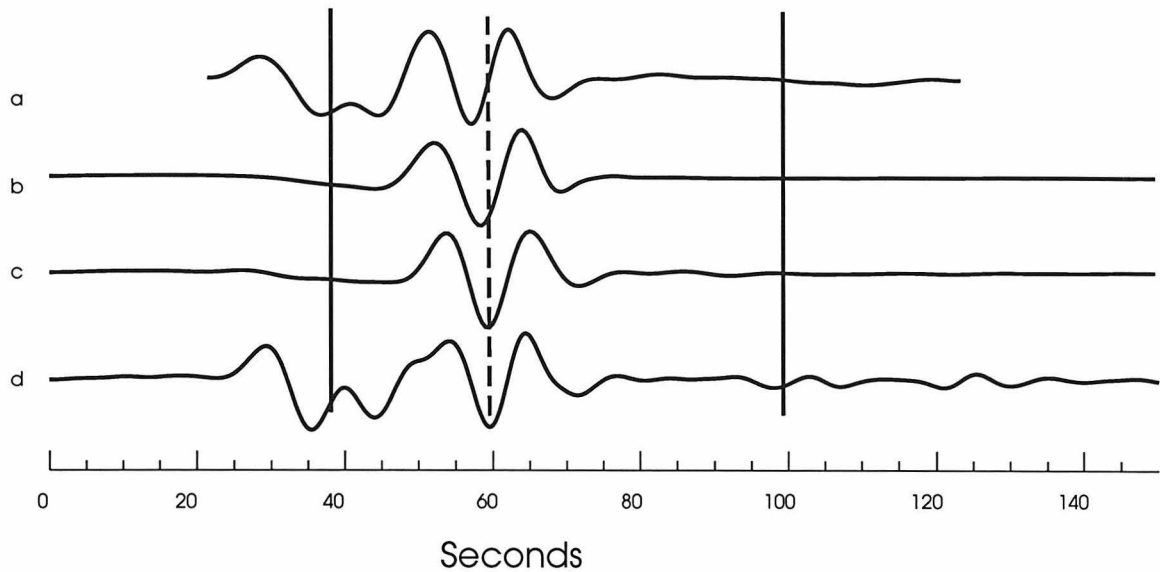


Figure 7. Comparison of data and synthetic seismograms. Seismogram (a) was calculated using an FK-code (Saikia, pers. comm.), (b) was calculated with fundamental mode summation, similar to the one used for the inversion, (c) is identical to (b) except that the phase velocities have been corrected using the regionalized phase velocity model, and (d) is the actual data, recorded at station PAS. All the synthetics were calculated using the mechanism determined with our inversion procedure and all seismograms have been band-pass filtered between 10 and 100 sec. The solid vertical lines indicate the group velocity window which is used in the inversion, the dashed line illustrates the phase line-up.

also clear that the upper five kilometers have a large effect on the phase velocities (fig. 4) in the period range from 10 to 30 seconds.

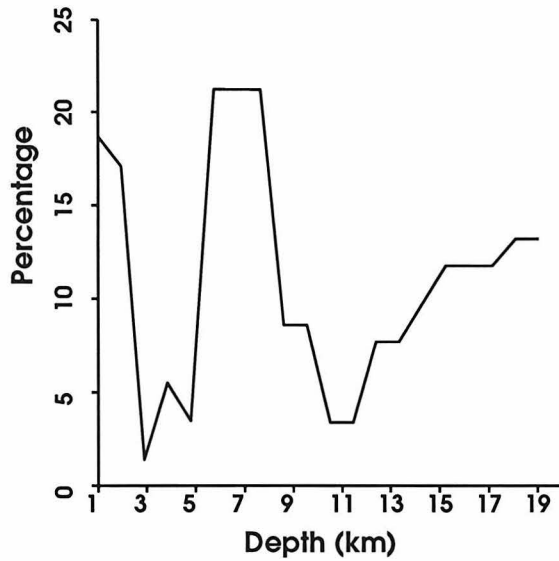
### Synthetic tests

We have also carried out synthetic tests in which we calculated full waveforms using a F-K code (Saikia, pers. comm.) and inverted these waveforms with our moment tensor inversion. The results indicate that the influence of higher mode, i.e. body-wave, contamination on our results is negligible. This is also apparent from visual comparison of the full waveform synthetics and those calculated with fundamental modes only (fig. 7), if they are low-pass filtered at ten seconds. We think that multipathing of the fundamental mode

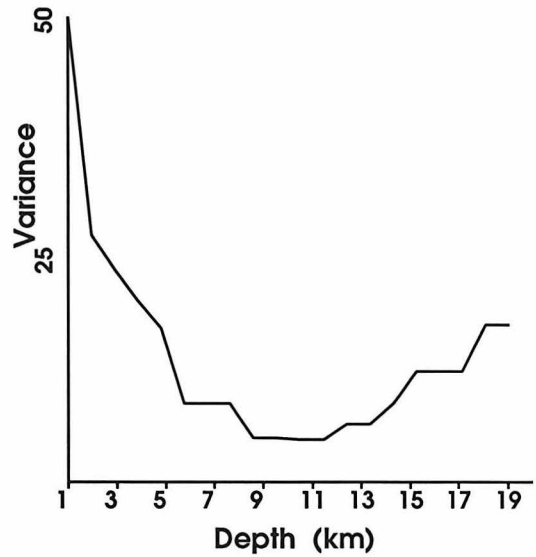


## Aftershock 9/15/92

**b - Epsilon**



**c - Sigma**



**d - Moment**

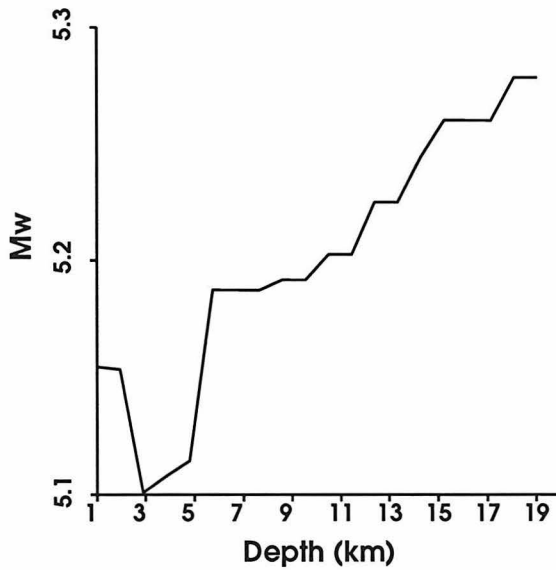


Figure 8b. Variation of the non-double couple component with depth.

Figure 8c. Depth dependence of the variance. We pick the depth with lowest variance for our final inversion results.

Figure 8d. Variation of the moment with depth.

---

surface waves due to lateral heterogeneity is a larger source of error than the existence of higher modes. Because the synthetic seismograms were calculated using a 1-dimensional model whereas our inversion compensates for lateral variations, we actually included some noise in these tests in the form of phase errors. Nevertheless, the resulting solutions were always very close to the mechanisms for which the synthetics had been calculated, with differences in strike and dip on the order of 5 degrees and differences in depth on the order of 1 to 2 kilometers. The best test results were obtained for events deeper than 5 kilometers.

### **Depth determination**

The inversion result depends on depth (fig. 8) and using an incorrect depth can give rise to a large non-double couple component in the moment tensor, but it can also result in a different mechanism. This can be seen from the shape of the excitation functions for different depth (fig. 2). The extrema and zero-crossings of the excitation functions for different periods occur at different depths. Therefore, if the inversion is carried out at the wrong depth, the resulting mechanism may be very different. Since the depths obtained from the local networks are usually not well constrained, especially immediately after the earthquake, it is necessary to determine the depth as well. Because of the rapidity of the inversion, we can solve this problem by inverting for a whole range of depths, typically between 1 and 20 kilometers with one kilometer intervals, and choosing the depth where the variance is minimal. This depth often coincides with a minimum in the non-double couple component. Our depth determinations are consistent with those obtained by other methods based on wave-form inversion or first-motion data, except for events shallower than 5 kilometers. The differences for shallow events are probably the result of several factors: the first-motion solutions are unreliable for shallow events; the uppermost crust has the strongest lateral variation, so that our eigenfunctions may not be appropriate; and for shallow events the eigenfunctions in the period range that we use are not very sensitive to depth. It is difficult to give an error margin for the depth determination because the

---

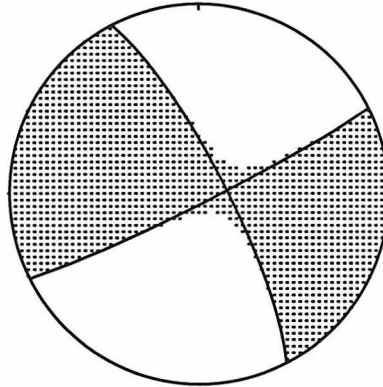
# Aftershock 9/15/92

1992 259 8 47 11.0

Latitude Longitude Depth  
34.060 -116.370 11. km

Moment= 8.01 e 23 dyn.cm, Mw 5.2

Strike Dip Slip  
63.4 85.7 11.3



Love

Rayleigh

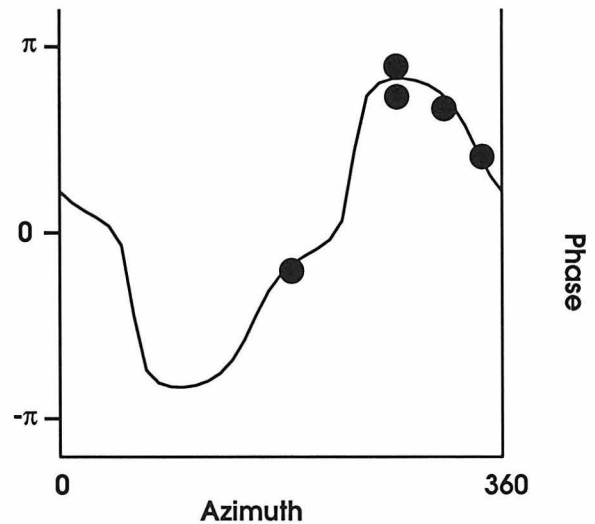
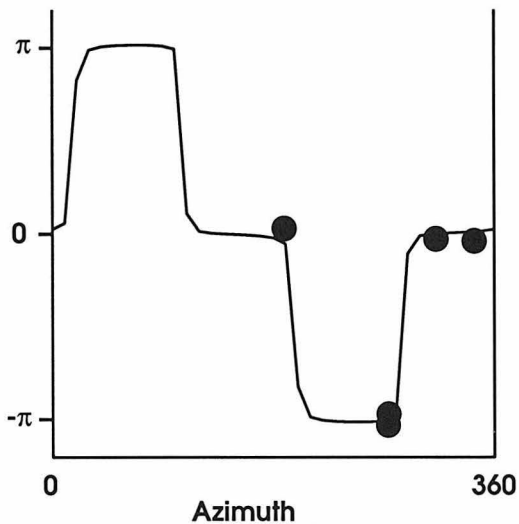
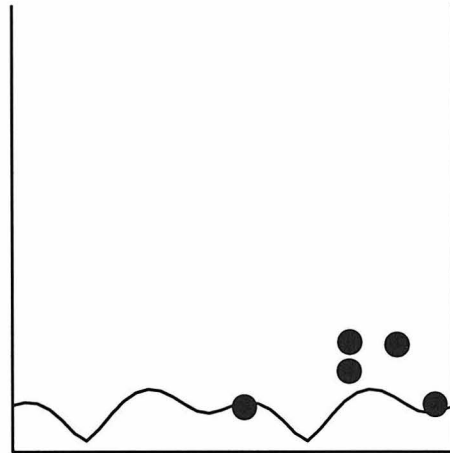
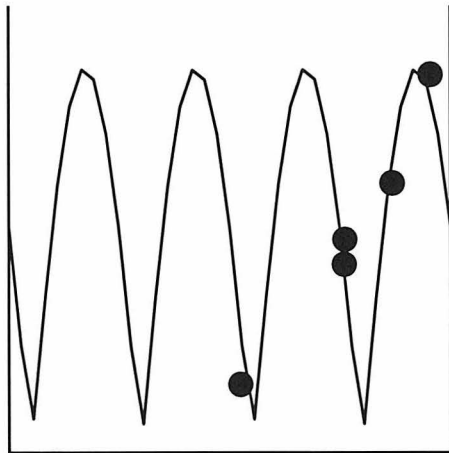


Figure 9. Moment tensor solution for an aftershock to the Landers earthquake (same as fig. 8). In the lower panel, the azimuthal variation of the source spectrum (around 20 sec.) corresponding to this solution is plotted together with the observed values (dots).

---

width of the minimum varies from event to event, but usually the minimum in variance is well constrained within 2 kilometers.

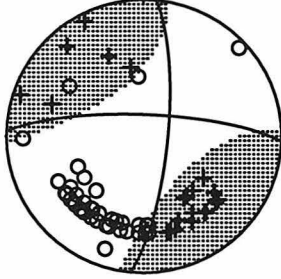
### **Performance and results**

We have used this inversion program since the spring of 1992 on a routine basis and have also studied some events recorded during the early deployment of TERRAscope. These events include the 1991 Sierra Madre earthquake, the 1992 Coso swarm, the 1992 Joshua Tree and Landers-Big Bear sequences, amounting to well over 160 events ranging in magnitude from 3.2 to 6.5 (Appendix A). An example of an inversion result for a Landers aftershock is given in figure 9. Figure 10 shows some representative moment tensor solutions with the best fitting double-couple and the first motion picks from the SCSN as comparison. Our results are very consistent with the first-motion mechanisms and are quite sensitive to subtle changes in the mechanism, e.g. Sierra Madre aftershocks, Coso swarm. We have noticed that the solution is quite robust for errors in location of up to 10 kilometers, which is the error level for the locations from the real-time system of the SCSN. The time to obtain a solution, on the order of a minute, is a fraction of the time needed for data acquisition, so the next logical step for speeding up this process will be installation of continuous data transmission from the stations to the central site at the Caltech Seismo Lab.

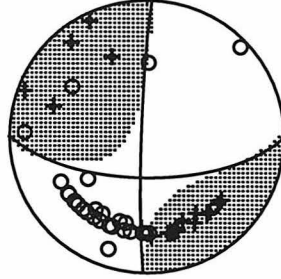
The correction for lateral inhomogeneity of the crust works very well in most cases, but the amplitudes at SBC are persistently higher than predicted by our moment tensor solutions. This is almost certainly due to strong multipathing and scattering in this area since the wavetrains tend to have long codas. For this reason we usually omit SBC from the inversion until we have solved this problem, either by including some empirical correction or by using more sophisticated raytracing methods which take into account lateral velocity

---

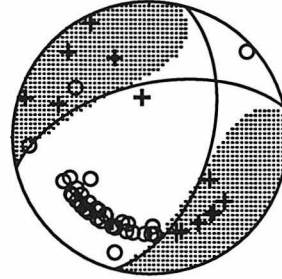
**a - Coso 02/19/92 1**  
Mw= 4.0



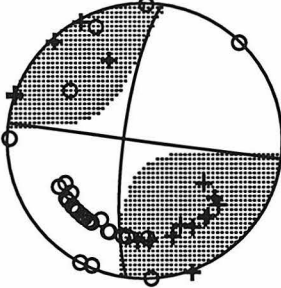
**b - Coso 02/19/92 2**  
Mw= 3.6



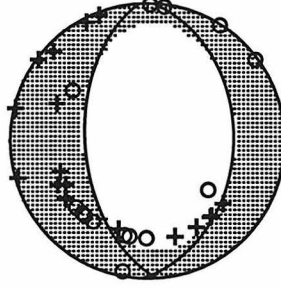
**c - Coso 02/21/92**  
Mw= 3.5



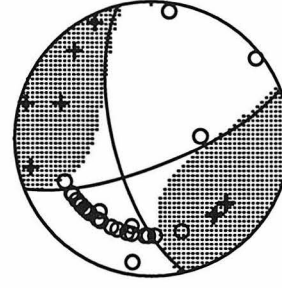
**d - Coso 02/22/92**  
Mw= 3.5



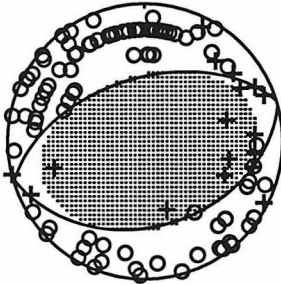
**e - Coso 03/16/92**  
Mw= 3.5



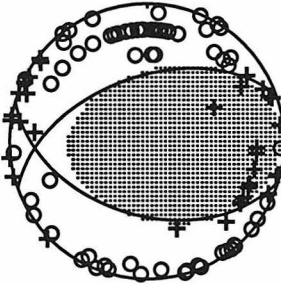
**f - Coso 03/17/92**  
Mw= 3.7



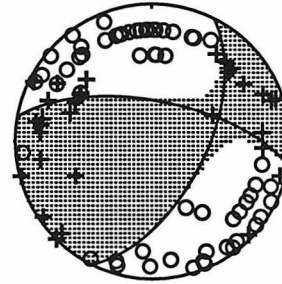
**g - S. Madre 06/28/91**  
Mw= 5.6



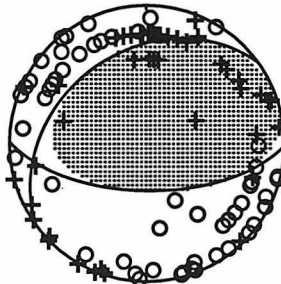
**h - S. Madre 06/28/91 2**  
Mw= 4.2



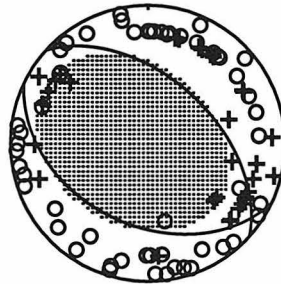
**i - S. Madre 06/28/91 3**  
Mw= 3.7



**j - S. Madre 07/06/91**  
Mw= 3.7



**k - San Fernando 07/05/91**  
Mw= 3.7



**l - Wrightwood 04/15/92**  
Mw= 3.3

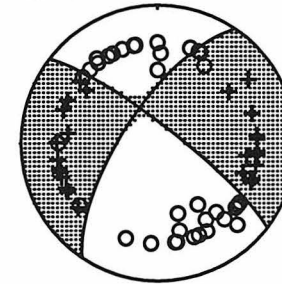


Figure 10. A comparison of our moment tensor solutions and first motion data from the Southern California Seismic Network. (a-f) Coso swarm (Feb. March 1992), (g-k) Sierra Madre sequence, (l) Wrightwood.

---

Sierra Madre earthquake - 91/06/28					
	Strike	Dip	Slip	Moment	Depth
DH	235.	50.	74.	2.5	12.
Wald	243.	49.	82.	2.8	11.
Harvard CMT	223.	58.	58.	3.6	15.
This study	253.	52.	89.	3.3	11.

---

Table 2. Comparison of results for the Sierra Madre earthquake. DH - Dreger and Helmberger, 1992, Wald - Wald, 1992, Harvard - Dziewonski et al., 1992. Depth in kilometers, moment in  $10^{24}$  dyne.cm.

---

Joshua Tree earthquake- 92/04/23					
	Strike	Dip	Slip	Moment	Depth
Dreger	263.	73.	2.	1.43	11.
Harvard CMT	81.	87.	-1.	3.6	15.
This study	83.	78.	6.	1.95	10.

---

Table 3. Comparison of results for the April 1992 Joshua Tree earthquake. Dreger - Dreger (pers. comm.), Harvard - Dziewonski et al., 1993. Moment in  $10^{25}$  dyne.cm.

---

Big Bear earthquake - 92/06/28					
	Strike	Dip	Slip	Moment	Depth
JHH	321.	86.	200.	5.3	3-8
Harvard CMT	48.	88.	2.	6.78	15.
This study	46.	81.	7.	4.52	12.

---

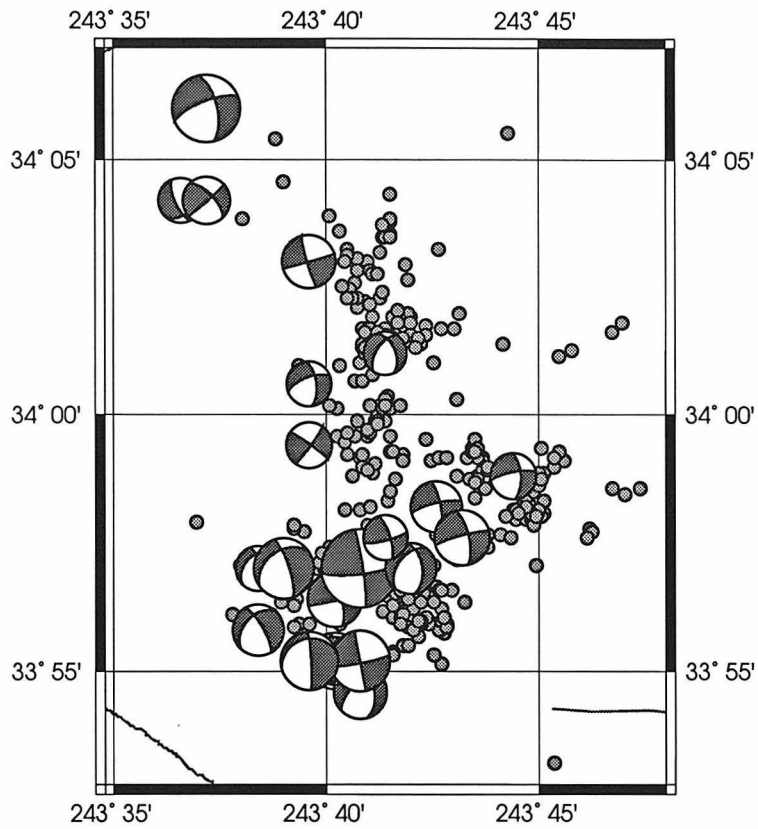
Table 4. Comparison of results for the June 1992 Big Bear earthquake. JH - Jones and Hough, 1995, Harvard - Dziewonski et al., 1993. Moment in  $10^{25}$  dyne.cm.

---

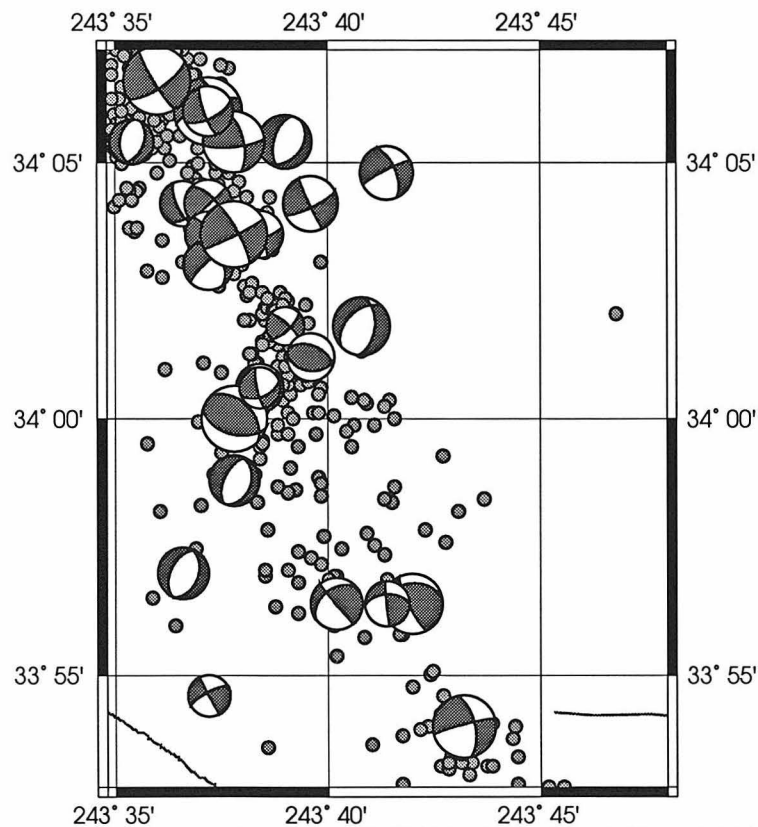
variations.

The number of stations needed to obtain a reliable solution depends on many factors like azimuthal coverage, mechanism, noise level and accuracy of the velocity model. In many cases we found that two stations can actually give good results, provided we can use both Love and Rayleigh waves. An example is the Coso swarm, for which we often had data from GSC and ISA only. The solutions, plotted in fig 10(a-f), vary from event to event.

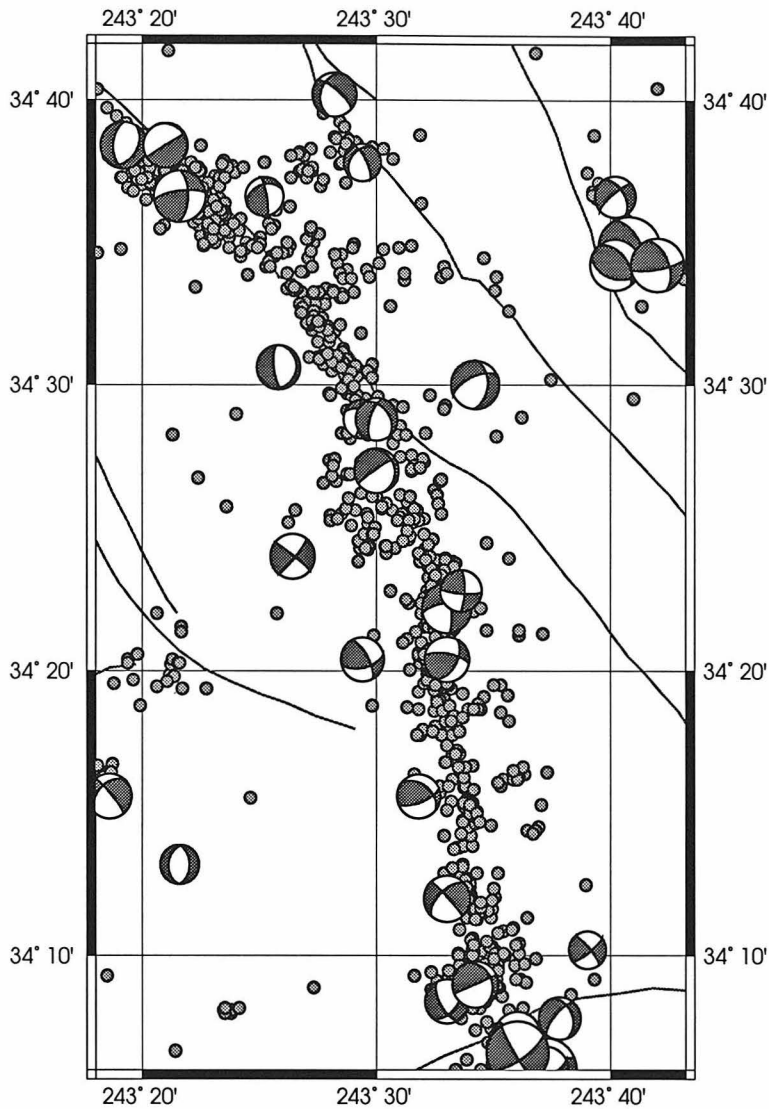
---



*Figure 11. Moment tensor solutions for the 1992 Joshua Tree earthquake and its aftershocks. The location of this box is depicted in fig. 1*



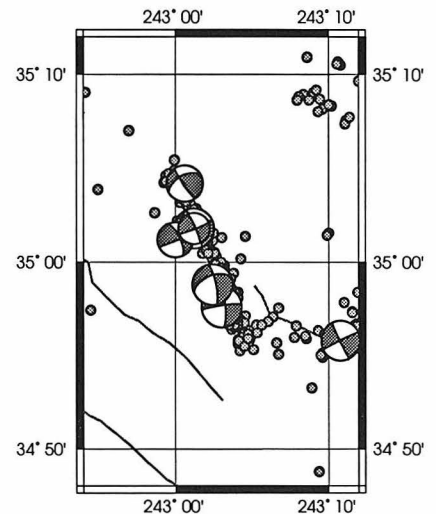
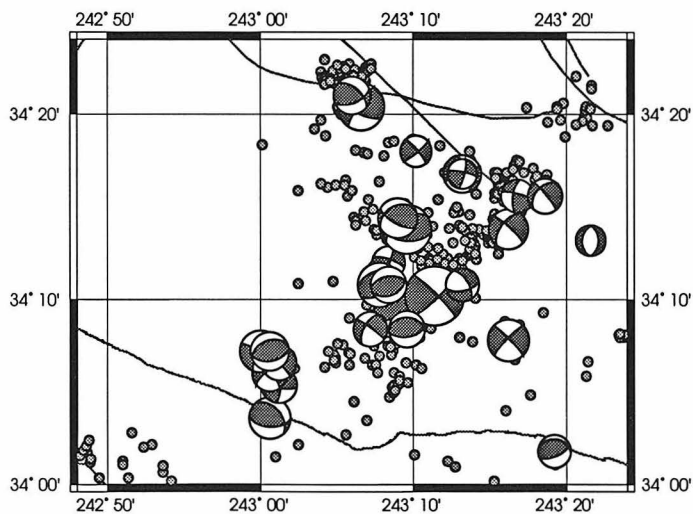
*Figure 12a. Mechanisms for aftershocks of the 1992 Landers earthquake. The area is the same as in figure 11.*



*Figure 12b (left). Mechanisms of aftershocks of the Landers earthquake along the surface rupture.*

*Figure 12c (bottom left). Aftershocks to the Landers earthquake in the Big Bear area.*

*Figure 12d (bottom). Aftershock mechanisms in the Barstow area.*



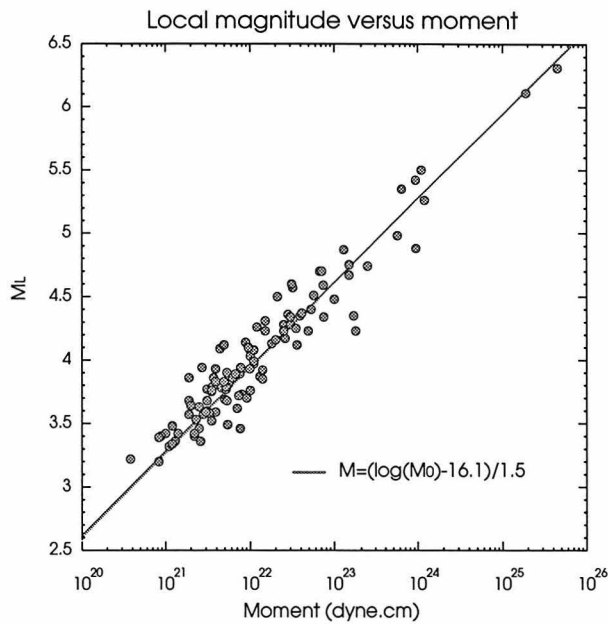


Figure 13. The relation between  $M_L$  and  $M_0$  in Southern California. The straight line represents the relation:  $M = (\log M_0 - 16.1) / 1.5$  (Thatcher and Hanks, 1973).

This variation is obvious in the solutions obtained from the first motion data. This demonstrates that even with only two stations we can resolve the difference in the mechanisms shown in fig. 10(a-f).

In table 2 we compare the results of our work with body-waveform inversions on the Sierra Madre earthquake by Dreger and Helmberger (1991) and Wald (1992), as well as the Harvard CMT solution. Our mechanism is very similar to theirs; our moment,  $3.3 \times 10^{24}$  dyne.cm, is somewhat larger but comparable to their solutions. Likewise, our results for the Joshua Tree and Big Bear earthquakes are very similar to those of other studies (tables 3 and 4). The difference in moment between the various authors can be attributed to the use of different crustal models, different depth and different frequency range of the data used for the inversion. The solutions for the Sierra Madre mainshock and some of the aftershocks are plotted in figure 10(g-k). A comparison of these solutions with the first motion data again demonstrates that we can resolve subtle changes in mechanism.

The smallest event we could analyze was the Wrightwood event (fig 10(l)) which had a local magnitude of 3.2. This event was favorably located in the middle of TERRAScope with both good azimuthal coverage and short distances. For more general locations within

---

the TERRAScope network the magnitude of the smallest event we can analyze is about 3.4, and with the increasing number of stations we expect that an  $M_W$  of 3.4 will be our lower limit for routine processing.

An upper limit to the size is primarily set by the dimensions of the rupture since we are using a point source approximation. We could not obtain a satisfactory solution for the Landers ( $M_W = 7.3$ ) earthquake because of strong directivity and large source dimensions. However, the Joshua Tree ( $M_W = 6.1$ ) and the Big Bear earthquakes ( $M_W = 6.4$ ) were still within the capability of our method.

The Joshua Tree and Landers sequences (Kanamori et al., 1992, Hauksson et al., 1993) provided a wealth of data for testing our method. The focal mechanisms we determined are plotted in figures 11 and 12 for selected regions. The aftershocks have a wide range of mechanisms. Many of them are very different from the mainshock mechanism. In fact, some of the larger aftershocks to the Landers and Big Bear earthquakes are purely dip-slip. Due to the data-retrieval system at the time, most of these solutions were obtained within half an hour after the events occurred, which means that we did run up a small backlog of events in the very early stages of the aftershock sequence but not thereafter.

Although a good azimuthal station coverage is desirable, we are not restricted to events that are within the TERRAScope area. We have included several outlying events like the San Simeon (Central California), San Miguel (Baja California), Little Skull Mountain (Nevada), Alum Rock (near San Jose) and Parkfield earthquakes. Because of the larger distances the influence of lateral inhomogeneity is more severe, especially at shorter periods. Hence we generally choose longer periods (up to 60 seconds) for these events. The resulting source mechanisms for these events are consistent with other studies (Dreger and Helmberger, 1993 (San Miguel), Walter, 1993 (Little Skull Mountain), Ritsema, pers. comm. (Parkfield), and Pasyanos, pers. comm. (Alum Rock)).

Another advantage of our method is that we now obtain reliable estimates of seismic

---

moments on a routine basis for events down to magnitude 3.4. Comparison of these values with estimates of seismic energy and with the local magnitudes provides a basis for scaling relations for earthquakes in Southern California. In fig. 13 we compare the seismic moments with the local magnitudes determined with SCSN short-period data. The dominant frequency in the  $M_L$  determinations is 1 Hz, whereas our seismic moments are estimated at periods longer than 10 seconds. The relationship between  $\log M_0$  and  $M_L$  is linear over the whole range from  $M_L = 3$  to 6.5. The best fit is  $M_L = (\log(M_0) - 16.1)/1.5$ , which is the relation found by Thatcher and Hanks (1973). The scatter is less for earthquakes in the 6-10 km depth range than for other depth ranges. This may be the result of higher-mode contamination and lateral heterogeneity.

Kanamori et al. (1993) found a linear relationship between  $\log E_S$  ( $E_S$ : released energy) and  $M_L$  with a slope of 1.96. This and the slope of 1.5 of the  $\log M_0$  versus  $M_L$  relationship suggests  $E_S/M_0 \sim M_0^{1/3}$  on the average.

## Conclusion

Short-period surface waves can be used for routine moment-tensor determinations of local earthquakes with magnitude greater than 3.2. In combination with the real-time location provided by the SCSN this method can be automated for real-time mechanism and moment determinations. Since this inversion does not require any manual processing, except perhaps for eliminating noisy records in the case of smaller events, it is very straightforward to automate this process and include it in the routine automatic analysis performed at the SCSN. The system can be refined further by allowing for finite rupture and by including a grid search technique to determine better locations in case the RTP location is not accurate enough. Our results confirm the results obtained by Thatcher and Hanks (1972) on the relationship between  $M_0$  and  $M_L$ .

## Acknowledgments

We would like to thank the people responsible for the daily operation of the Southern California Seismic Network for their help. This work was partially supported by USGS grant 1434-93-G-2287. Division of Geological and Planetary Sciences contribution no. 5467.

## References

- Aki, K., 1966. Generation and propagation of G waves from the Niigata earthquake of June 16, 1964. Part 2. Estimation of earthquake moment, released energy and stress-strain drop from the G wave spectrum. *Bull. Earthq. Res. Inst.*, 44, 73-88.
- Dreger, D. and Helmberger, D., H., 1991. Source parameters of the Sierra Madre earthquake from regional and local body waves. *Geoph. Res. Lett.* 18, no. 11, 2015-2018.
- Dreger, D. and Helmberger, D.H., 1993. Determination of source parameters at regional distances with three-component sparse network data. *J. Geoph. Res.*, 98, B5, 8107-8125.
- Dziewonski, A.M. and Woodhouse, J.H., 1983. Studies of the seismic source using normal-mode theory. In *Earthquakes: observation, theory and interpretation*, Kanamori, H. and Boschi, E., eds., North-Holland, Amsterdam, 45-137.
- Dziewonski, A.M., Ekström, G. and Salganik, M.P. 1992. Centroid moment tensor solutions for april-june 1991. *Phys. Earth Plan. Int.*, 77, 151-163.
- Dziewonski, A.M., Ekström, G. and Salganik, M.P. 1993. Centroid moment tensor solutions for april-june 1992. *Phys. Earth Plan. Int.*, 71, 6-14.
-

- 
- Hauksson, E., Jones, L.M., Hutton, K. and Eberhart-Phillips, D., 1993. The 1992 Landers earthquake sequence: Seismological observations. *J. Geoph. Res.*, 98 (B11), 19,835 - 19,858.
- Jones, L. E., Hough, S.E., 1995. Analysis of broadband records from the June 28, 1992 Big Bear earthquake: evidence of a multiple-event source. *Bull. Seis. Soc. Am.*, in press.
- Kanamori, H. and Given, J.W., 1981. Use of long-period surface waves for rapid determination of earthquake-source parameters. *Phys. Earth Plan. Int.* 27, 8-31.
- Kanamori, H., Thio, H.K., Dreger, D., Hauksson, E. and Heaton, T.H. (1992). Initial investigation of the Landers, California, earthquake of 28 June 1992 Using TERRAScope. *Geoph. Res. Lett.* 19, no. 22, 2267-2270.
- Kanamori, H., Mori, J., Hauksson, E., Heaton, T.H., Hutton, L.K. and Jones, L.M., 1993. Determination of Earthquake Energy Release and  $M_L$  using TERRAScope. *Bull. Seis. Soc. Am.*, 83,no. 2, 330-346.
- Kawakatsu, H., 1989. Centroid single force inversion of seismic waves generated by landslides. *J. Geoph. Res.*, 94, 12,363-12,374.
- Mendiguren, J.A., 1977. Inversion of surface wave data in source mechanism studies. *J. Geoph. Res.*, 82, 889-894.
- Patton, H.J., 1980. Reference point method for determining the source and path effects of surface waves. *J. Geoph. Res.*, 85, 821-848.
- Patton, H.J., Zandt, G., 1991. Seismic moment tensors of Western U.S. earthquakes and implications for the tectonic stress field. *J. Geoph. Res.*, 96, B11, 18,245-18,259.
- Ritsema, J., Lay, T. 1993. Rapid source mechanism determination of large ( $M_w > 5$ ) earthquakes in the Western United States. *Geoph. Res. Lett.*, 20, no. 15, 1611-1614.
- Romanowicz, B. and Monfret, T. 1986. Source process times and depths of large earthquakes by moment tensor inversion of mantle wave data and the effect of lateral
-

heterogeneity. *Ann. Geoph.*, 4. 271-183.

Romanowicz, B., Dreger, D., Pasyanos, M., Uhrhammer, R., 1993. Monitoring of strain release in Central and Northern California using broadband data. *Geoph. Res. Lett.*, 20, no. 15, 1643-1646.

Thatcher, W. and Hanks, T.C., 1973. Source parameters of Southern California earthquakes. *J. Geoph. Res.*, 78, 8547-8576.

Wald, D.J., 1992. Strong-motion and broadband teleseismic analysis of the 1991 Sierra Madre, California, earthquake. *J. Geoph. Res.*, 97, no. B7, 11,033-11,046.

Walter, W.R., 1993. Source parameters of the June 29 Little Skull Mountain earthquake from complete regional waveforms at a single station. *Geoph. Res. Lett.*, 20, no. 5, 403-406.

---

## Chapter 2:

# Lateral variation of surface wave velocities in Southern California

### Abstract

We applied tomographic techniques to phase residuals of short period surface waves recorded by TERRAscope. Our results indicate that the phase velocities of Love and Rayleigh waves show strong lateral variations, up to 10%, even over a relatively small area like Southern California.

### Introduction

We present preliminary results of a tomographic study of Southern California using short-period fundamental mode Love and Rayleigh waves. At longer periods, these waves have been successfully used to study global structure (e.g. Zhang & Tanimoto, 1993) as well as more regional structure. Thanks to the increasing density of local broad-band networks like TERRAscope, we are now able to apply this method on an even smaller scale, and we will show that lateral variations can be studied using short period surface waves.

A reference model for lateral variations of phase velocities can be very useful for seismic source studies using surface waves (Thio & Kanamori, 1995), because it provides better corrections to the phase spectra, but it also gives us better constraints on lateral variations in S wave velocities, which have not been studied as extensive as the P wave velocities.

---

## Method

We computed source spectra for all station-receiver pairs (fig. 1) using the results from our moment tensor inversions (Thio & Kanamori, 1995) and subtracted these from the observed phases, which have been corrected for a simple one-dimensional velocity model. These phase differences ( $\Delta\varphi$ ) were then translated into travel-time residuals ( $\Delta t$ ) using:

$$\Delta t = \frac{\Delta\varphi}{2\pi} T$$

where  $T$  is the period. In a strictly 2-dimensional approximation these residuals can be represented as a summation of travel time residuals along elements of the ray-path. If we divide the map of our region in blocks with different phase velocities, then:

$$\Delta t_j = \sum_{i=1}^N \Delta p_i s_{ij}$$

with  $\Delta p_i$  slowness (inverse phase velocity) perturbations in block  $i$  and  $s_{ij}$  the length of the segment of path  $j$  in block  $i$ .  $N$  is the total number of blocks. This linear set of equations can then be solved as a standard least-squares problem:

$$\mathbf{A}\bar{x} = \bar{b}$$

where  $\mathbf{A}$  is a matrix with the segment-lengths  $s_{ij}$  as elements,  $x$  a vector containing the slowness perturbations and  $b$  the travel-time residuals. To prevent unrealistic amplitude fluctuations, we added damping and smoothing elements to the matrix  $\mathbf{A}$ .

The errors in the travel-time residuals can have a large effect on the errors in the slowness

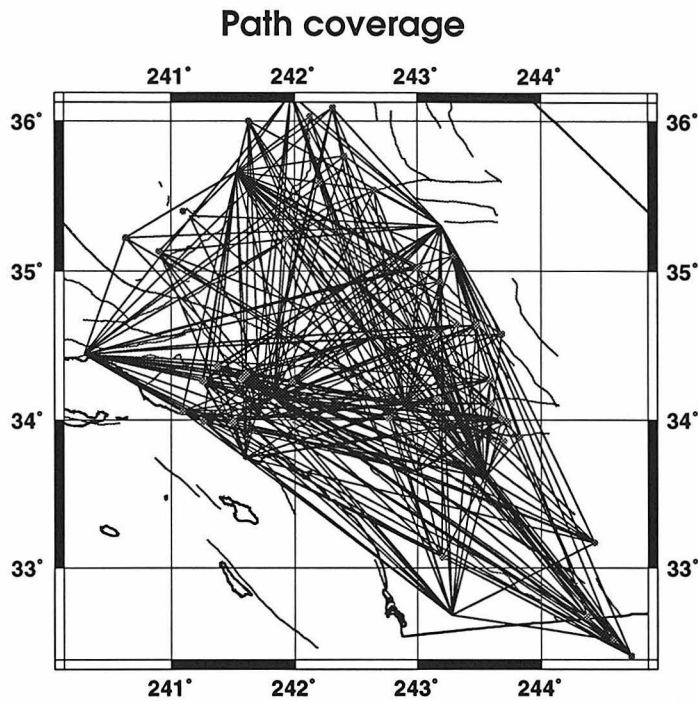


*Figure 1. Map of Southern California showing the set of raypaths used in this study.*

perturbations, because they are inversely proportional to the pathlength. We therefore experimented with distance-based weighting and also distance cutoffs. We found that using a weighting function of the form:

$$W(\Delta) = 1 - e^{-\frac{\Delta}{\lambda}}$$

where  $\lambda$  is the wavelength at that period and  $\Delta$  the distance, gave good results.

## Data

We used data recorded by TERRAScope from local earthquakes in the magnitude range of 4 to 6. In this range there is sufficient excitation of surface waves in our period range so that we have good signal to noise ratios but the events are small enough that we don't have to account for finite source duration and dimension. We selected events so that we had a maximum but also balanced path coverage (fig. 1). To ensure sufficient path coverage, we did not include all TERRAScope stations, but limited ourselves to those which led to a

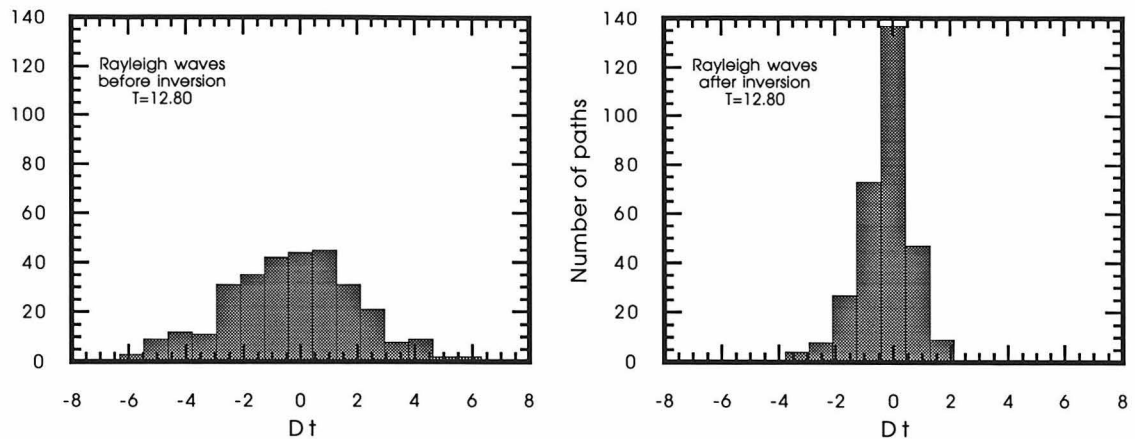


Figure 2. Histograms of the travel-time residuals for Rayleigh waves at a period of 12.80 sec. a (left) - before inversion, b (right) - after inversion.

homogenous path coverage, with many intersecting paths. In total we had more than 350 source-receiver pairs, but this number was reduced by applying some selection criteria; we eliminated paths which were within half a wavelength for that particular period, since the surface waves are not well developed in that range and since we use a cosine approximation to the Legendre polynomials which are required in the normal mode representation.

We experimented with various blocksizes, but in order to gain a maximum resolution we used a blockmodel with a blocksize of  $.25^\circ$  by  $.25^\circ$ . The travel-time residuals, plotted in fig. 2 and 3 follow in most cases a Gaussian distribution. As a starting model, we chose a standard model for Southern California. This model gives a reasonable fit to both the Love and Rayleigh wave dispersion measurements, although the Rayleigh wave seems a little biased with respect to this model. Using a different model, with lower velocities at the top gave a better fit to the Rayleigh waves but a worse fit to the Love waves. This may be a result of seismic anisotropy (Polet & Kanamori, 1995), where the SH velocities are systematically higher than the SV velocities. It could also be produced by lateral heterogeneity (Keilis-Borok, 1989) or a multilayered velocity model with rapidly changing velocities. However, the latter may be physically unrealistic. If the baseline of the residuals is shifted toward one side, then it is possible that some of the more outlying measurements will be folded around to the other end of the spectrum, i.e. residuals that are strongly positive may

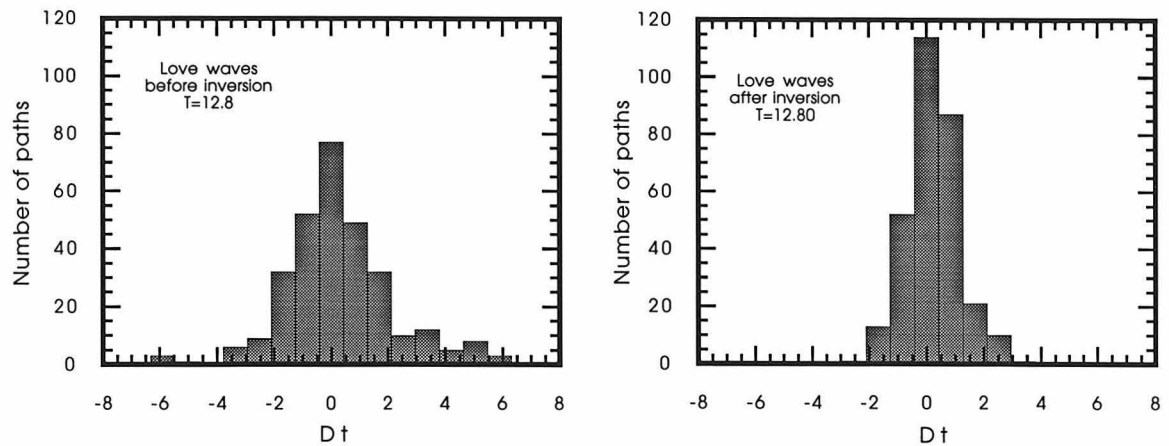


Figure 3. Histograms of travel-time residuals of Love waves at a period of 12.80 sec. a (right) - before inversion, b (left) - after inversion.

become negative, but after visual inspection of all histograms we believe that this is not a serious problem. Surface waves are sensitive to topography. We calculated partial derivatives for the phase velocity in relation to the topography but found that the topography of Southern California does not have a significant effect on the phase velocities, except, possibly, on the shortest periods for the Love waves.

## Results and conclusion

We present the complete set of maps of lateral phase velocity variations in appendix B and some examples in figure 4. It is clear that at shorter periods very significant variations of up to 10% exist. One of the clearest features is that there is a systematic difference between the northwestern and southeastern parts of the region. Especially in the Love waves, it is clear that the phase velocities tend to be higher in the south and east. This pattern persists to longer periods, and it may be an indication of a decrease in crustal thickness toward the south. Also, part of the Transverse ranges show a distinct low velocity anomaly at intermediate periods, especially in the Rayleigh waves. The occurrence of strong lateral variations in the western part of the region is consistent with the complex waveforms that are

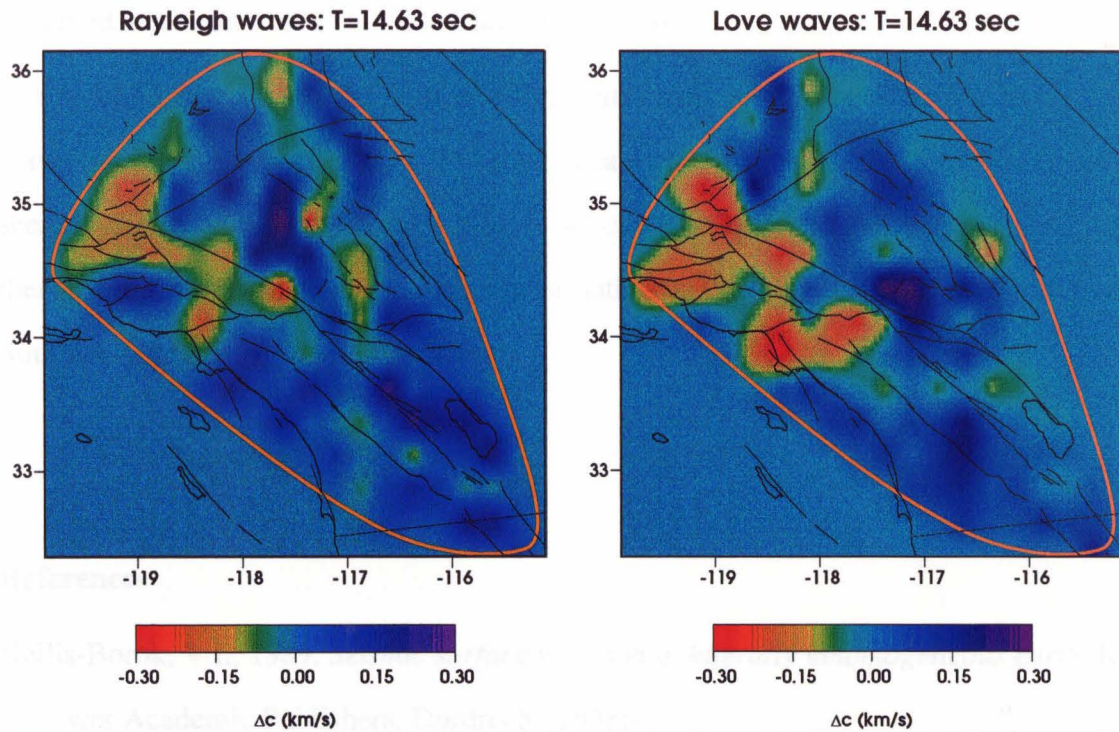
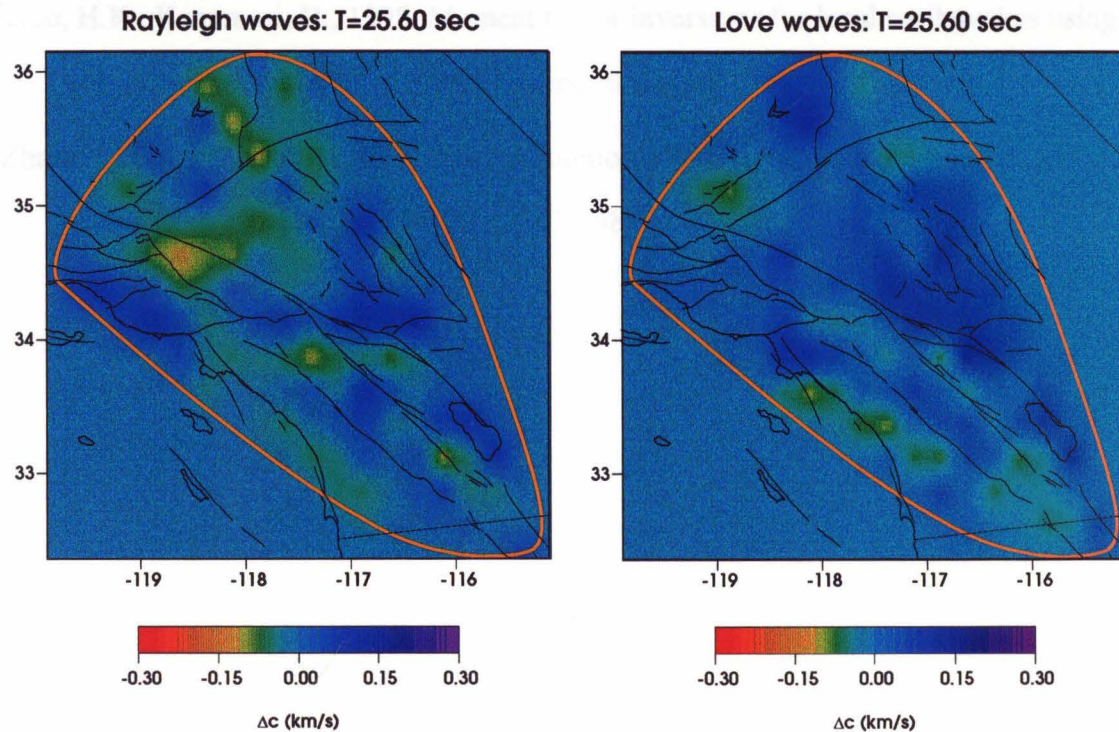


Figure 4. Examples of lateral phase velocity variations for Rayleigh and Love waves in Southern California. *a* (top) - at a period of 14.63 sec, *b* (bottom) at 25.60 sec. Contour scales are the same for all panels. Notice the decrease in amplitude of the variations at longer periods.



observed at station SBC (Thio and Kanamori, 1995).

The spatial dimensions of the anomalies are quite small, especially relative to the wavelength of the surface waves. However, because the pattern of these variations does not seem to change with larger block sizes, we believe that these anomalies are real, and that these surface waves can yield valuable information on the seismic structure of the crust of Southern California.

### **References**

- Keilis-Borok, V.I., 1989. *Seismic surface waves in a laterally inhomogeneous earth*. Kluwer Academic Publishers, Dordrecht, 293pp.
- Polet, J., Kanamori, H., 1995. Upper mantle structure beneath southern California determined from long-period surface waves. in prep.
- Thio, H.K., Kanamori, H., 1995. Moment tensor inversions for local earthquakes using surface waves recorded at TERRAScope. Bull. Seis. Soc. Am., in press.
- Zhang, Y.S., Tanimoto, T., 1993. High resolution global upper mantle structure and plate tectonics. J. Geoph. Res., 98, B6, 9793 - 9823.
-

## Chapter 3:

# Source complexity of the January 1994 Northridge earthquake and its relation with aftershock mechanisms

### Abstract

We determined the source process of the 1994 Northridge earthquake in relation to the aftershock mechanisms. To study the source complexity of the mainshock, we inverted the P and SH waveforms recorded by the IRIS and IDA/IRIS networks, using the method of Kikuchi and Kanamori (1991) in which the rupture is represented by a series of discrete subevents with varying mechanisms. The waveforms show that the rupture consisted of several subevents with about 2 sec in between. Our solution consists of three subevents with essentially the same mechanism, viz. strike/dip/rake:  $130^{\circ}/42^{\circ}/116^{\circ}$ . The first subevent occurred at a depth of about 19 km, followed after 2 sec by the second and largest subevent at a depth of 17 km and the third subevent, again 2 sec after the second, at a depth of about 13 km. The total moment from the body-waves of this sequence is about  $1.1 \times 10^{26}$  dyne.cm ( $M_W=6.6$ ) with a source duration of 7 sec.

The large depths of these subevents explain the lack of any surface rupture. Furthermore, the upward propagation of the subevents is consistent with the depth of the hypocenter and the distribution of the aftershocks, which are shallower and more northerly than the mainshock hypocenter.

The aftershocks were analyzed using data from the TERRAScope network. We inverted short-period surface waves to determine the moment tensor for 70 events with  $M_W > 3.5$ . The aftershocks can be grouped into three regions based on the mechanisms; the eastern part of the aftershock zone, where we find thrust events with mechanisms very similar to the main event, a central area with predominantly strike-slip events and an area to the west

---

where we find oblique thrust events but with more northerly P-axes than in the eastern region. This distribution suggests that the fault system on which the Northridge earthquake occurred is segmented, and that the extent of the Northridge rupture is controlled by a change in geometry of the fault. We find a high stress-drop (270 bar) for the mainshock; we propose that the changes in the fault geometry prevented a slip-pulse from propagating, thereby causing a high ratio of slip to rupture length .

## Introduction

The Northridge earthquake ( $M_W=6.7$ ) is the largest earthquake to have occurred in the Los Angeles metropolitan area in this century. The epicenter (lat/lon: 34.21/-118.55) was located in the San Fernando Valley, southwest of the 1971 San Fernando earthquake (fig. 1). Due to its location, the earthquake caused a considerable amount of casualties and damage in the Santa Clarita Valley, the San Fernando Valley and the northern Los Angeles Basin (Scientists of the USGS and SCEC, 1994). The aftershocks span an area of about  $20 \times 30$  km<sup>2</sup> (Hauksson et al., 1995), with the largest concentration in the northeast of the mainshock hypocenter. In cross-section, the mainshock location and the aftershock distribution suggest that the rupture propagated upward on a south-dipping fault-plane. The mechanism, a thrust, is similar to that of the San Fernando earthquake, but the south dipping rupture plane stands in contrast to the north-dipping fault plane of the San Fernando earthquake (Whitcomb et al., 1973).

The fault on which the Northridge earthquake occurred is part of a larger system of faults in the Transverse Ranges. This fault system is under NNW compression (Norris & Webb, 1990). The compressive stress environment is associated with the big bend of the San Andreas fault, the main boundary between the North American and Pacific plates (fig 1). Since 1971 there have been numerous earthquakes along the Transverse ranges, notably

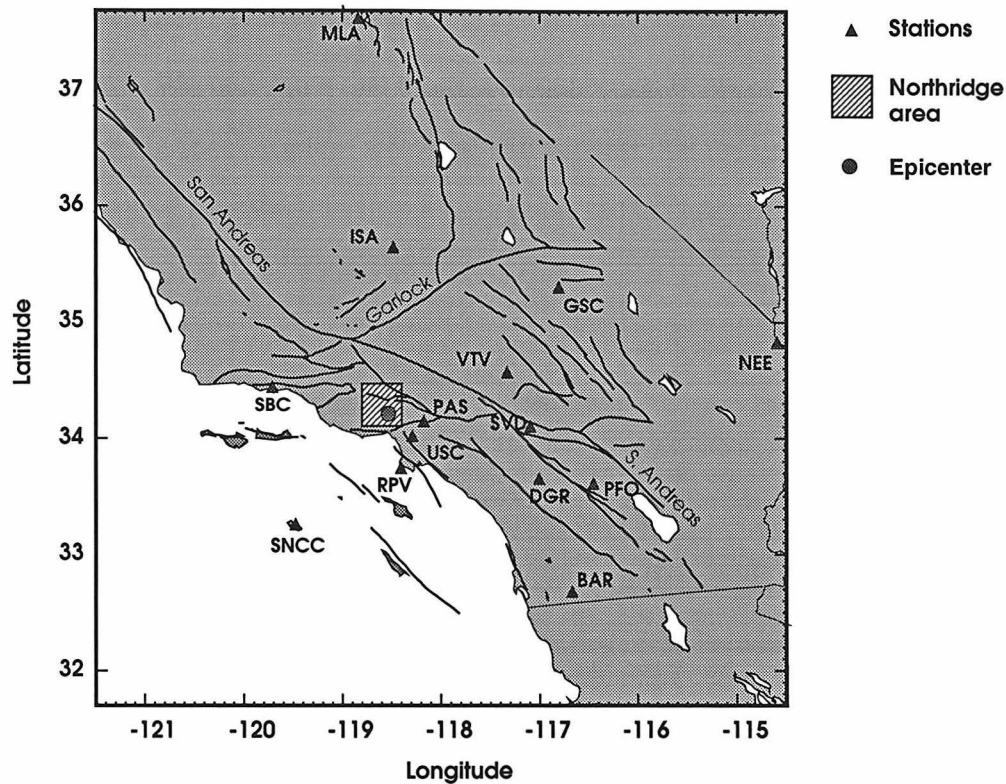


Figure 1. Map of Southern California including the TERRAscope stations used in this study. The hatched area is enlarged in figure 9.

the 1971 San Fernando earthquake ( $M_W=6.6$ ), but more recently the 1990 Upland earthquake ( $M_W=5.5$ , Dreger & Helmberger, 1991a), the 1991 Sierra Madre ( $M_W=5.8$ , Dreger & Helmberger, 1991b) and the 1989 Pasadena ( $M_L=4.9$ , Kanamori et al., 1990) earthquakes. The San Fernando earthquake occurred just northeast of the Northridge earthquake, with some overlap of the two aftershock zones (Mori et al., 1994). Rupture during the San Fernando earthquake reached the surface and produced surface breaks at several locations. The aftershock distribution shows a distinct pattern with the western edge of the aftershock zone having a sharp linear distribution of aftershocks in NE-SW direction. In this area the mechanisms are predominantly strike-slip with the strike aligned to the orientation of the edge. This led Whitcomb et al. (1973) to the conclusion that the fault-plane is offset along the western lineament and that this may have limited the western extent of the San Fernando rupture.

In this paper we determined the spatial extent and the complexity of the mainshock rupture

using teleseismic body-waves and the mechanisms of the larger aftershocks using TERRA-scope data. We will show that there is a connection between the aftershock mechanisms and the main shock rupture area, and will suggest that the extent of the rupture is influenced by complexities of the fault plane, which are reflected in the aftershock mechanisms.

### Data and method

In the first part of this study we used body-wave (P and SH) data, from the IRIS and IDA/IRIS networks (fig. 2), with epicentral distances between 30 and 90 degrees. All the data were deconvolved to displacement through a very wide passband (.0033 to 4 Hz). The waveform is relatively simple. The simplicity of teleseismic waveforms is often character-

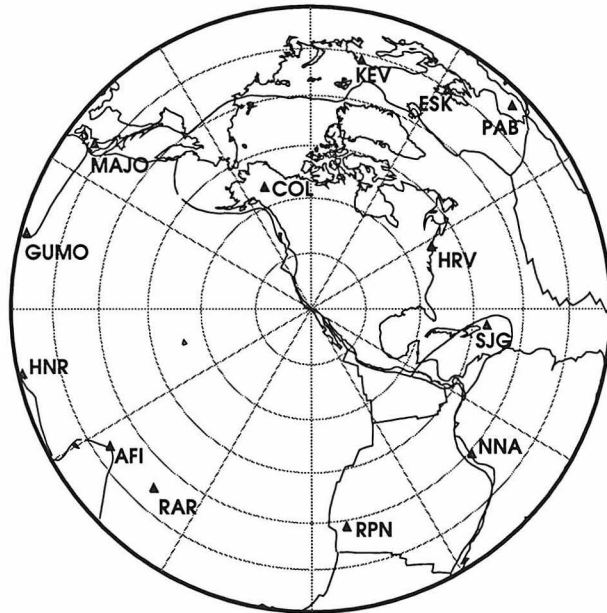


*Figure 2. Distribution of stations used in the teleseismic inversion. The projection is centered on Northridge. The distance to the outer rim is 90°.*

istic of dip-slip earthquakes, for which P waves to teleseismic stations leave the source in the direction close to the radiation maximum, resulting in clean waveforms (fig. 3).

However, figure 3 shows some evidence for source complexity. We can distinguish at least three episodes of energy release in the P-waves approximately 2 seconds apart, the second

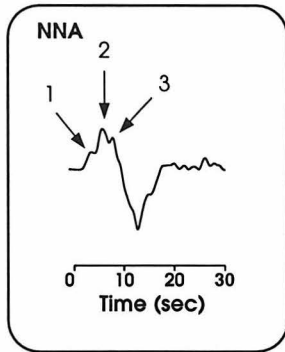


Figure 3. A P-wave form recorded at station NNA in Chile. Arrivals from distinct episodes of energy release are indicated with the arrows. The numbers correspond to the subevents used in this study.

h	$\alpha$	$\beta$	$\rho$
.5	2.4	1.4	2.0
1.0	3.8	2.2	2.1
4.0	5.2	3.0	2.4
9.5	6.2	3.6	2.7
19.0	6.6	3.8	2.8

Table 1. Velocity model used to compute teleseismic body waves.  $h$  is the layer thickness (km),  $\alpha$ ,  $\beta$  are P and S wave velocities respectively (km/s) and  $\rho$  is the density (g/cm<sup>3</sup>).

episode being the largest. In order to determine the spatial and temporal distribution of the energy release we used the method of Kikuchi and Kanamori (1991) where the P and SH waveforms are inverted to determine the subevent distribution, allowing the mechanisms of the individual subevents to vary. This is accomplished by computing synthetic wave forms from the fundamental Green's functions at all stations and choosing the mechanism (including location and timing) with the largest correlation coefficient.

In the second part of our study, we determined the source mechanisms of the aftershocks using the data from the TERRAScope network. We determined the complex spectrum, usually over a period range of 10 to 40 seconds, of the vertical and tangential components (Thio and Kanamori, 1995a), and applied propagation corrections to the spectrum to obtain the source-spectrum. This source spectrum is inverted for the moment-tensor elements. We determine the depth of these events by performing inversions for different depths and choosing the depth which gives the best fit.

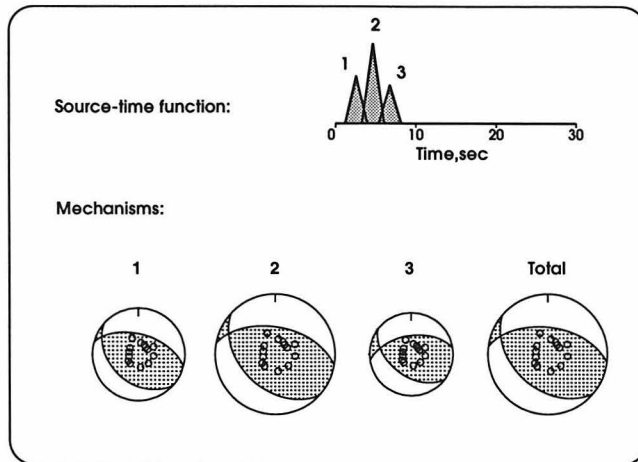


Figure 4. Source time function (top) of the Northridge earthquake from the first inversion. The bottom panel shows the individual source mechanisms of the subevents.

### Main shock inversion

We computed Green's functions using a layered model of Southern California obtained by Magistrale et al. (1991). It consists of a slow sedimentary layer on top of the crustal model which is widely used in seismic studies in Southern California (table 1).

To determine the overall mechanism we first inverted the seismograms using a long (8 sec.) time function and only one subevent. This yielded an event with a strike of about  $130^\circ$ , dip of  $40^\circ$ , rake of  $115^\circ$  and a depth of 17 km. On the basis of these results, as well as information provided by the Southern California Seismic Network (SCSN), we set up a grid network on a plane with a dip of  $45^\circ$  and a strike of  $130^\circ$ . The gridpoints are distributed at depths between 10 and 20 km.

We subsequently carried out the inversion with a series of subevents (up to 4) with individual time functions ranging in width from 2 to 4 sec. Using two subevents could not explain all the details in the P-waveforms, whereas four subevents resulted in an unstable solution. The best result was obtained with three subevents (figs. 4 and 5, table 2). The mechanisms of the subevent were not fixed or constrained, but determined by the inversion. Thus, the similarity of the subevents means that the mechanism did not change during rupture. In fact, the differences between the first and second subevent are

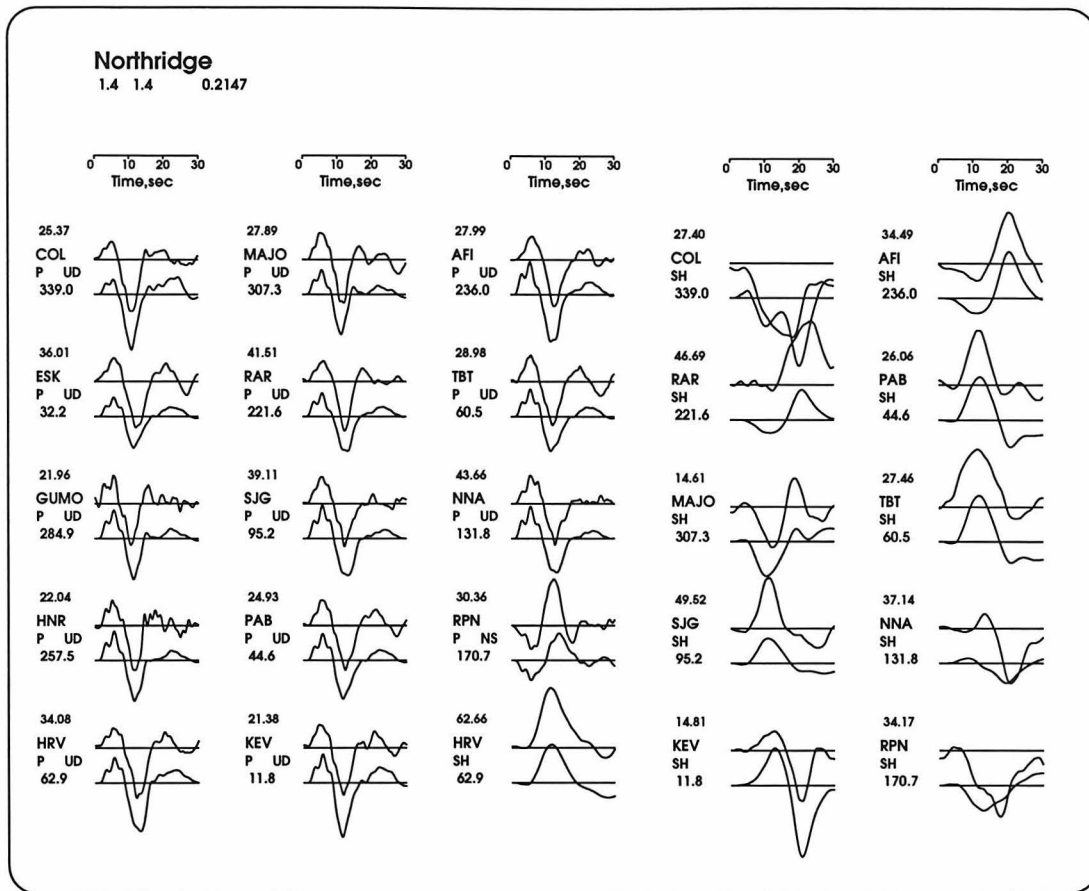


Figure 5. Data (top) and synthetic seismograms from the first inversion (bottom).

insignificant. The depths of the subevents can be well resolved with depth phases (pP and sP). They indicate that the rupture was primarily updip, starting at a depth of about 19 km with the largest energy release at 17 km and the last subevent around 14 km. Our inversion suggests that the width (in the horizontal direction) of the rupture zone is narrow, on the order of 3 km, but the minimum resolution of the horizontal location of the subevents in our inversion is on the order of 10 km. Hence, this means that the horizontal extent of the rupture did not exceed 10 km, which is consistent with the aftershock distribution of the first 11 hours.

The above results were obtained using simple triangular time-functions. To explore the degree of complexity of the rupture, we carried out a second inversion where we fixed the mechanism and location of each of the three subevents, but allowed the time function to

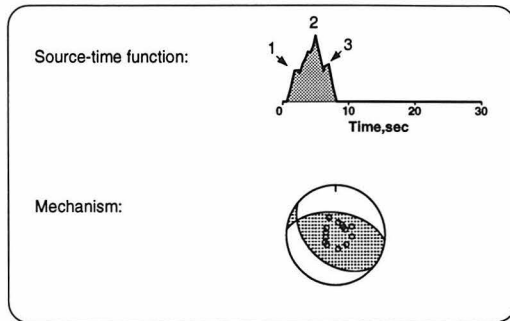


Figure 6. Source time function (top) of the Northridge earthquake from the first inversion. The bottom panel shows the single source mechanism used in the final inversion..

have a more complex shape than a single triangle. This was done by representing each subevent with several narrow triangular time functions (Kikuchi & Kanamori, 1991). To evaluate the significance of the mechanism change, we inverted the data for two cases, one with a different mechanism for each subevent, and the other with the same mechanism for all subevents. The results of the inversion with variable mechanisms and with a single mechanism were only marginally different and we conclude that no significant change of mechanism occurred during the rupture. Therefore, we used a single mechanism in the subsequent analysis.

The resulting time function is plotted in figure 6. This is of course smoother than that shown in figure 4, but the three pulses remain distinct. The seismic moment obtained by the second inversion is  $1.1 \times 10^{26}$  dyne.cm, which is slightly smaller than the moment derived from long-period (300-150 sec.) surface waves, viz  $1.5 \times 10^{26}$  dyne.cm, or regional short-period surface waves,  $1.6 \times 10^{26}$  dyne.cm (see below), but similar to results by Dreger (1994,  $M_0=1.2 \times 10^{26}$  dyne.cm) and Wald & Heaton (1994,  $M_0=1.2 \times 10^{26}$  dyne.cm), which are based on local and regional body-waves. The radiated energy can be computed from our results using the method of Kikuchi and Fukao (1988) and we obtain a value of  $.53 \times 10^{22}$  erg.

Looking at our rupture model in cross section (fig. 8) we see that the aftershock density along the fault-plane becomes much higher above our rupture zone. This is a frequently observed phenomenon in aftershock sequences and suggests that tectonic stresses are relieved on the actual rupture plane, but increase outside the ruptured areas (Mendoza &

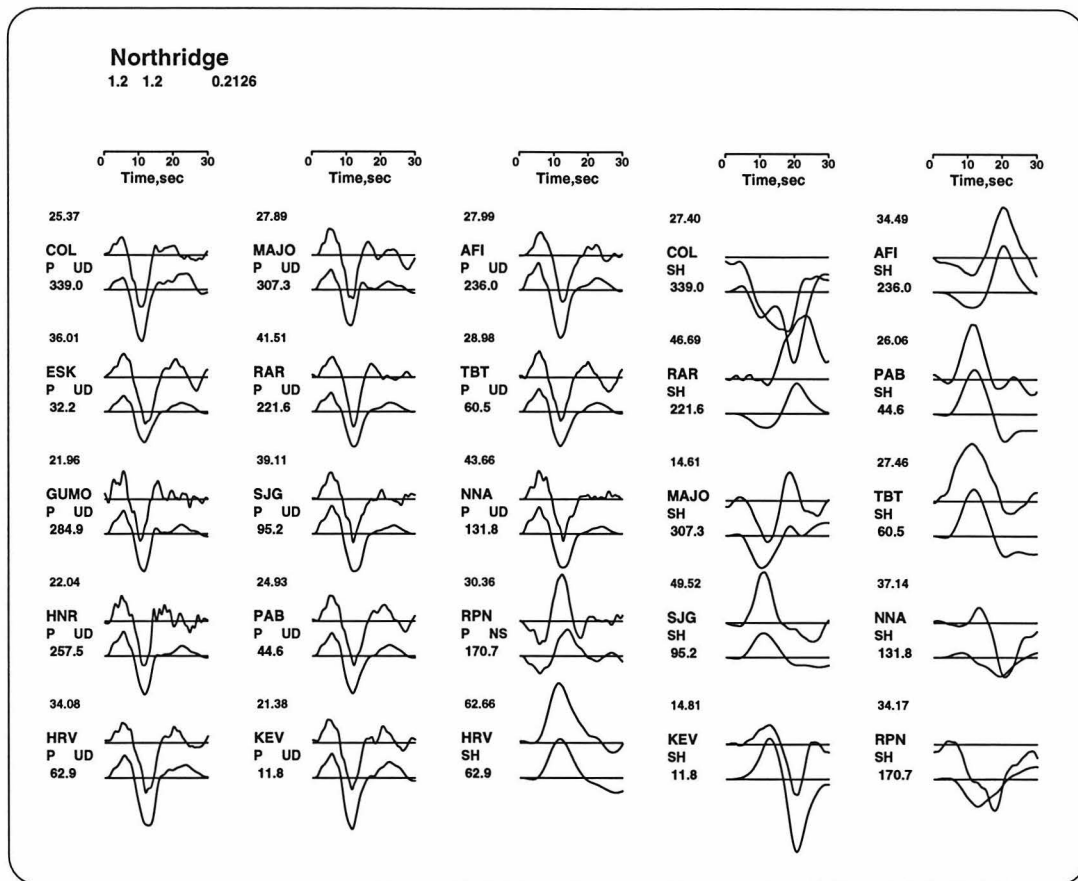


Figure 7. Data (top traces) and synthetic seismograms calculated for the second model (bottom traces).

### Cross section of the Northridge rupture

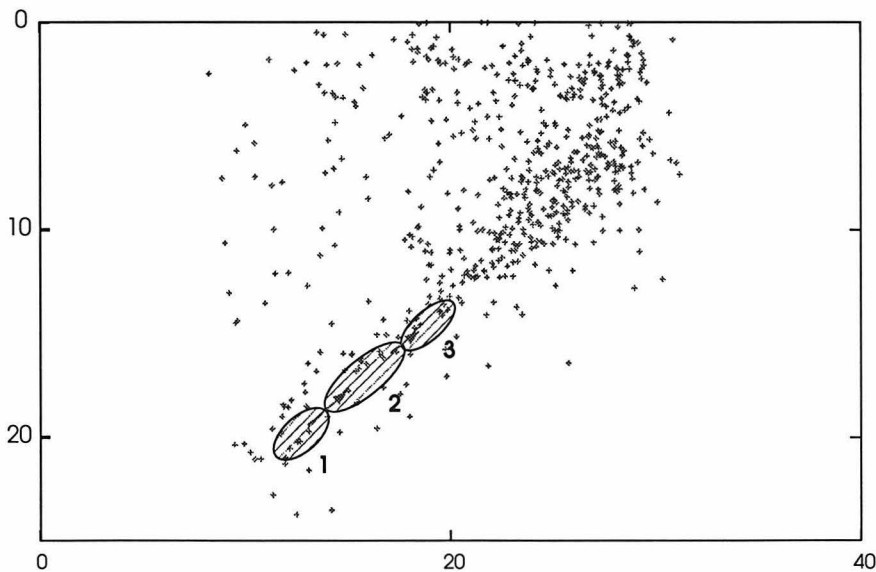


Figure 8. Cross section through the Northridge aftershock zone, perpendicular to the strike of the fault. The ellipses show the location and approximate extent of the subevents which resulted from our inversion.

Hartzell, 1988). If we assume that the rupture extended 10 kilometers in the updip direction as well as laterally, we can estimate the slip on the fault plane using  $M_0 = \mu SD$ , where  $\mu$  (rigidity) =  $3.5 \times 10^{11}$  dyne/cm<sup>2</sup>,  $S$  (fault surface) = 100 km<sup>2</sup> and  $D$  is the displacement. For the average slip we obtain 3 m, which is large for an earthquake of this size; this indicates a relatively high stress-drop. If we compute the stress-drop using a circular crack-model, we obtain an estimate of 270 bar. This is similar to the stress-drops observed on other earthquakes along the Transverse Ranges like the Sierra Madre (460 bar, Dreger & Helmberger, 1992), Whittier Narrows (750 bar, Bent & Helmberger, 1989), Upland (265 bar, Dreger and Helmberger, 1991) and Pasadena (200 bar, Kanamori et al., 1990) earthquakes.

### **Aftershocks**

The Northridge earthquake occurred in the middle of the TERRAscope network so that we have an abundance of high quality very broad-band data. This enabled us to make a systematic study of the source mechanisms of the aftershocks using short-period surface waves. The method of Thio and Kanamori (1995a) is used for this analysis. We present solutions for most aftershocks with  $M_W > 3.5$ , with the exception of events which followed within the first couple of hours after the mainshock, including the largest aftershock which occurred a few minutes after the main event. The records for these events could not be used because of interference with the mainshock.

Since the source dimension of the main shock is relatively large compared to the epicentral distances to the TERRAscope stations, the point source approximation made in our method may not be justified. However, by using some of the more distant stations, we were able to determine the mechanism with sufficient accuracy (fig. 9). The moment of  $1.6 \times 10^{26}$  dyne.cm is larger than that from the body-waves but this may be due to the longer periods involved or to errors arising from the use of the point-source approximation. The best

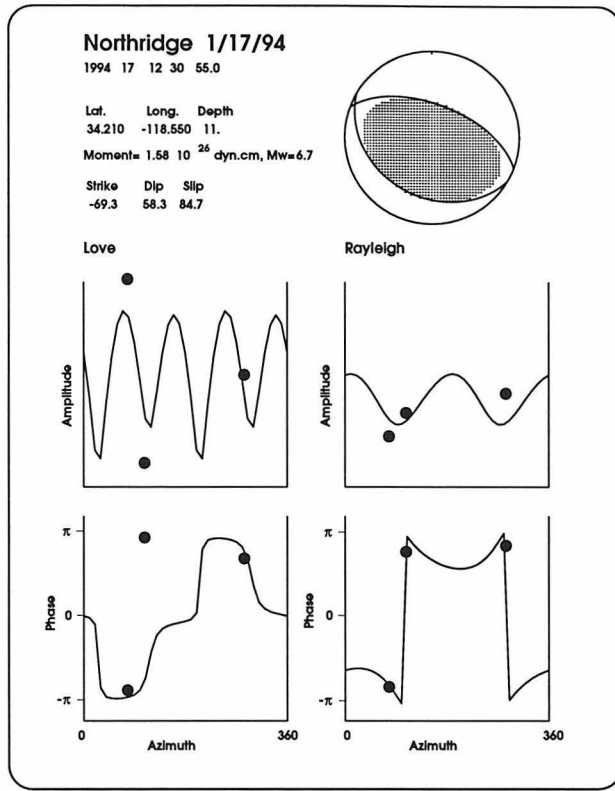


*Figure 9. Moment tensor solution for the Northridge mainshock from short-period surface waves. The bottom panels are the radiation patterns for this solution at a period of 20.48 sec. The dots are the observed values.*

results were obtained with a half-duration of 5 seconds, which is comparable with the body-wave results. The depth however was 11 kilometers, which is substantially shallower than the depth found from the SCSN and our body-wave solution. We think that this is also caused by our point-source approximation.

Our inversion method is more suitable for the analysis of smaller events, and the results for the aftershocks are much more reliable than that for the mainshock. The results are given in appendix A, and plotted in figure 10. The mechanisms of the aftershocks are predominantly thrust, similar to the mainshock mechanism. There are, however, some larger strike-slip aftershocks; in general the strike-slip mechanisms seem to be concentrated near the center of the aftershock area. East of this zone we find thrust mechanisms similar to the mainshock, whereas to the west we find thrust mechanisms which are more oblique than in the eastern zone with more northerly oriented P-axes.

We also compared the  $M_w/M_L$  ratios for the aftershock sequence to see whether there is any

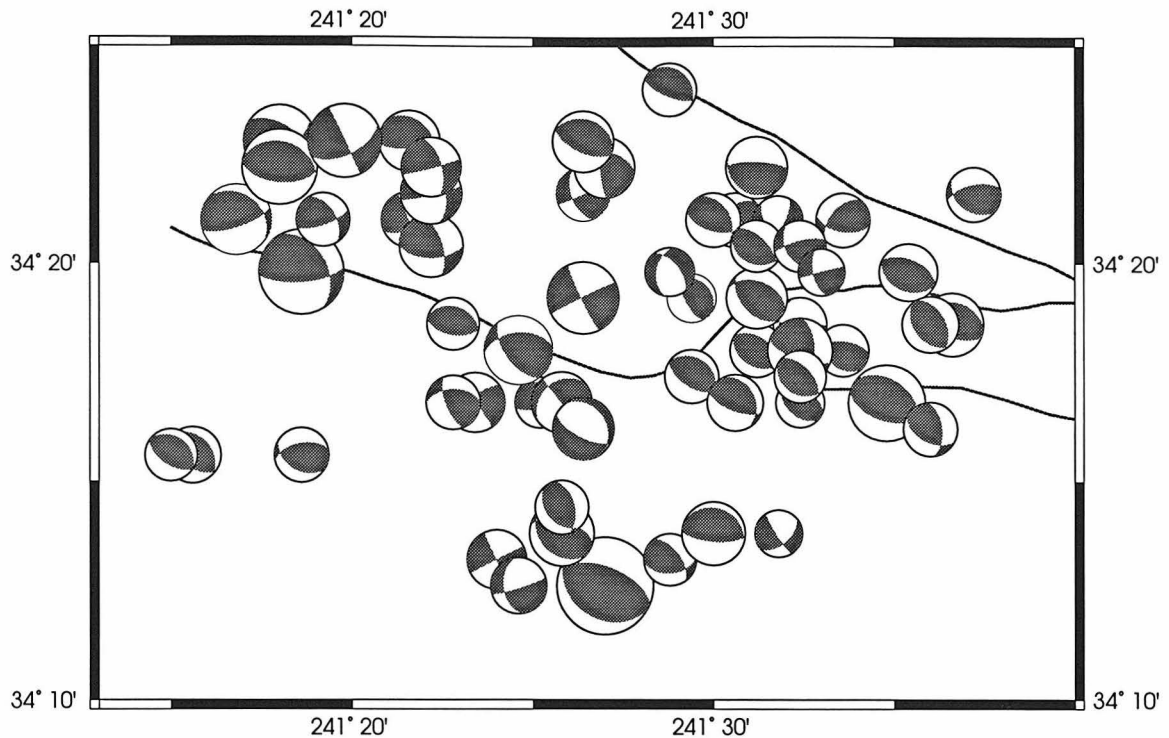
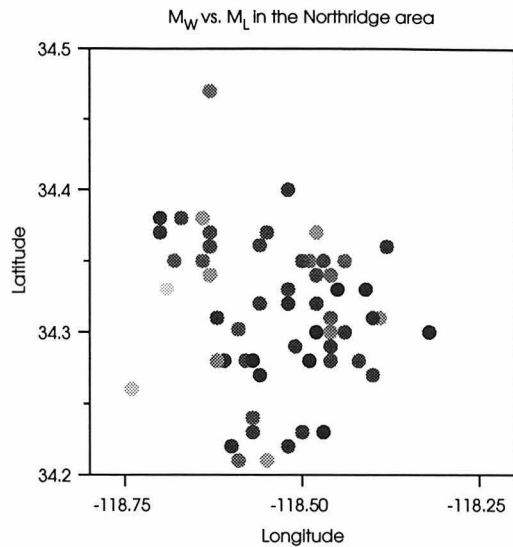


Figure 10. Aftershock mechanisms determined using short-period surface waves.

trend with respect to the locations in the aftershock region, which might indicate differences in stress-drop. However, as can be judged from figure 11 there is no evidence for that from these ratios alone.

## Discussion

Our results for the mainshock rupture are consistent with the results obtained by Wald & Heaton (1994), Dreger (1994), which favor slip occurring at large depths. Our teleseismic inversion results, as well as the results of Wald & Heaton (1994), show no evidence of mechanism changes during rupture, suggesting that the rupture plane is simple in geometry. This is in contrast to the San Fernando earthquake for which Langston (1978) and Heaton (1982) found evidence for a change in dip angle. Further evidence for simplicity of the rupture plane comes from the observation that the aftershocks in the rupture area are very similar in mechanism to the mainshock.



*Figure 11. Variation of the ratio between  $M_L$  and  $M_0$  in the Northridge aftershock area. The dark dots represent high ratios, the light dots represent low ratios.*

Outside the immediate rupture plane however, the fault geometry seems to become more complicated. Mori et al. (1994) concluded that the upper continuation of the rupture plane is cut off by the rupture plane of the San Fernando earthquake which broke to the surface. To the west, our aftershock mechanisms suggest that the fault geometry changes, ultimately resulting in a zone of more east-west striking fault planes separated from the main shock area by a zone with more strike-slip or oblique mechanisms.

We suggest that this change in mechanism is a manifestation of structural complexity that limited the extension of the Northridge rupture. Thio and Kanamori (1995b) observed for several large strike-slip earthquakes that complexity of the structure has a significant influence on the rupture process itself, causing complex rupture time-histories or changes in mechanism. This may also explain the high stress drop of this earthquake. The stress drop of the Northridge earthquake, 270 bars, is high, but, as discussed previously, high stress drops are commonly found for earthquakes in the Transverse Ranges and also for the 1992 Landers earthquake. High stress drop earthquakes are usually associated with relatively long recurrence times of earthquakes, as suggested by Kanamori and Allen (1986) and Scholz et al. (1986). One possible mechanism is that the faults in the Transverse Ranges with low slip rates have not developed into a single throughgoing fault. Faults do not evolve as a single propagating crack, but rather as a system of smaller cracks that progres-

sively grows into a single fault (Scholz, 1989). An example of this is the development of en-echelon faults that are observed in the early stages of strike-slip faults (e.g. Mandl, 1988). Discontinuities in faulting may inhibit propagation of a rupture front, thereby limiting the extent of the rupture zone. This mechanism, combined with a slip-pulse (Heaton, 1990) causes high stress drop events. In the slip pulse model (Heaton, 1990), the slip during rupture occurs in a narrow band and propagates on a fault plane. In general, slip pulses with large displacements tend to propagate over a large distance, which gives rise to the relationship between slip and fault length. However, if the slip is stopped early by irregularities of fault geometry, the ratio of slip to rupture becomes large, resulting in a high stress drop event.

### **Acknowledgments**

We would like to thank Holly Given and Pete Davis for their help in obtaining IRIS/IDA data. This research was supported by the USGS Grant Number 1434-93-G-2287 and NSF Grant Number EAR-9416120.

### **References**

- Bent, A.L., Helmberger, D.V., 1989. Source complexity of the October 1, 1987, Whittier Narrows earthquake. *J. Geoph. Res.*, 94, B7, 9548-9556.
- Dreger, D.S., 1994. Empirical Green's Function Study of the January 17, 1994 Northridge Mainshock ( $M_W=6.7$ ). *Geoph. Res. Lett.*, 21, 2633-2636.
- Dreger, D.S., Helmberger, D.V., 1991a. Complex faulting deduced from broad band mod-
-

- 
- eling of the 28 February 1990 Upland earthquake ( $M_L=5.2$ ). *Bull. Seis. Soc. Am.*, 81, no. 4, 1129-1144.
- Dreger, D.S., Helmberger, D.V., 1991b. Source parameters of the Sierra Madre earthquake from regional and local body waves. *Geoph. Res. Lett.*, 18, no 11, 2015-2018.
- Hauksson, E., Jones, L.M., Hutton, K., 1995. The 1994 Northridge earthquake sequence in California: Seismological and tectonic aspects. submitted to *Journ. Geoph. Res.*
- Heaton, T.H., 1982. The 1971 San Fernando earthquake: a double event? *Bull. Seis. Soc. Am.*, 72, no 6, 2037-2062.
- Heaton, T.H., 1990. Evidence for and implications of self-healing pulses of slip in earthquake rupture. *Phys. Earth Plan. Int.*, 64, 1-20.
- Kanamori, H., 1994. Mechanics of earthquakes. *Ann. Rev. Earth. Plan. Sc.* 22, 207-237.
- Kanamori, H., Allen, C.A., 1986. Earthquake repeat time and average stress drop. In *Earthquake Source Mechanics*, *Geoph. Monograph.* 37, AGU, 227-235.
- Kanamori, H., Mori, J., Heaton, T.H., 1990. The 3 December 1988, Pasadena earthquake ( $M_L = 4.9$ ) recorded with the very broadband system in Pasadena. *Bull. Seis. Soc. Am.*, 80, no 2, 483-487.
- Kanamori, H., Mori, J., Hauksson, E., Heaton, T.H., Hutton, L.K., Jones, L.M., 1993. Determination of earthquake energy release and  $M_L$  using TERRAScope. *Bull. Seis. Soc. Am.*, 83, no 2, 330-346.
- Kikuchi, M., Fukao, Y., 1988. Seismic wave energy inferred from long-period body wave inversion. *Bull. Seis. Soc. Am.*, 78, 1707 - 1724.
- Kikuchi, M., Kanamori, H., 1991. Inversion of complex body waves - III. *Bull. Seis. Soc. Am.*, 81, no. 6, 2335 - 2350.
- Langston, C.A., 1978. The February 9, 1971 San Fernando earthquake: a study of source finiteness in teleseismic body waves. *Bull. Seis. Soc. Am.*, 68, no. 1, 1-29.
-

- 
- Ma, K.F., Kanamori, H., 1991. Aftershock sequence of the 3 December 1988 Pasadena earthquake. *Bull. Seis. Soc. Am.*, 81, no. 6, 2310-2319.
- Mandl, G., 1988. *Mechanics of tectonic faulting: models and basic concepts*. Elsevier Science Pub., Amsterdam, 407 pp.
- Magistrale, H., Kanamori, H., Jones, C., 1991. Forward and inverse 3-dimensional P-wave velocity models of the Southern California crust. *J. Geoph. Res.*, 97, B10, 14,115-14,135.
- Mendoza, C., Hartzell, S.H., 1988. Aftershock patterns and mainshock faulting. *Bull. Seis. Soc. Am.*, 78, no. 4, 1438-1449.
- Dreger, D.S., Helmberger, D.V., 1991. Complex faulting deduced from broad band modeling of the 28 February 1990 Upland earthquake ( $M_L=5.2$ ). *Bull. Seis. Soc. Am.*, 81, 4, 1129-1144.
- Mori, J., Wald, D., Wesson, R., 1994. Overlapping fault planes of the 1971 San Fernando and 1994 Northridge, California, earthquakes. *Geoph. Res. Lett.*, 22, no. 9, 1033-1036.
- Norris, R.M., Webb, R.W., 1990. *Geology of California*. Wiley & Sons, 541pp.
- Scholz, C.H., 1989. Mechanics of faulting. *Ann. Rev. Earth.. Plan. Sc.*, 17, 309-334.
- Scholz, C.H., Aviles, C.A., Wesnousky, S.G., 1986. Scaling differences between large and intraplate earthquakes. *Bull. Seis. Soc. Am.*, 76, 65-71.
- Scientists of the USGS and Southern California Earthquake Center, 1994. The magnitude 6.7 Northridge, California, earthquake of January 17, 1994. *Science*, 266, 389-397.
- Thio, H.K., Kanamori, H., 1995a. Moment tensor inversions for local earthquakes using surface waves recorded at TERRAScope. *Bull. Seis. Soc. Am.*, in press..
- Thio, H.K., Kanamori, H., 1995b. Source processes of large on-land strike-slip earthquakes. in prep.
- Wald, D.J., Heaton, T.H., 1994. A dislocation model of the 1994 Northridge, California,
-

earthquake determined from strong ground motions. USGS open-file report, 94-278.

Whitcomb, J.H., Allen, C.R., Garmany, J.D., Hileman, J.A., 1973. San Fernando Earthquake Series, 1971: Focal Mechanisms and Tectonics. *Rev. Geoph. Sp. Ph.*, 11, no. 3, 693-730.

## Chapter 4:

# Source complexity of large strike-slip earthquakes: the 1990 Rudbar (Iran), Luzon (Philippines) and 1992 Landers (California) earthquakes.

### Abstract

We studied the complexity of the 1990 Rudbar (Iran), Luzon (Philippines) and 1992 Landers (Southern California) earthquakes. All three earthquakes were large strike-slip events that broke the surface. Our results show that there is a good correlation between the source complexity and the observed surface rupture. We conclude that the geometrical complexity of the fault systems contributed to the source complexity, and that the rupture was interrupted because of the occurrence of stronger patches at the step-overs between rupture segments. Since the geometrical complexity is strongly related to the stage of development of a fault system, it is expected that ruptures will become more uniform as fault activity progresses over geologic time. This is demonstrated by the fact that the Luzon earthquake was much smoother than the other two events. The static and dynamic stress drops are high but they are very similar in size and some cases the dynamic stress exceeds the static stress drop. These observations can be explained by a partial stress drop model which is also consistent with observations of high dislocation velocities during the Luzon earthquake, and gives an explanation for the high static stress drops observed for earthquakes with long repeat times. In these earthquakes, slip pulses are more likely to be stopped early because the faults are stronger due to the effect of healing between major earthquakes. This leads to a high ratio of dislocation versus rupture length, which means that the static stress drop is higher.

---

## Introduction

Recent studies of the rupture processes of earthquakes have revealed a wide variety of complexity associated with these events. Some earthquakes show evidence of changes of mechanism during the rupture and complicated source time-functions (e.g. 1988 Armenia earthquake ( $M_S=6.8$ ), Kikuchi et al., 1993; 1989 Ungava earthquake ( $M_S=6.3$ ), Bent, 1994), whereas others, even large events, have smooth time-histories and have a single mechanism throughout the rupture process (e.g. 1992 Nicaragua earthquake ( $M_S=7.0$ ,  $M_W=7.6$ ), Kikuchi & Kanamori, 1993; 1989 Maquarie Ridge earthquake ( $M_S=8.2$ ), Tichelaar & Ruff, 1990). In recent numerical studies on the dynamics of earthquake rupture (Carlson & Langer, 1989; Cochard & Madariaga, 1994) it has been shown that small heterogeneities in the stress field on a fault can cause source complexity. However, others have attributed source complexity to geometrical discontinuities of the faults (e.g. Li et al., 1994; Ben-Zion & Rice, 1995). With this paper we hope to contribute to this discussion by studying the source complexity of several large strike-slip earthquakes. By comparing the source complexity with the surface rupture we show how the fault geometry influences the rupture complexity. We also computed the radiated energy and estimated the dynamic stress drop and static stress drop for the individual rupture segments, as well as the earthquakes as a whole.

We present results of source inversions for three large earthquakes, the 1990 Manjil-Rudbar (Iran,  $M_S=7.6$ ) and Luzon (Philippines,  $M_S=7.8$ ) earthquakes and the 1992 Landers (Southern California,  $M_S=7.6$ ) earthquake (fig. 1). We used teleseismic body waves (P and SH) to study the complexity of the source. This complexity consists of changes in mechanism during rupture, the irregularity of the source-time functions and an uneven distribution of seismic moment release along the rupture plane.

All three earthquakes in this study are on-land strike-slip events and caused large surface ruptures which have been mapped in some detail. This enables us to compare the deformation on the surface with processes which occurred at depth and gives us a more complete

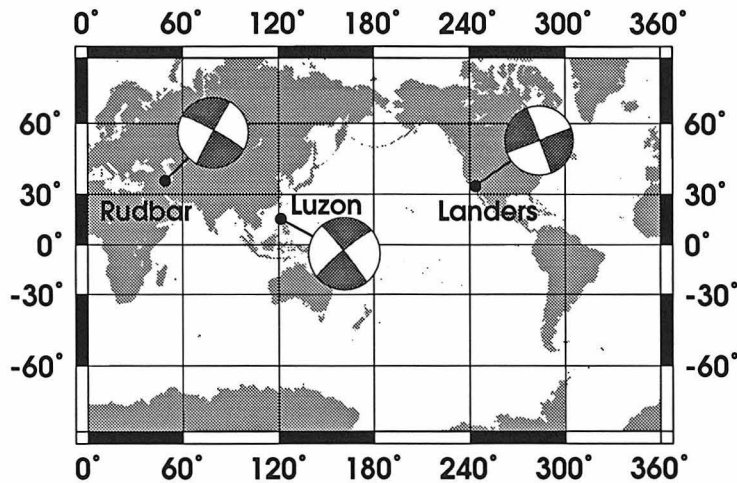


Figure 1. The locations of the earthquakes included in this study.

image of the rupture process which may help us anticipate the character of future earthquakes based on observations in the field and tectonic setting. It also allows us to determine static stress drops for individual rupture segments, which we can then compare to dynamic stress drops which are derived from the rupture model. These earthquakes are comparable, among others, with events like the 1976 Guatemala earthquake ( $M_S=7.5$ ), the 1978 Tangshan earthquake ( $M_S=7.8$ ) and the 1906 San Francisco earthquake ( $M_W=7.7$ ) and we will discuss our results with respect to these and other large strike-slip earthquakes.

The method we used for the inversion is described by Kikuchi and Kanamori (1991) and we shall give a very concise outline of the method below. We also studied several aftershocks of these events, both to determine their relation with the main event and to gain some insight in the influence of source-receiver path structure on the waveforms. The latter proved to be especially important in the case of the Luzon earthquake.

## Method

We model the earthquake rupture as a sequence of subevents. The inversion method that we use determines the timing, location and mechanism for these subevents which are located on a grid. The geometry of the grids used in this study is based on the observed surface rupture. For each different depth separate Green's functions are generated. The dip

and strike and possible curvature of the grid are based on some a priori knowledge about the event, i.e. surface observations or long period moment-tensor inversions. The actual inversion is an iterative process which seeks a maximum in the correlation between the observed records and the Green's functions over a certain time window. This determines the location and focal mechanism for this subevent and subsequently its synthetic waveform is subtracted from the data. We constrained the subevents to be pure double-couples. This process is repeated several times, resulting in one subevent per iteration. The time functions used in this inversion are constrained to be triangular with a certain width. In a second step, however, the solutions obtained earlier are kept fixed and we invert the data for their individual time functions.

In general, source-time functions are dependent on the azimuth and distance of the observing station and the rupture. Only for point-sources are all source-time functions equal. In our case, where the rupture is represented as a series of point-sources, the final source-time function is a simple addition of the individual source-time function of the different point-sources (subevents) without any correction for the location of the subevents. This implies that our final source-time functions are as they would appear at a station with an azimuth perpendicular to the strike of the fault and at a distance of  $90^\circ$ , i.e. at a station which has equal distances to all subevents.

### **Data processing**

The dataset we used in this study consists of P and SH waveforms recorded at teleseismic ( $30^\circ$  to  $100^\circ$ ) distances by very broad band seismometers (fig. 2). In this distance range the effect of propagation is relatively easy to remove. The records were deconvolved to displacement and the P and S wave portions were extracted in windows of about 200 sec at 2 samples per second, for the main events. For the aftershocks we chose denser sampling rates down to 10 samples per second and shorter time windows. We only used the SH

---

## Rudbar earthquake

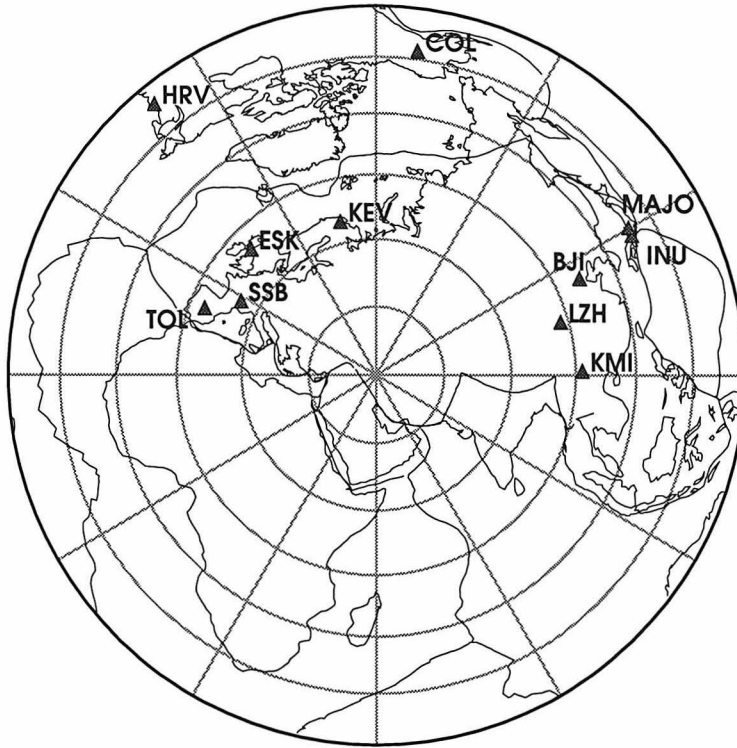


Figure 2a. Azimuthal distribution of the stations used in the inversion for the Rudbar earthquake. The plot is centered on the epicenter, and the distance of the outer rim is 90°.

## Luzon earthquake

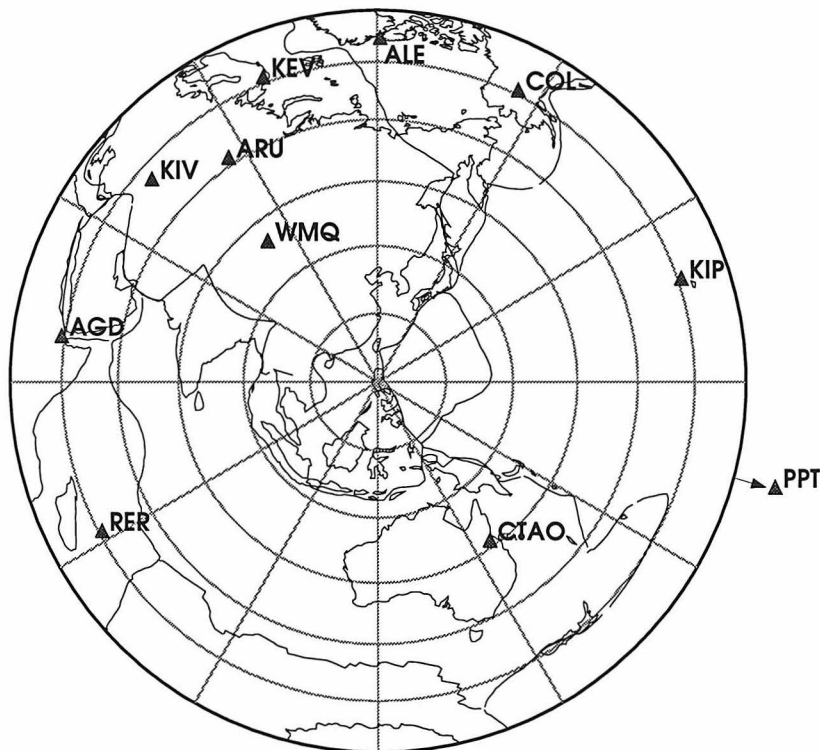
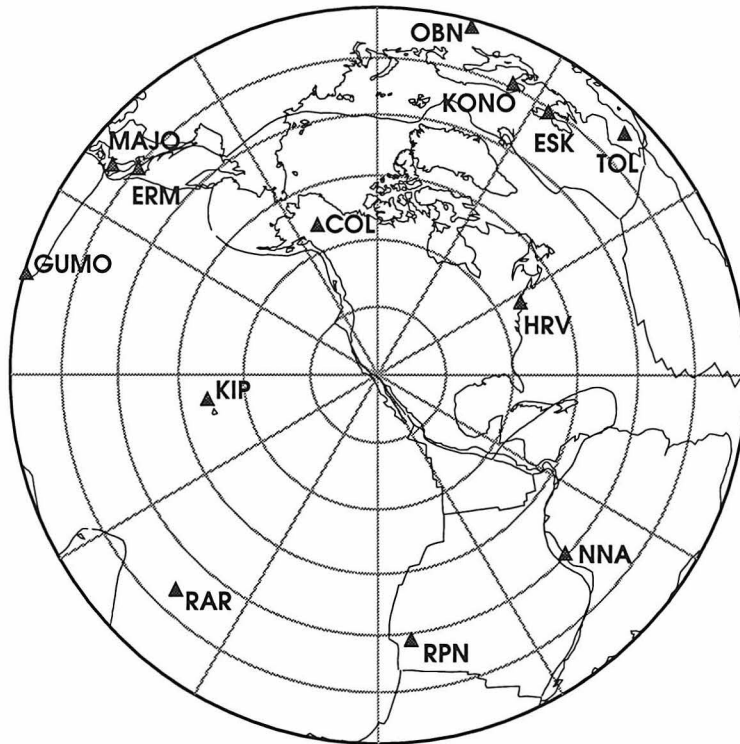


Figure 2b. Same as 2a for the Luzon earthquake.

## Landers earthquake



*Figure 2c. Same as figure 2a for the Landers earthquake.*

component of the S wave because the SV is very often contaminated by S to P conversions near the station. In some cases, where the SH component was small compared to the SV, the SH wave also seemed to be contaminated and those records were not used. The travel-time for the P and S arrivals were calculated using the iasp91 tables (Kennett and Engdahl, 1991) for an epicenter located on the fault as determined from surface observations and closest to the epicenter given by the NEIC. The records were lined up initially according to these arrival times but subsequently small corrections were made to account for the lateral heterogeneity of the earth's structure.

### **The 1990 Rudbar earthquake**

This earthquake occurred on June 20, 1990 and was one of the most devastating in recent times with a death toll of about 40,000. It struck in a densely populated area of Western

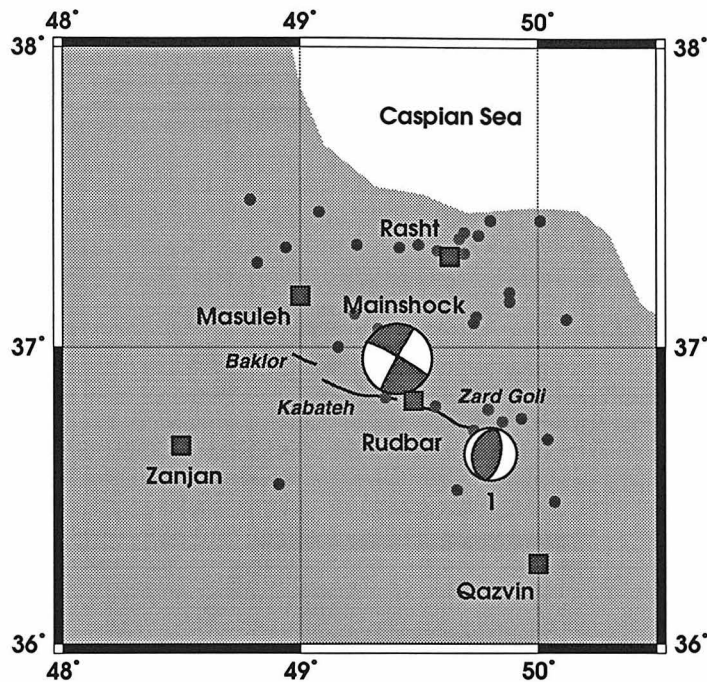


Figure 3. Map of northwestern Iran with the mapped earthquake rupture and the location of the larger aftershocks, taken from the NEIC catalog. The mechanism of the mainshock and that of the largest aftershock are also plotted.

Iran in the Alborz mountains near the city of Rudbar (fig. 3), destroying the cities of Manjil and Rudbar. Strong motion instruments installed in this region within a distance of 100 km registered peak accelerations of over 20%  $g$  and one of the stations which was located a few km from the fault trace registered up to 65% of  $g$ . A surface rupture has been mapped over a length of about 80 km (Berberian et al., 1991) and it consists of three main segments, called the Baklor, Kabateh and Zard-Goli segments, which are arranged in a left-lateral en-echelon, or Riedel, pattern. The lateral offset along the fault as well as the length of the segments increases towards the eastern end of the fault where it amounts to 60 cm.

Iran is believed to be part of a wide zone of deformation between the converging Eurasian and Arabian plates (Jackson & McKenzie, 1988). The deformation is concentrated in three EW trending zones; the Zagros mountains to the south of this area, the Alborz mountains where this event occurred and a more northerly zone under the Caspian Sea. The faults in the present area are primarily thrust faults (Berberian et al., 1991) although a major earthquake to the south, the Buyin Zahra event of 1962 had a significant left-lateral component (Ambraseys, 1963). Based on tectonic models for the area (Jackson & McKenzie,

### Rudbar, 1990

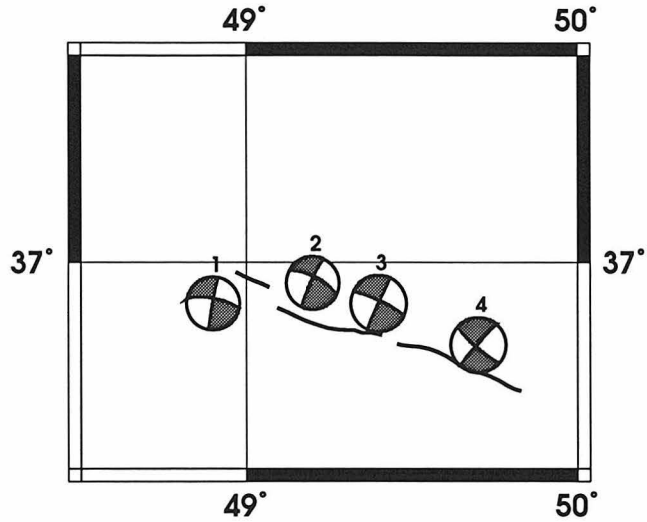
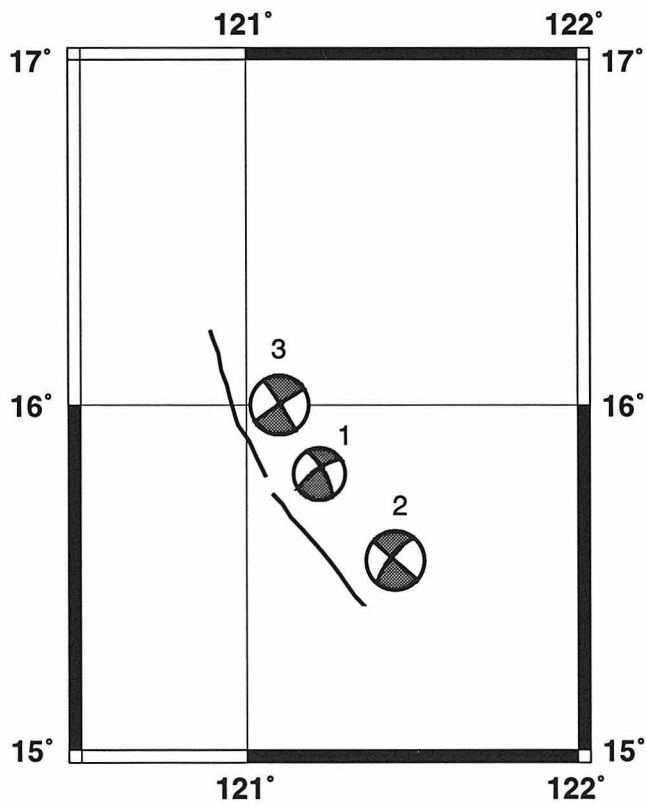


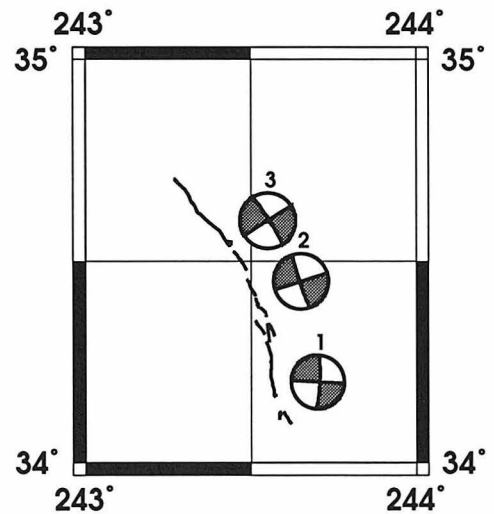
Figure 4. Distribution of subevents and the surface ruptures for the earthquakes in this study. The size of the focal mechanisms is proportional to the magnitude of the subevents.

The numbers correspond to the subevent numbers in the text. a (left): Rudbar earthquake, b (bottom left): Luzon earthquake and c (bottom right): Landers earthquake.

### Luzon, 1990



### Landers, 1992



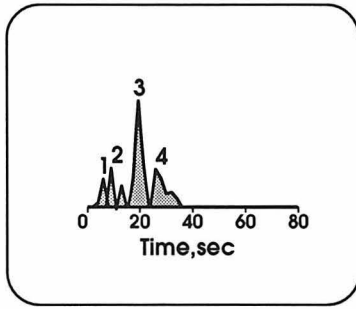


Figure 5. Source-time function for the Rudbar earthquake. The numbers correspond to the numbers of the subevents in figure 4 and in the text.

1988) the slip rate along strike-slip faults is very low, since their orientation is nearly perpendicular to the slip vector. This suggests that the repeat time for earthquakes like the Rudbar event are very long. There are no historical records for large earthquakes in this area and the only indication for a large earthquake comes from archeological excavations (Ambraseys and Melville, 1982) which date back to 1000 BC. This is consistent with the fact that this fault had not been recognized in the field prior to this earthquake (Berberian

	t	$\Delta$	depth	duration	moment	strike	dip	slip
1	0	0	12.5	6	8.9	281	74	2
2	7	15	15	8	15.9	297	71	7
3	13.5	45	10	8	48.9	295	81	1
4	22	60	7.5	12	28.2	131	81	-4

Table 1. Source parameters for the Rudbar earthquake. The numbers in the first column correspond to the numbers in figure 4a and 5.  $t$  - start time of subevent,  $\Delta$  - distance along strike (km). All times in seconds, distance and depth in kilometers and moment in  $10^{26}$  dyne.cm..

et al., 1991).

### Inversion results

Based upon inversion results from long-period surface waves we constrained the subevents along a fault segment with a strike of  $110^\circ$  and a vertical fault plane. We used eight nodes with a separation of 15 km. The depth of the subevents was constrained initially between 5

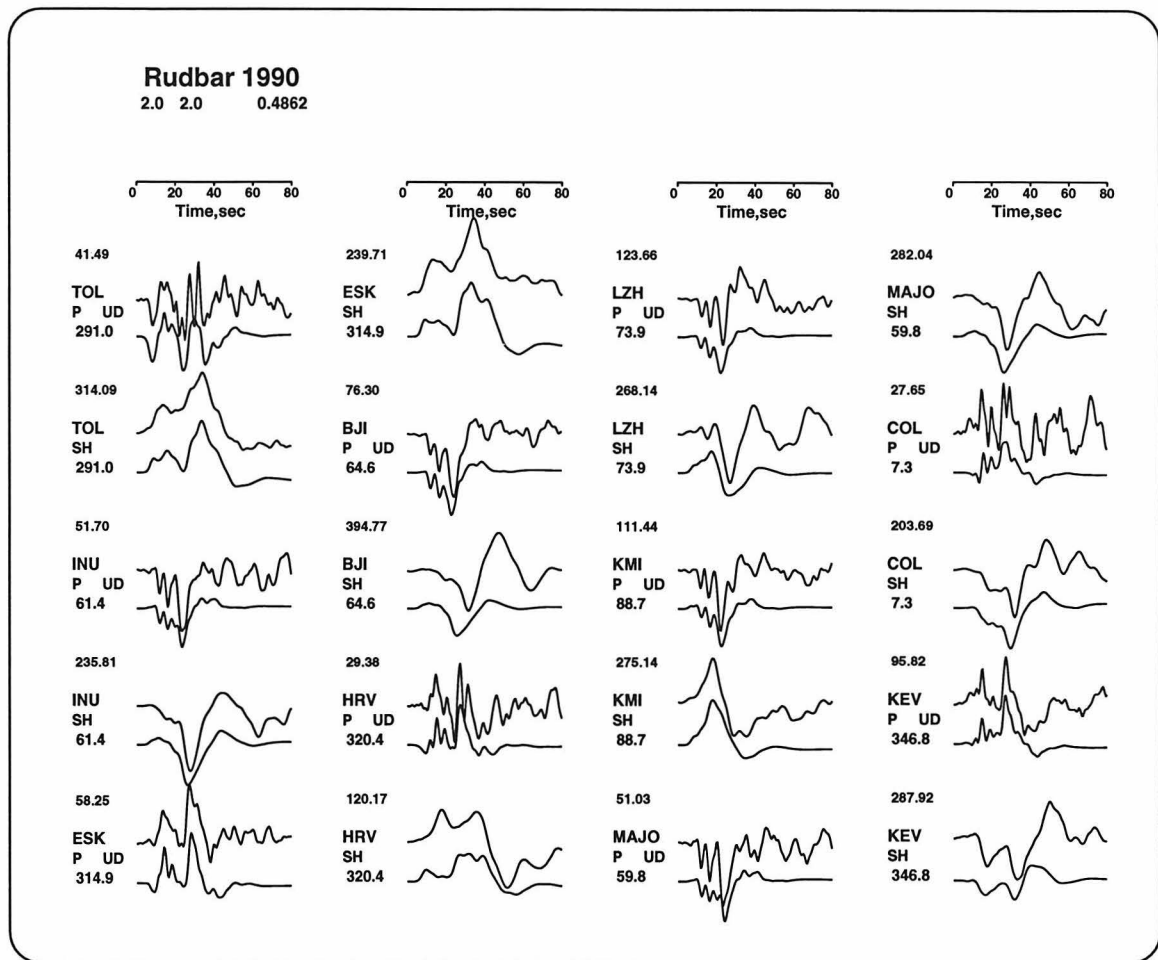


Figure 6. Data (top traces) and synthetic seismograms for the rupture model of the Rudbar earthquake. The seismograms are scaled per station and component.

and 25 km with a separation of 5 km but on the basis of these earlier inversion runs, we constrained the depths between 7.5 and 17.5 km. The only constraint on the mechanism of the subevents was a double couple constraint.

In order to get an optimal fit of the waveforms we needed at least four subevents. The distribution of the subevents is given in fig. 4, with the sequence numbers of the subevents corresponding to those in table 1. The rupture propagates to the south east, and the largest energy release occurs at the end of the rupture, along the easternmost segment. This agrees with the observation that the surface slip and segment length were the largest along the easternmost fault segment. The source-time function (fig. 5) is very irregular, which

	Date	Time	Lat.	Long.	Depth	Strike	Dip	Slip	Moment
M	90/06/20	21:00:09.9	36.96	49.41	10	299	84	2	95.7
1	90/06/21	09:02:14.6	36.64	49.80	7.5	195	31	93	.21

Table 2. Overall source parameters for the Rudbar mainshock and the largest aftershock. Moment in  $10^{25}$  dyne.cm.

indicates that the rupture was not very smooth, but instead may have stopped or slowed down and accelerated during the earthquake process. This irregular rupture is clearly visible in the waveforms (fig. 6). There are small differences in strike for the various subevents. We have tried to fit the observed waveforms by using subevents with identical source parameters but this did not give a satisfactory fit. We therefore conclude that there are subtle changes in mechanism during the rupture. The correspondence between the surface complexity and the rupture complexity suggests that the Riedel pattern on the surface does extend to seismogenic depths. Finally, the total moment derived from the body-waves amounts to  $.95 \times 10^{27}$  dyne.cm, which gives  $M_W = 7.3$ . This is slightly smaller than the CMT solution ( $M_0 = 1.1 \times 10^{27}$  dyne.cm). The Harvard solution has a considerable non-double component but we find no evidence for this. These results are similar to those obtained by Campos et al. (1994).

We also studied the largest aftershock which occurred the next day and had a magnitude of  $M_S = 5.3$ . The waveforms for this event are very simple, consisting of a single arrival with hardly any secondary arrivals later in the records. We inverted this event as a single point source initially and it resulted in a pure thrust mechanism along a NS strike (fig. 3).

### The 1990 Luzon earthquake

The Philippines fault is a major strike-slip fault running over the whole NS length of the Philippines from the southern island of Mindanao to northern Luzon. Definitive evidence for left-lateral movement along the fault was obtained after the 1973 Ragay Gulf earthquake, which had a magnitude of 7.3 and a surface offset of 3.2 meters (Allen, 1975).

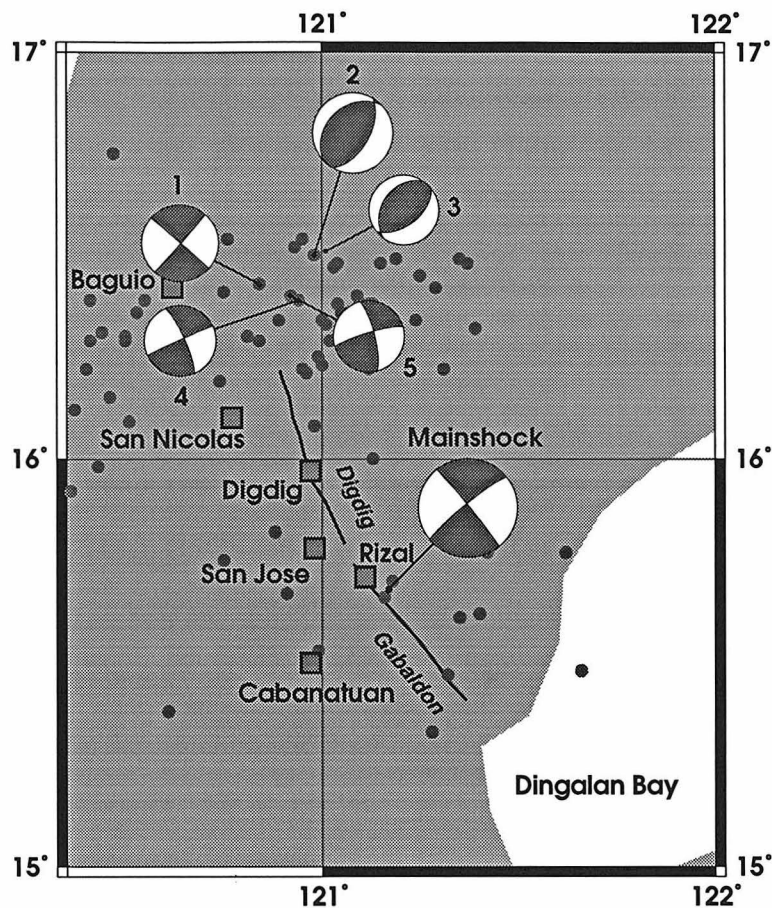


Figure 7. Map of Central Luzon showing the mapped surface rupture (Nakata et al., 1990) and the mechanisms for the mainshock and the aftershocks referred to in the text. The numbers refer to figure 8 and table 3. The italicized names are the names of the fault segments

On the island of Luzon the fault splices into different branches and it is not clear which branch, if any, is dominant. This event occurred on the easternmost branch, called the Digdig fault (Nakata et al., 1977; Ringenbach et al., 1991), which has been mapped all the way up to the northern tip of Luzon, through the Central Cordillera, and might even continue offshore. Historical reports indicate that this area had been struck by a large earthquake in 1627 (Repetti, 1946). These reports specifically mention the Caraballos Mountains, which straddle the Philippines fault and it therefore seems likely that this event took place on the same fault and is not related to the trench systems to the west or east. Slip rates along the northern branch of the Philippines fault are not available, but based on plate reconstruction the convergence rates between the Philippines plate and the Eurasian plate is estimated to be 8 cm/yr (Seno et al., 1993). This movement is partitioned between the trench systems on the eastern (East Luzon trough) and western (Manila trench) sides of the island and the

Philippines fault. It is impossible to determine this partition quantitatively, but given the fact that the orientation of the Philippines fault is close to the slip vector it seems reasonable that the slip rate along the Philippines fault amounts to several centimeters per year (Ringebach et al., 1992). This is consistent with a repeat time of around three hundred years based on the historical records.

This earthquake struck the northern island of Luzon on July 16, 1991. Its mechanism from CMT inversion is left-lateral strike-slip along a NNW-SSE trend. A large surface rupture (fig. 7) with similar sense of shear was mapped by a number of different investigators (Abe, 1990, USGS 1990, Ringebach et al., 1991, Nakata et al., 1990) over a length of at least 120 km, along the Philippines fault, with a maximum displacement of 6 m. The present break coincides with a preexisting fault trace (Nakata et al., 1977, 1990) and in general deformation was confined to a narrow zone of several meters around the fault trace. Most authors have divided the present break into two segments, the northern Digdig segment, of about 60 km length and the southern Gabaldon segment, measuring 50 km in length. These segments are separated by a stretch of about 15-20 km, where very little or no offset was measured. The average offset amounts to 2-3 m along the southern segment and 5-6 m along the northern segment. The epicenter of the earthquake is located in the middle of the southern segment. From the southern end near Dingalan Bay to its northern end near the village of Kayapan the strike of the surface rupture changes from NW-SE to NNW-ESE. There have been reports of local surface breaks not related to the main rupture zone, but there is no evidence for major rupturing along other strands of the Philippines fault system.

### **Data**

We studied both the main event and five of its aftershocks, and some of the teleseismic records are plotted in figure 8 for comparison. The first, fourth and fifth aftershocks as well as the main shock show very complex waveforms with long period ringing lasting well

---

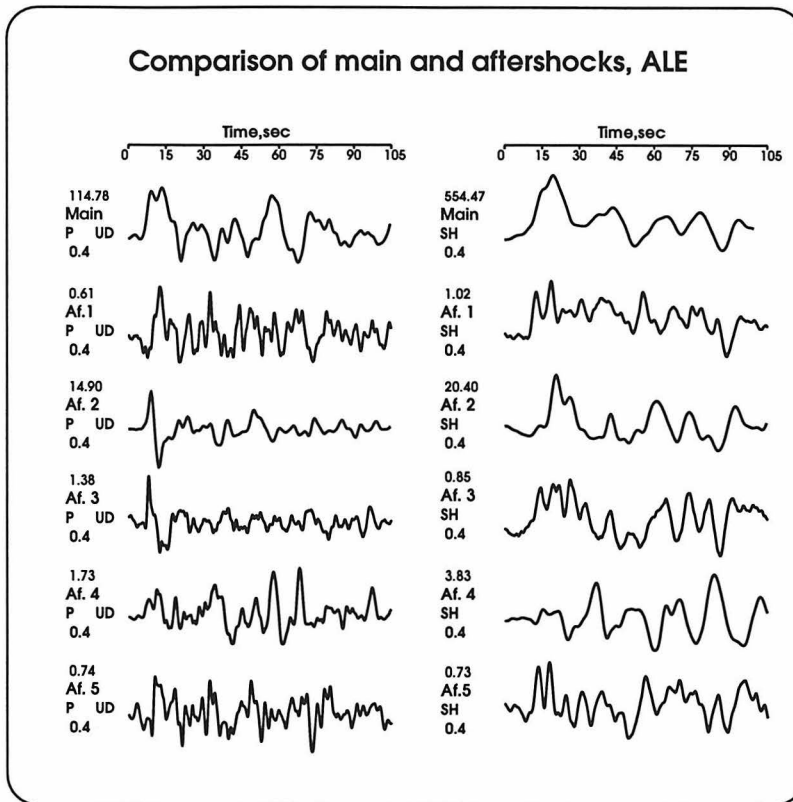


Figure 8a. Displacement seismograms for the Luzon mainshock and aftershock recorded at station ALE. The numbers refer to the numbers in the text and in figure 7.

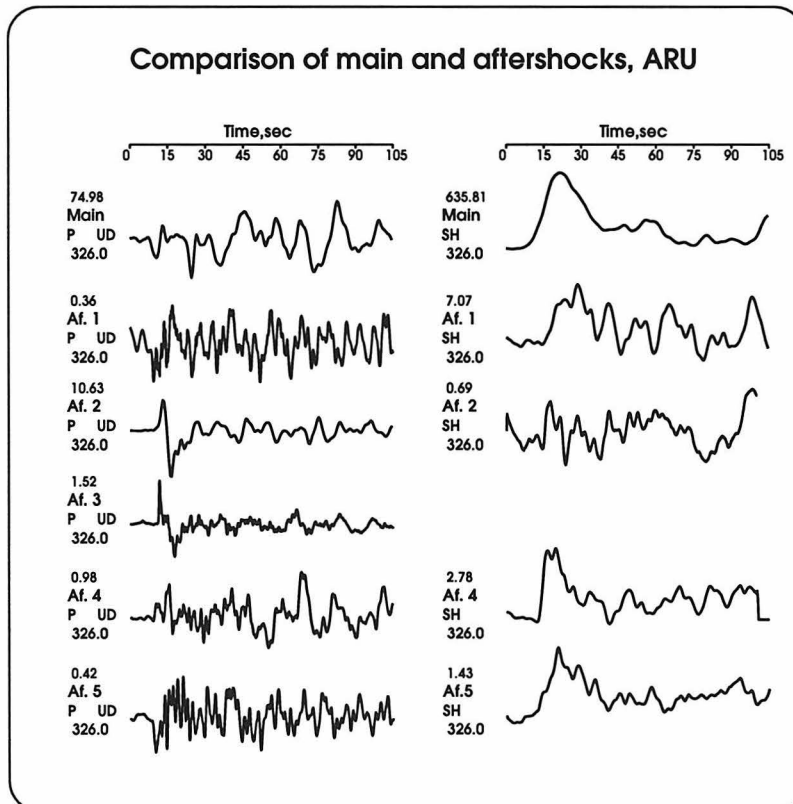


Figure 8b. Same as fig. 8a for station ARU.

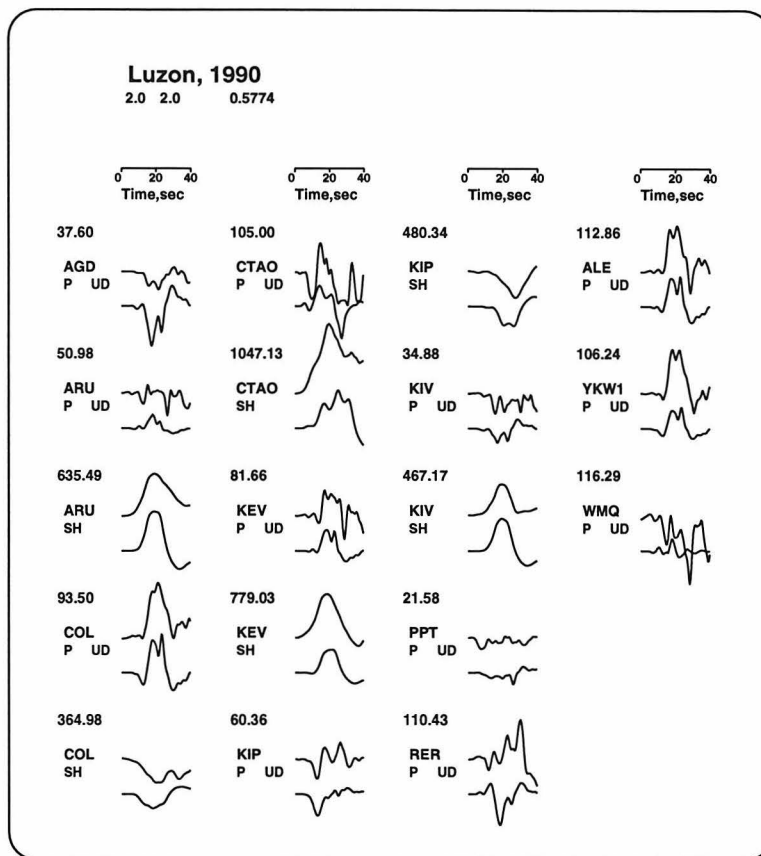


Figure 9. Displacement data (top traces) and synthetic seismograms for the Luzon earthquake.

	Date	Time	Lat.	Long.	Depth	Strike	Dip	Slip	Moment
M	90/07/16	07:26:34.6	15.679	121.171	12.5	321	87	7	261.
1	90/07/17	18:06:35.3	16.43	120.84	9.0	311	89	-2	.74
2	90/07/17	21:14:43.8	16.50	120.98	10.0	227	35	104	2.52
3	90/07/18	08:00:12.8	16.51	121.01	12.5	214	37	75	.12
4	90/07/20	15:11:17.8	16.39	120.94	10.0	336	79	2	.18
5	90/07/21	07:23:35.8	16.40	120.92	11.0	346	76	9	.20

Table 3. Source parameters for the Luzon mainshock and aftershocks. Moment in  $10^{25}$  dyne.cm.

over 60 seconds. The other two aftershocks show relatively clean P waves with some ringing but with much lower amplitudes than the initial arrivals. We generally expect the waveforms of events with magnitudes below 6.5 to be fairly simple because of the short source duration and source dimensions. The observed complexity for some of the Philippines aftershocks therefore needs some special attention because if it is not caused by the source then it must be due to complexity of the earth's structure near the source and

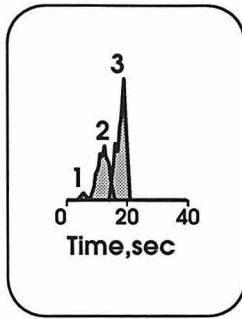


Figure 10. Source time function of the Luzon earthquake. Numbers refer to the subevents in figure 4b and table 4b.

along the path between the hypocenter and the stations. This has profound consequences on the interpretation of waveform complexity in the main shock records in terms of source processes.

To understand the very different character of these records we inverted them for source parameters using a single subevent, thereby effectively assuming that the initial arrival is relatively uncontaminated by noise. The mechanisms are plotted in fig 7 (see also table 3) and if we compare these mechanisms with the waveforms in figure 8, it is clear that the simple records are produced by thrust events, whereas the complex waveforms are related to strike-slip events. It is unlikely that these small strike-slip events have complex sources, especially since the ringing later in the records correlate between different events at the same stations. This effect has been observed before (e.g. Hwang and Kanamori, 1992) and can be explained by the fact that for teleseismic distances the P waves take off near a node in the case for a strike-slip earthquake, in contrast to the case of dip-slip events where the take off angle is near a maximum in radiation. Therefore, the direct P wave is relatively small relative to secondary arrivals which are produced by rays taking off at angles with a stronger radiation. Therefore a strike-slip mechanism has larger potential for multiple reflected or trapped waves in the source region than a thrust event and this may be an explanation for the difference in waveform complexity. The longer period ringing arriving as late as a minute or more into the records suggests that waves are trapped near the source, possible in the sedimentary basins on the island of Luzon or in the trenches which border the island on both the eastern as well as the western side. However, a determination of the

	t	$\Delta$	depth	duration	moment	strike	dip	slip
1	0.0	0	5.0	4	6.7	330	74	16
2	4.0	30	12.5	8.5	97.9	310	90	14
3	9.0	70	12.5	8.5	178	327	87	2

*Table 4. Source parameters for the subevents of the Luzon mainshock. Units as in table 1.*

local structure to model the waveforms falls outside the scope of this paper.

In conclusion, it appears that much of the later arrivals and the ringing in the main-shock records are caused by structural complexity of the source region and not by source-complexity. This casts doubt on interpretations of the data in which the later waveform complexity originates at the source (Thio et al., 1990; Yoshida and Abe, 1992).

### **Inversion**

We choose a curved fault trace, in accordance with the mapped rupture, and the depth interval we used was between 2.5 and 17.5 km. In the light of the discussion in the last section we have limited the inversion to the first thirty seconds of the records, so that we avoid most of the long period ringing. Nevertheless, it is unavoidable that some of the propagation effects will be included in the inversion.

A close look at the records (fig. 9) reveals that the rupture started with a small subevent and was followed after 5 sec by the main energy release. Because the initial event is much smaller than the main energy release, we initially inverted these subevents separately. For the main energy release we found two distinct periods of energy release (fig. 10), the first one starting 4 sec after the beginning of the rupture and the second and largest 9 sec after the beginning (table 4). The mechanisms for these large subevents are rotated by  $17^\circ$  relative to one another, consistent with the changing strike of the surface rupture.

The initial event was located between the large subevents (fig. 4), which indicates a bilateral rupture. The mechanism is more oblique than the large subevents but this may be poorly



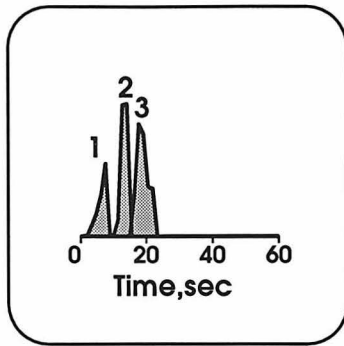


Figure 13. Source-time function of the Landers earthquake. Subevent numbers relate to those in figure 4c and table 5.

constrained because of the influence of the large subevents on the inversion for the initial rupture. The total rupture length from our body-wave inversion is 80 km with a total duration of 20 sec.

### **The 1992 Landers earthquake**

This event occurred in the Eastern California Shear zone north of the San Andreas fault. It broke the surface along different fault strands over a length of 85 km with a maximum displacement of 6 meters (Sieh et al., 1993) (fig. 11). The main segments are the Johnson Valley segment to the south, the Homestead Valley fault in the middle and the Camprock-Emerson faults to the north. This displacement pattern agrees with the displacement pattern deduced from TERRAScope broad-band data by Kanamori et al. (1992) as well as radar interferometric images of the regional displacement field (Massonet et al., 1993). Because of the abundance in seismic instrumentation in Southern California this event has been studied intensively using various methods and data (Wald & Heaton, 1993; Kanamori et al., 1992; Cohee & Beroza, 1993). Our results corroborate both the field investigations as well as the local seismic studies and vindicates the use of teleseismic data to study the complexity of these events.

### **Tectonic setting**

The Eastern California Shear Zone (ECSZ) is a wide zone of deformation between the southern segment of the San Andreas fault and the Owens Valley. It is thought that this

	t	$\Delta$	depth	duration	moment	strike	dip	slip
1	0	0	5.0	8.4	16.2	93	90	7
2	9.4	15	5.0	5.6	30.6	162	86	-180
3	14.4	30	5.0	8.4	38.4	328	86	-179

*Table 5. Source parameters of the Landers subevents. Units similar as table 1.*

	Date	Time	Lat.	Long.	Depth	Strike	Dip	Slip	Moment
M	92/06/28	11:57:34.1	34.20	-116.44	7.3	339	88	-179	79.8

*Table 6. Overall source parameters for the Landers mainshock.*

zone accommodates part, around 15%, of the relative plate-motion between the North American and Pacific plates. Nur et al. (1993) argue that the Landers rupture is part of a newly developing set of faults which represent the emergence of a young throughgoing fault replacing older faults which have rotated to unfavourable orientations for the overall stress field. Sauber et al. (1994) concluded on the basis of geodetic observations that slip rates along the ECSZ are approximately 12 mm/yr. This yields a very long recurrence interval for Landers-type earthquakes, viz. 3500-5000 yr.

## **Inversion**

A first inspection of the teleseismic waveforms (fig. 12) suggests that this event was complex. The P-waves clearly show several pulses of moment release over a time-period of about 30 sec. The P-wave recorded at station KIP shows that this station was close to nodal for the early part of the rupture but not for the later part. This means that the mechanisms has changed during the rupture. Our first inversion results support this observation. Our best results were obtained with a rupture consisting of three subevents, with varying mechanisms, and a rupture propagation from the southern end of the surface rupture, corresponding to the hypocenter, to the north. The source-time function (fig. 13) reflects the different pulses and shows that the rupture is complex although not as irregular as the Rudbar event. The subevents are plotted in figure 4c (table 5), and we clearly see that the

mechanisms follow the changing orientations of the surface rupture. Total moment for this earthquake amounts to  $8.0 \times 10^{26}$  dyne.cm, which is slightly smaller than the moment determined with long-period surface waves which is  $1.1 \times 10^{27}$  dyne.cm.

### Stress-drop

When we calculate the stress-drop for an earthquake, we have to distinguish between dynamic stress-drop,  $\Delta\sigma_d$  and the static stress drop,  $\Delta\sigma$ . The static stress-drop is defined as the difference between the stress on the fault before and after an earthquake and can be calculated for a strike-slip event from the moment and source dimensions using the relation:

$$\Delta\sigma = \frac{2}{\pi} \left( \frac{M_0}{Lw^2} \right)$$

We can define a dynamic stress drop from the moment and the radiated seismic energy:

$$\Delta\sigma_d = 2\mu \frac{E_R}{M_0}$$

In simple earthquake models, where the frictional stress ( $\sigma_f$ ) is equal to the final stress ( $\sigma_1$ ) and where the energy needed to create crack surfaces is negligible, the dynamic stress drop is equal to the static stress drop. In more general cases, where the final and frictional stresses are not equal and the fracture energy is not negligible we have:

$$E_R = W - H - E_C$$

where  $W$  is the total work done during an earthquake,

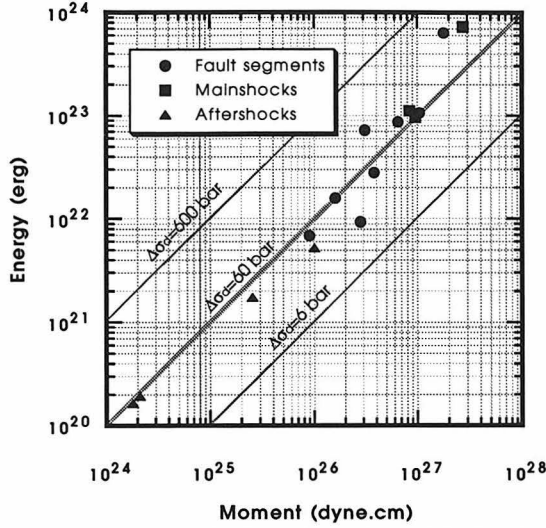


Figure 14. Energy vs. moment for the mainshocks, individual segments and aftershocks for the earthquakes described in this study. The straight lines represent values of constant dynamic stress drop.

$$W = \frac{1}{2}(\sigma_0 + \sigma_1)\bar{D}S,$$

H is the heat produced due to friction on the fault,

$$H = \sigma_f \bar{D}S$$

and  $E_C$  the energy needed to create new crack surfaces. We can write this energy as

$$E_C = \Delta\sigma_C \bar{D}S$$

where we define  $\Delta\sigma_C$  as an apparent stress needed for the formation of new crack surfaces.

Now, we can write the relationship between the static and dynamic stress drops as:

$$\Delta\sigma_C = \Delta\sigma + 2\Delta\sigma_{1f} - 2\Delta\sigma_C$$

with

$$\Delta\sigma_{1f} = (\sigma_1 - \sigma_f)$$

Segment	$M_0$	L	W	$E_R$	$\Delta\sigma_d$	$\Delta\sigma$	$\Delta\sigma_d/\Delta\sigma$
Baklor	.90	11.0	12.5	.69	46.1	33.3	1.38
Kabateh	6.50	30.0	15.0	8.64	79.8	61.3	1.30
Zard-Goli	2.80	36.0	7.5	.94	20.2	88.0	0.23
total	9.57	80.0	12.5	9.73	61.2	49.7	1.23

Table 7. Energy and stress drops for the Rudbar earthquake.

Segment	$M_0$	L	W	$E_R$	$\Delta\sigma_d$	$\Delta\sigma$	$\Delta\sigma_d/\Delta\sigma$
Gabaldon	1.04	48.0	12.5	1.06	61.1	88.3	0.69
Digdig	1.78	57.0	12.5	6.42	216.4	127.2	1.70
total	2.71	115.0	12.5	7.34	162.6	96.0	0.59

Table 8. Energy and stress drops for the Luzon earthquake.

Segment	$M_0$	L	W	$E_R$	$\Delta\sigma_d$	$\Delta\sigma$	$\Delta\sigma_d/\Delta\sigma$
Johnson Valley	1.60	30.0	7.5	1.59	59.6	60.4	0.99
Homestead Valley	3.10	25.0	7.5	7.25	140.3	140.3	1.00
Camprock-Emerson	3.80	35.0	7.5	2.81	44.4	122.9	0.36
total	8.39	80.0	7.5	11.12	79.2	118.7	0.67

Table 9. Energy and stress drops for the Landers earthquake.

Both the dynamic and static stress drops are usually in the range of 1-100 bars (Kanamori, 1994). Large static stress-drops are often associated with earthquakes with long repeat times (Kanamori & Allen, 1986). To compute the static stress drop we determined the source dimensions from the observed surface rupture and the depths from the subevents. The energy  $E_S$ , needed to calculate the dynamic stress drop, is determined from the source time function by integrating the velocity squared field over a sphere around the rupture:

$$E_S = \int_0^{2\pi} \int_0^{\pi} r^2 \sin \vartheta \int_0^{\infty} (\rho\alpha\dot{u}_\alpha^2 + \rho\beta\dot{u}_\beta^2) dt d\vartheta d\phi$$

---

(Kikuchi and Fukao, 1988) where  $u_{\alpha,\beta}$  are the P and S wave velocity fields which include the radiation patterns, the spatial extent and time history of the rupture. We computed the energy, dynamic stress and static stress drops for the different rupture segments as well as for the events as a whole (table 7, 8, 9). In order to make a comparison of the two, we had to assign one or two subevents to each rupture segment for all three earthquakes. Although in some cases this may seem a little arbitrary, the correspondence between the subevents and rupture segments is generally good, and even if we misassigned one subevent it wouldn't influence our conclusions significantly.

The static stress drops range between 33 to 140 bars, which is consistent with results for intra-plate earthquakes. These numbers should be regarded with some caution since the fault dimensions, especially the width of the fault may be underestimated. The dynamic stress drops (fig. 14) are on the same order, although in individual cases they do differ significantly from the static stress drops. In some cases the dynamic stress drop exceeds the static stress drop. In case of a bilateral rupture it is difficult to separate the time functions and if there actually were a larger overlap than suggested in our inversion the energy estimate would decrease, but not by more than a factor of two. On the other hand, our static stress drop estimates may also be on the low side if we have underestimated the fault width. It is safe to say that the dynamic stress drop is not significantly lower than the static stress drop, and that in some cases it exceeds the static stress drop. From equation 4 it is clear that the dynamic stress drop can only exceed the static stress drop if the frictional stress is lower than the final stress state, a situation usually referred to as partial stress drop. This type of behaviour is predicted by rupture models of Brune (1970) and Heaton (1990) among others.

A high dynamic stress drop indicates that the resistance to sliding is relatively low so that sliding velocities are high. We can estimate the dislocation velocities using Brune's (1970) approximation:

---

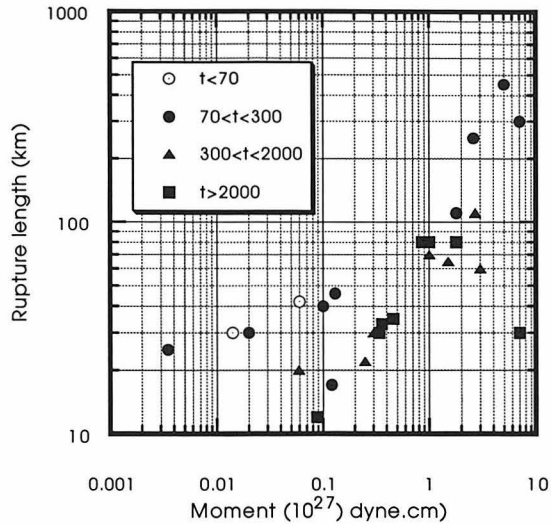


Figure 15. Relation between moment, rupture length and repeat time ( $t$ ) for earthquakes worldwide. Adapted from Kanamori and Allen (1986).

$$\dot{D} = \frac{\beta}{\mu} (\sigma_0 - \sigma_f)$$

For the Luzon earthquake the displacement velocity is then on the order of 1-2 m/sec.

Yomogida & Nakata (1994) determined slip velocities from numerous eyewitness reports and found values in the range of 2.5 to 44 m/sec. Our results therefore are comparable with their lower bounds. It may be that locally the stress drops were much larger than what we determined for the whole fault segment. Also, given the very short observation time (< 2 sec) and the state of mind of most eyewitnesses during a major earthquake, values estimated from eyewitness reports are very uncertain.

Kanamori and Allen (1986) found that stress drop is related to the repeat time of earthquakes. This may reflect the healing process after an earthquake has occurred that increases the fault strength over time. Especially the Landers and Rudbar events would fall in this category. In figure 15 we plotted our results on top of theirs; our events plot in the region of intermediate repeat times.

## Discussion and conclusion

The earthquakes that we studied occurred in very different tectonic regimes. The Rudbar

---

earthquake broke through a very poorly developed or non-existing fault-zone, the Landers earthquake occurred in a pre-existing fault zone with low slip rates and the Luzon earthquake happened on a well-developed and relatively simple fault system with high slip rates. For all three earthquakes, the complexity that we inferred from our inversions matches the complexity observed on the surface rupture. Both the size of the subevents and the mechanisms are consistent with the displacement along the fault segments and the orientation of these segments. From our observations we therefore conclude that fault segmentation can interrupt the rupture process and cause source complexity. It is very likely that it acts as a limiting factor for the extent of the total rupture as well. We believe that the interruption occurs because the energy needed to crack new surfaces is locally too high for the rupture to continue. In the case of pre-existing fault strands this may be caused by a stepover to the next segment.

In some numerical models of rupture processes the complexity arises from small heterogeneities in the stress-field on a fault surface (Cochard & Madariaga, 1994). The complex rupture then leaves a heterogeneous stress-field behind, so that later ruptures are complex as well. In contrast to this dynamically regenerated complexity, in our case the complexity seems to be caused by the fault geometry, which may be influenced by factors not related to the rupture dynamics itself and which evolves with continuing deformation. Faults do not grow as a single expanding crack. Instead, they tend to grow as en-echelon systems (Cloos, 1928; Scholz, 1989; Naylor et al., 1986) which evolve into a single throughgoing crack with progressive deformation. In this simple scheme of fault development, the Rudbar earthquake corresponds to a fault in its very initial stages. The Landers rupture, although it had been mapped previous to the earthquake and shows evidence for prehistoric slip, is made up of different fault strands, separated by stepovers. Li et al. (1994) argue that these step-overs have acted as barriers, causing a slowdown in the rupture propagation. Wald and Heaton (1994) also observed that the rupture decelerated near the stepovers. The Philippines fault on the other hand is a well developed fault, comparable to the Alpine fault

---

---

in New Zealand and the San Andreas fault in California. It has a high slip rate, a very simple surface trace and was recognized as a major fault prior to this earthquake (Allen, 1975). Given the good correlation between the rupture complexity and the complexity of the fault system we conclude that the geometrical complexity is the main factor influencing source complexity. As a fault system evolves over time into a simpler geometry we expect the individual earthquakes on the fault to become simpler as well. It is possible that when fault systems have evolved the source complexity becomes dominated by the source dynamics.

The static stress drops for the earthquakes in this study were all high, which is characteristic of intra-plate earthquakes or earthquakes with long repeat times. This means that the amount of slip is relatively large with respect to the length and width of the fault. The dynamic stress drops are similar to the static stress drops. This may simply mean that very little energy is lost to the creation of new crack surfaces, i.e.  $\Delta\sigma_C=0$ , and that the final stress is equal to the frictional stress so that  $\Delta\sigma_{1f}=0$ . However, the fact that the ruptures are so complex, and the good correlation between the subevents and the fault segments suggests that the creation of new crack surfaces may have played a role in the faulting process. In that case,  $\Delta\sigma_C$  is not negligible so that, in order for the dynamic and static stress drops to be similar,  $\Delta\sigma_{1f}$  must be non-zero (and positive). This means that the frictional stress is lower than the final stress.

As mentioned earlier, the displacement velocities during the Luzon earthquake are on the order of 2 m/sec. Thus, that at any point the actual rupture process was over within a few seconds, much shorter than the total rupture time which is on the order of tens of seconds. This is consistent with the slip-pulse model (Heaton, 1990) in which the slip occurs in a narrow band which propagates along the fault surface. At any point the slip occurs in a very short timespan, much shorter than the overall rupture duration and the slip can cease while the rupture front is still propagating. Therefore, the healing of this slip-pulse is independent from the distance that the rupture front travels. In this model larger slip pulses are more

---

---

difficult to arrest, so that larger displacements give rise to longer rupture lengths. However, if a slip pulse is stopped earlier, for instance because of geometrical irregularities on the fault, then the ratio between displacement and fault length becomes larger, since the rupture length is shorter than in the case where the pulse could have continued to propagate. This means that the static stress drop becomes larger and explains why earthquakes with long repeat times, which are more likely to arrest the propagation of a slip pulse because of geometric complexities, have high static stress drops.

### References

- Abe, K., 1990. Seismological aspects of the Luzon, Philippines earthquake of July 16, 1990. (in Japanese, with english abstract). Bull. ERI, Univ. Tokyo, 65, 851-873.
- Allen, C.R., 1975. Geological criteria for evaluating seismicity. Geol.Soc.Am. Bull., 86, 1041-1057.
- Ambraseys, N.N., 1963. The Buyin-Zahra (Iran) earthquake of September 1, 1962: a field report. Bull. Seis. Soc. Am., 53, 705-740.
- Ambraseys, N.N., Melville, C.P., 1982. A history of Persian earthquakes. Cambridge University Press, 219 pp.
- Ben-Zion, Y., Rice, J.R., 1995. Slip patterns and earthquake populations along different classes of faults in elastic solids. Journ. Geoph. Res, in press.
- Bent, A.L., 1994. The 1989 ( $M_S$  6.3) Ungava, Quebec, earthquake: a complex intraplate event. Bull. Seis. Soc. Am., 84, no 4, 1075-1088.
- Berberian, M., Qorashi, M., Jackson, J.A., Priestly, K., Wallace, T., 1991. The Rudbar-Tarom earthquake of 20 June 1990 in NW Persia: preliminary field and seismological observations, and its tectonic significance. In prep.
- Bischke, R.E, Suppe, J., del Pilar, R., 1990. A new branch of the philippines fault system as observed from aeromagnetic and seismic data. Tectonophysics, 183, 243-264.
-

- 
- Brune, J.N., 1970. Tectonic stress and spectra of seismic shear waves from earthquakes. *J. Geoph. Res.*, 75, 4997-5009.
- Campos, J., Madariaga, R., Nšbùelek, J., Bukchin, B.G., Deschamps, A., 1994. Faulting process of the 1990 June 20 Iran earthquake from broad-band records. *Geoph. Journ. Int.*, 118, 31-46.
- Carlson, J.M., Langer, J.S., 1989. Mechanical model of an earthquake. *Physical Review A*, 40, 6470-6484.
- Cochard, A., Madariaga, R., 1994. Dynamic faulting under rate-dependent friction. *Pageoph*, 142, nr 3/4, 420-445.
- Cohee, B.P., Beroza, G.C., 1993. Slip distribution of the 1992 Landers earthquake and its implications for earthquake source mechanics. *Bull. Seis. Soc. Am.*
- Harding, T.P., 1973. Newport-Inglewood Trend, California - an example of wrenching style deformation. *AAPG bull.*, 57(1), 97-116.
- Haskell, N.A., 1964. Total energy and energy spectral density of elastic wave radiation from propagating faults. *Bull. Seis. Soc. Am.*, 54, 1811-1841.
- Heaton, T.H., 1990. Evidence for and implications of self-healing pulses of slip in earthquake rupture. *Phys. Earth. Plan. Int.*, 64, 1-20.
- Hwang, L.J., Kanamori, H., 1992. Rupture process of the 1987-1988 Gulf of Alaska earthquake sequence. *Journ. Geoph. Res.*, 97, B13, 19,881-19,908.
- Jackson, J., McKenzie, D., 1988. The relationship between plate motions and seismic moment tensors, and the rates of active deformation in the Mediterranean and Middle East. *Geoph. Journ.*, 93, 45-73.
- Kanamori, H., Allen, C.R., 1986. Earthquake repeat time and average stress-drop. In *Earthquake Source Mechanics*, *Geoph. Monograph* 37, 227-235.
- Kanamori, H., Thio, H.K., Dreger, D., Hauksson, E., 1992. Initial investigation of the
-

- 
- Landers, California, earthquake of 28 June 1992 using TERRAScope. *Geoph. Res. Lett.*, 19, no 22, 2267-2270.
- Kanamori, H., 1994. Mechanics of earthquakes. *Ann. Rev. Earth. Planet. Sci.*, 22, 207-237.
- Kennett, B.L.N., Engdahl, E.R., 1991. Travel times for global earthquake location and phase identification. *Geoph. Journ. Int.*, 105, 429-465.
- Kikuchi, M., Fukao, Y., 1988. Seismic wave energy inferred from long-period body-wave inversion. *Bull. Seis. Soc. Am.*, 78, no. 5, 1707-1724.
- Kikuchi, M., Kanamori, H., 1991. Inversion of complex body-waves III. *Bull. Seis. Soc. Am.*, 81, no. 6, 2335-2350.
- Kikuchi, M., Kanamori, H., Satake, K., 1993. Source complexity of the 1988 Armenian earthquake: evidence for a slow after-slip event. *Journ. Geoph. Res.*, 98. no. B9, 15,797-15,808.
- Li, Y.-G., Vidale, J.E., Aki, K., Marone, C.J., Lee, W.H.K., 1994. Fine structure of the Landers fault zone: segmentation and the rupture process. *Science*, 265, 367-370.
- Massonnet, D., Rossi, M., Carmona, C. Adragna, F., Peltzer, G., Feigl, K., Rabaute, T., 1993. The displacement field of the Landers earthquake mapped by radar interferometry. *Nature*, 364, 138-142.
- Matsumoto, N., Yomogida, K., Honda, S., 1992. Fractal analysis of fault systems in Japan and the Philippines. *Geoph. Res. Lett.*, 19-4, 357-360.
- Nakata, T, Sangawa, A, Hirano, S., 1977. A report on tectonic landforms along the Philippine fault zone in the Northern Luzon, Philippines. *Sci. Rep., Tohoku Univ.*, ser. 7, 27:2, 69-93.
- Nakata, T., Tsutsumi, H., Punongbayan, R., Rimando, R., Daligdig, J., Daag, A., 1990. Surface faulting associated with the Philippines earthquake of 1990. (in Japanese) *Geological Journal*, 99, no. 5, 95-112.
-

- 
- Naylor, M.A., Mandl, G., Sijpestein, C.H.K., 1986. Fault geometries in basement-induced wrench faulting under different initial stress states. *J.Struct.Geol.*, 7(8), 737-752.
- Nur, A., Ron, H., Beroza, 1993. The nature of the Landers-Mojave earthquake line. *Science*, 261, 201-203.
- Niazi, M., 1969. Source dynamics of the Dasht-e Bayaz earthquake of August 31, 1968. *Bull. Seis. Soc.* 59, no. 5, 1843-1861.
- Repetti, W.C., 1946. Catalogue of Philippine earthquakes, 1589-1899. *Bull. Seis. Soc. Am.* 36-3, 133-372.
- Ringenbach, J-C., Pinet, N., MUYCO, J., Billedo, E., 1991. Analyse de la rupture associée au séisme du 16 juillet 1990 le long de la faille Philippine (Luzon, Philippines) (with english abstract). *C.R.Acad.Sci.Paris*, t. 312, Série II, 317-324, 1991.
- Ringenbach, J-C., Pinet, N., Delteil, J., Stephan, J-F., 1992. Analyse des structures engendrées en régime décrochant par la séisme de Nueva Ecija du 16 juillet 1990, Luzon, Philippines. *Bull. Soc. Geol. France*, t. 163, no 2, 109-123.
- Sauber, J., Thatcher, W., Solomon, S.C., Lisowski, M., 1994. Geodetic slip rate for the eastern California shear zone and the recurrence time of Mojave desert earthquakes. *Nature*, 367, 264-266.
- Scholz, C.H., 1989. Mechanics of faulting. *Ann. Rev. Earth Plan. Sc.*, 17, 309-334.
- Seno, T., Stein, S., Gripp, A.E., 1993. A model for the motion of the Philippine Sea Plate consistent with NUVEL-1 and geological data. *Journ. Geoph. Res.*, 98, B10, 17,941-17,948.
- Sieh, K., Jones, L., Hauksson, E., Hudnut, K., Eberhart-Phillips, D., Heaton, T., Hough, S., Kanamori, H., Lilje, A., Lindvall, S., McGill, S.F., Mori, J., Rubin, C., Spotila, J.A., Stock, J., Thio, H.K., Treiman, J., Wernicke, B. and Zachariasen, J. (1993). Near-field investigations of the Landers earthquake sequence, April to July 1992. *Science*, 260, 171-176.
-

- Tanioka, Y., Johnson, J.M., Laforge, R., Satake, K., Ruff, L., 1992. Rupture process of the 1990 Philippine earthquake. *EOS*, 73, no. 14.
- Thio, H.K., Satake, K., Kikuchi, M., Kanamori, H., 1990. On the Sudan, Iran and Philippines earthquakes of 1990. *EOS*, 71, no. 43, 1438-1438.
- Tichelaar, B.W., Ruff, L.J., 1990. Rupture process and stress-drop of the great 1989 Maquarie Ridge earthquake. *Geoph. Res. Lett.*, 17, no 7, 1001-1004.
- Wald, D.J., Kanamori, H., Helmberger, D.V., 1992. Source study of the 1906 San Francisco earthquake. *Bull. Seis. Soc. Am.*, 83, 981 - 1019.
- Wald, D.J., Heaton, T.H., 1993. Spatial and temporal distribution of slip for the 1992 Landers, California earthquake. *Bull. Seis. Soc. Am.*, 84, no. 3, 668 - 691.
- Yomogida, K., Nakata, T., 1994. Large slip velocity of the surface rupture associated with the 1990 Luzon earthquake. *Geoph. Res. Lett.*, 21, no. 17, 1799-1802.
- Yoshida, Y., Abe, K., 1992. Source mechanism of the Luzon, Philippines earthquake of July 16, 1990. *Geoph. Res. Lett.*, 19, no. 6, 545-548.
-

## Chapter 5:

### A short note on earthquake energy

#### Abstract

The relationship between seismic moment and radiated energy for earthquakes in Southern California is non-linear. This is contrary to what is expected for earthquakes which are dynamically similar. The non-linearity can be explained by a moment dependence of the specific fracture energy, which is inherent in barrier type rupture models, but it can also be a result of more complex frictional behaviour during rupture, which occurs in rupture models with partial stress-drop.

#### Introduction

In studies of the seismic source it is now common practice to determine its size with the seismic moment ( $M_0$ ), which is a measure of the difference in physical state of the medium before and after an earthquake has occurred. This is evident from the definition for the seismic moment:

$$M_0 = \mu S \bar{D} \tag{1}$$

Both the surface area of the fault  $S$  and the average dislocation  $D$  are static variables. On the other hand the radiated energy of an earthquake is a dynamic quantity that depends on processes during the rupture, like the behaviour of the frictional stress and the velocity with which the crack-tip propagates. Over the years, several studies have been made on the relation between radiated energy, magnitude and moment of earthquakes (e.g. Thatcher & Hanks, 1973; Kikuchi & Fukao, 1988; Singh & Ordaz, 1994). The relation between

---

moment and energy has so far been regarded as linear, with deviations from linearity presumably caused by differences in stress drop that, among others, reflects the tectonic environment. The scatter among different studies is quite large. For example, estimates for the radiated energy of the 1985 Michoacan earthquake (Kikuchi & Fukao, 1988; Ruff & Miller, 1994; Singh & Ordaz, 1994) differ by more than an order of magnitude. These differences may be caused by different methods being used (e.g. local or teleseismic methods) or limited bandwidth of the data. Recently, with the introduction of very broad band instrumentation both worldwide and in dense local arrays the methods for determining these quantities have improved considerably. Kanamori et al. (1993) determined the energy for local Southern California earthquakes and found a very good correlation between local magnitude ( $M_L$ ) and energy. They also present moment and energy estimates for a few selected Southern Californian events. Thio and Kanamori (1995a) developed a method to determine moments for local earthquakes on a routine basis for earthquakes in Southern California. Furthermore, Thio and Kanamori (1995b, 1995c) determined moment and energy for the 1992 Landers and 1994 Northridge earthquakes. In this paper we present a compilation of the above results for earthquakes in Southern California, so that we can reduce the scatter due to different environments, but still have a large magnitude range over which we can observe the relation between energy and moment. We will show that this relation is not linear, but that the energy over moment ratio increases with increasing size of the earthquakes.

## Theory

If we define the initial stress as  $\sigma_0$  and the final stress as  $\sigma_1$ , then the total work done during an earthquake is:

$$W = \frac{(\sigma_0 + \sigma_1)}{2} \bar{D}S \quad (2)$$

where  $S$  is the rupture area and  $D$  average displacement. Part of this energy is released as heat,  $H$ , that is generated due to friction on the fault:

$$H = \sigma_f \bar{D} S \quad (3)$$

where  $\sigma_f$  is the frictional stress. Energy is also lost due to the creation of new crack surfaces. To facilitate the discussion we introduce an apparent stress, the crack stress ( $\Delta\sigma_C$ ), which is related to the crack energy,  $E_C$ , by:

$$E_C = \Delta\sigma_C \bar{D} S \quad (4)$$

The remaining energy,  $E_R$ , is radiated as seismic waves,

$$E_R = W - H - E_C = \frac{1}{2} S \bar{D} [(\sigma_0 - \sigma_f) + 2(\sigma_1 - \sigma_f) - 2\Delta\sigma_C] \quad (5)$$

If we define the static stress drop,  $\Delta\sigma = \sigma_0 - \sigma_1$  and  $\Delta\sigma_{1f} = \sigma_1 - \sigma_f$ , we can write the energy-moment ratio as:

$$\frac{E_R}{M_0} = \frac{1}{2\mu} (\Delta\sigma + 2\Delta\sigma_{1f} - 2\Delta\sigma_C) \quad (6)$$

In a smooth rupture model, where the specific crack energy,  $G_C$ , is constant over the entire fault area, the crack energy ( $E_C = G_C S$ ) is dependent on the fault surface which scales as  $L^2$  whereas the other energy forms scale as  $L^3$ . Thus, the crack energy becomes negligible for large earthquakes. This is also clear if we write the crack formation stress as a function of the specific crack energy:

$$\Delta\sigma_C = \frac{G_C}{\bar{D}} \quad (7)$$

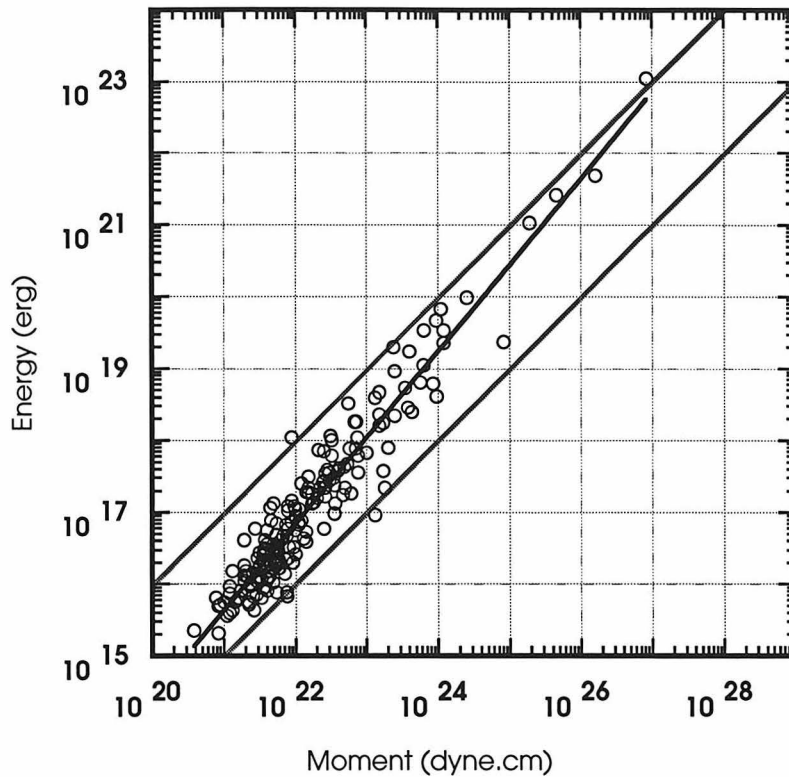


Fig.1. Moment vs radiated energy for earthquakes in Southern California. The thick line is the best fit with a slope of 1.2.

## Data

Kanamori et al. (1993) determined the radiated energy for earthquakes in Southern California and found a very good correlation between local magnitude ( $M_L$ ) and the radiated energy:

$$\log E_R = 1.96 M_L + 9.05 \quad (8)$$

This relationship is valid for events up to magnitude 6 at least. Thio and Kanamori (1995a) determined seismic moments for earthquakes in the same region using surface waves, and found that the data satisfy the relation between magnitude and moment:

$$\log M_0 = 1.5 M_L + 16.0 \quad (9)$$

which has been established in earlier works (e.g. Thatcher and Hanks, 1973). Combining these two equations, we find that the energy/moment ratio is not constant but depends on the size of the earthquake:

$$\frac{E_R}{M_0} \propto M_0^{1/3} \quad (10)$$

In figure 1 we plot the moment vs. energy for Southern California earthquakes. Most moments were determined by Thio and Kanamori (1995a) and the energies were determined from  $M_L$  using equation 8. For some of the larger events (Northridge, Landers) the moments were determined from teleseismic body waves using the method of Kikuchi and Kanamori (1993) and the energies were determined from the rupture models for these earthquakes using the method of Kikuchi and Fukao (1988) (Thio and Kanamori, 1995b,c). Other local energy estimates are directly taken from Kanamori et al. (1993). For events for which we had both teleseismic as well as local energy determinations (Northridge, Landers) we find a very good agreement. For this whole dataset we find:

$$E_R \propto M_0^{1.2} \quad (11)$$

which is different from equation 3, but it is clear from fig. 1 that  $E_R \propto M_0$  does not provide a fit to the data.

## Discussion

If we compare our results with those from other studies it is evident that there are systematic differences between them. Boatwright et al. (1991), and also Fletcher and Boatwright (1991), determined energy and moment for aftershocks of the Loma Prieta earthquake. Their results show an energy moment ratio which is proportional to  $M_0^{1/3}$ , which is similar

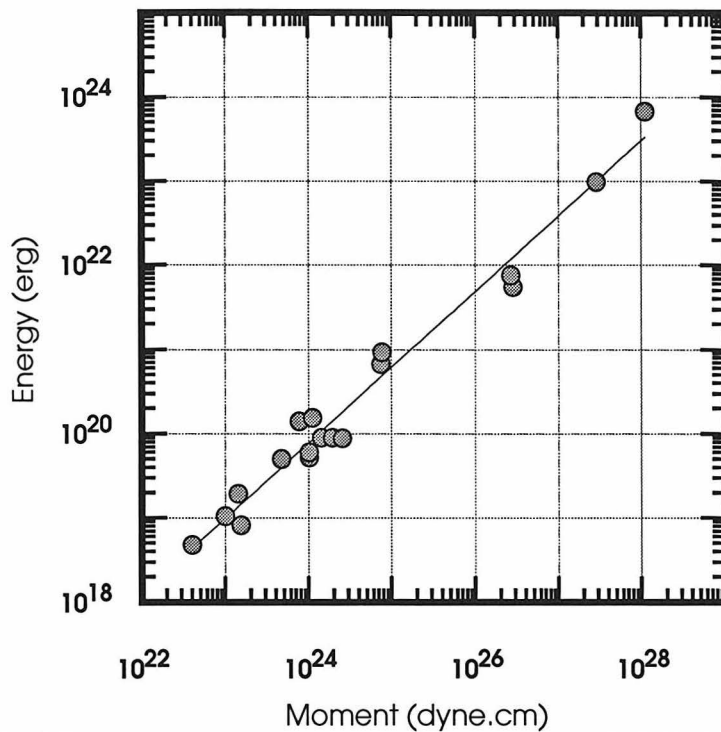


Fig. 2. Moment vs. energy for Mexican events, taken from Ordaz & Singh (1994). The solid line is the fit to the data with slope 0.9.

to our results. However, all the energies are systematically higher than our results by an order of magnitude. This may reflect a difference in seismic structure. Singh and Ordaz (1994) determined energy and moment for a number of Mexican subduction zone earthquakes. Their results (fig. 2) are consistent with a linear relationship (i.e. constant ratio) between moment and energy. Ruff and Miller (1994) found much lower energy/moment ratios in their study of Mexican earthquakes using teleseismic data. Likewise, in a systematic study of events worldwide, Kikuchi and Fukao (1988) found ratios which are much smaller than those found in our study.

It has been suggested (Singh & Ordaz, 1994) that attenuation can cause the non-linear relation between moment and energy. However, this effect has been corrected for by Boatwright et al., (1991) who studied small earthquakes and should not affect our results significantly above magnitude 3.5. Recently, Abercrombie (1995) presented energy and moment relations for small ( $M_L < 3.5$ ) earthquakes recorded in the Cajon Pass borehole. She found a similar relationship between moment and energy as presented here and concluded

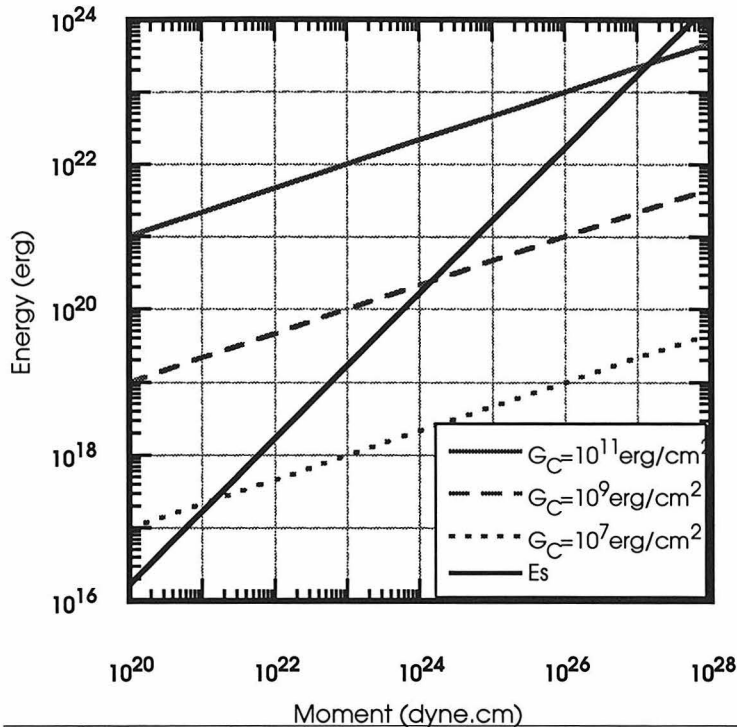


Fig. 3. Crack energies computed for different values for the specific crack energy. The dark line is the radiated energy calculated for a complete stress-drop model with negligible crack energy. All energies are calculated with a static stress-drop of 100 bar.

that even for these small earthquakes attenuation cannot explain the non-linearity. Given the scatter in energy and moment observations for datasets which include events from different regions, it is difficult to tell whether the energy/moment ratio is dependent on earthquake size or not. However, with our observations limited to Southern California for which an abundance of high quality data is available, it is clear that there is a size dependence on the ratio between energy and moment.

There are several processes which might lead to a moment dependent ratio and we will discuss a few of them here. Assuming that the static stress drop is independent of earthquake size, we can identify two terms in equation 6 which can cause the moment dependence, viz., the crack formation stress (i.e. the crack energy), and  $\Delta\sigma_{1f}$ .

Estimates for the specific fracture energy ( $G_C$ ) range from  $10^3$  to  $10^{11}$  erg/cm<sup>2</sup> (Kostrov & Das, 1988). The largest values are derived from seismic data on the assumption that rupture was arrested by a barrier (Aki, 1979) and represents the fracture energy of the barrier and

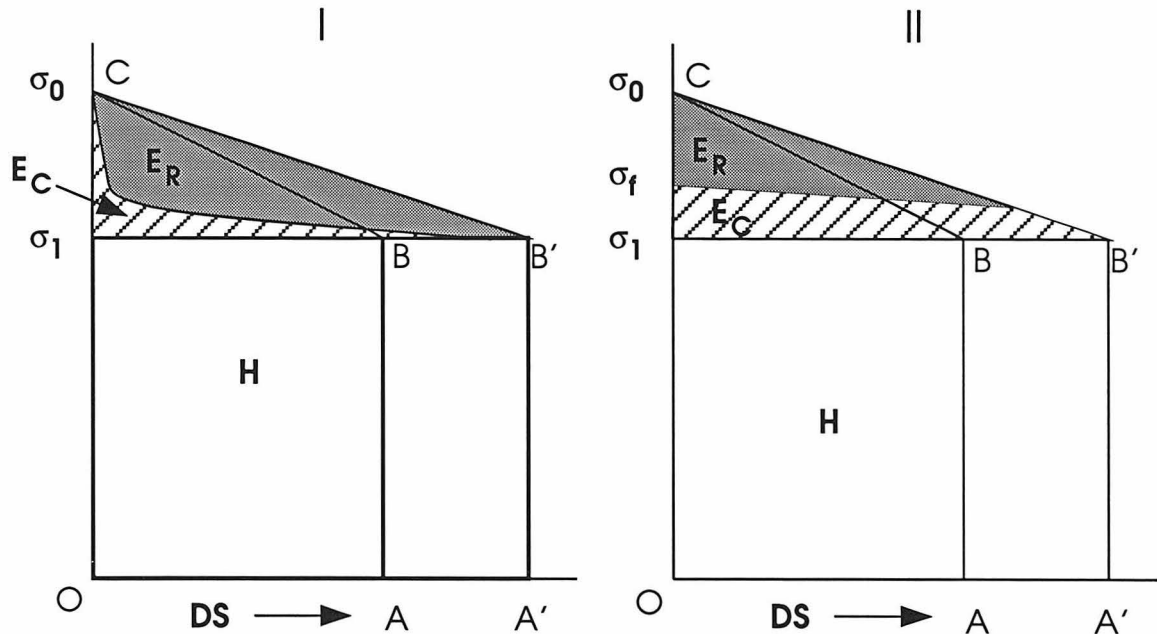


Fig 4. Diagrams showing the contribution of the crack formation to the total energy. The whole areas  $OABC$  or  $OA'B'C$  are the total work done during the earthquakes. The hatched areas represent the fracture energy, and the shaded area is the radiated energy. In case I the specific fracture energy is independent of size and it is clear that for larger earthquakes the crack energy becomes negligible. In case II the crack stress decreases less rapidly than in case a, which means that the specific crack energy increases with moment.

therefore may not be representative of the average energy needed to create crack surfaces during rupture. Husseini (1977) estimated values for the specific fracture energy to be on the order of  $10^8$  erg/cm<sup>2</sup>. Many estimates for  $G_C$  are based on determinations of the rupture velocity since, in theoretical models, the velocity relates directly to the energy needed in the formation of crack surfaces. If the energy is negligible, the rupture velocity varies between the shear velocity, where the slip and rupture directions are perpendicular (anti-plane), and the Rayleigh wave velocity, where rupture and slip are parallel (plane). The rupture velocities decrease as the crack energy increases. However the rupture velocity is generally not very accurately determined. In fig. 3 we plot the crack energy vs. moment for various values for  $G_C$ . It is clear that at some point for the higher estimates of  $G_C$  the crack energy will exceed the available energy. Another illustration of this effect is in figure 4a. Here, the stress states of an earthquake are plotted including the contribution of the

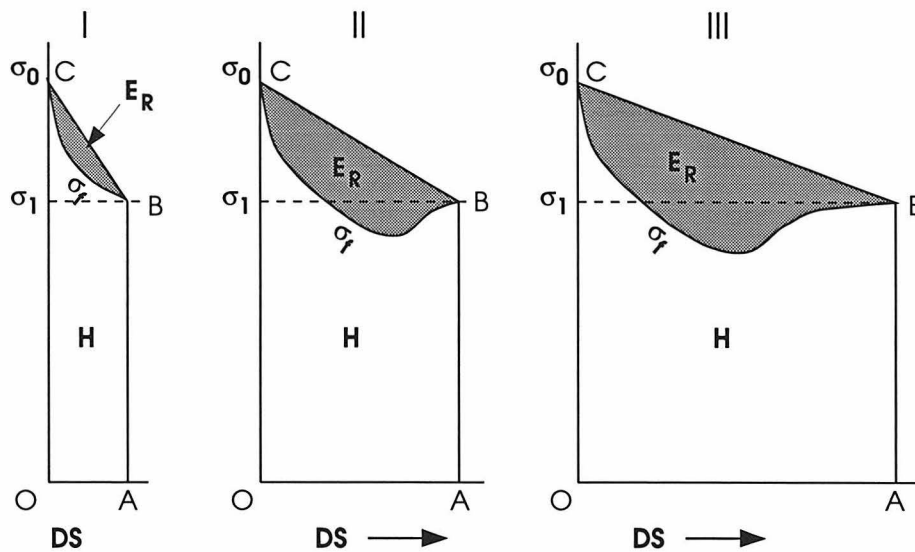


Fig 5. Model showing the moment dependence of frictional stress. The shaded area represents the radiated energy. The total energy is the area enclosed by OABC. In case I, the dynamic stress drop is smaller than the static stress drop, in case II both stress drops are equal, and for the largest event, case III, the dynamic stress drop is larger than the static stress drop.

crack energy in the form of  $\Delta\sigma_C$ . The surface areas between the various stress curves correspond to the different energies, and if  $G_C$  is constant the energy lost to crack formation becomes negligible if  $DS$  (and therefore the earthquake moment) increases. Likewise, for small earthquakes,  $\Delta\sigma_C$  will dominate energy. The decrease of the fracture energy relative to the elastic energy leads to a non-linear relationship between moment and radiated energy. However, it is not possible to explain the slope of the curve in figure 1 over such a magnitude range with a single value for the specific fracture energy. It is possible that the specific crack energy increases with moment, if one assumes that ruptures are limited by barriers and that large earthquakes must overcome barriers that are strong enough to arrest small earthquakes. In that case the average specific fracture energy increases as the size of the earthquakes increases. In figure 4b we plotted the situation where  $\Delta\sigma_C$  is constant so that (following eq.7)  $G_C$  increases.

The frictional stress is very difficult to determine and theoretical estimates are highly model-dependent. Kikuchi (1992) concluded that the frictional stress is high and decreases

as the total stress decreases during rupture. His conclusion is based on the fact that his estimates of the dynamic stress drop are much lower than the static stress-drop. Other authors (e.g. Brune, 1970; Heaton, 1990) have concluded the opposite, viz. that the frictional stress is actually lower than the final stress, so that the dynamic stress drop is higher than the static stress drop. Their conclusions are based on observation of high seismic energy radiation and on short slip durations observed in the field during rupture. The frictional stress is not a static variable. In physically realistic models it varies between the initial stress at the onset of rupture, to the final stress when the rupture stops. For instance, if we assume that the frictional stress drops with a finite slope instead of instantaneously, we could actually introduce a size dependence to the average frictional stress. In this model (fig 5), when a large earthquake occurs the frictional stress drops below the final stress as the dislocation progresses, reaching some minimum value after which it increases until the dislocation terminates. If a smaller earthquake were to exhibit the same initial frictional stress path, then the average frictional stress would be smaller because the dislocation would have terminated before the frictional stress ever dropped below the final stress value. This could even lead to  $\Delta\sigma_{1f}$  to be negative for small earthquakes. Such behaviour is similar to that proposed by Kikuchi (1992) to explain the low dynamic stress drops that he observed. Such a decrease of friction with progressive slip could be the result of heat generation. Although melting does not seem to occur on a significant scale during earthquakes, it is possible that an increase in pore pressure reduces the normal stress and thus the friction on a fault.

Heaton (1990) and Madariaga and Cochard (1994), among others, have proposed slip models where the friction depends in a non-linear way on the slip rate. The latter have shown that such a friction law in conjunction with asperities can lead to self-healing slip pulses. In their model, the stress on the fault drops instantaneously to a minimum value, at a maximum slip rate, which is determined by the friction law, after which the slip rate decreases and the frictional stress increases until some critical stress (the final stress  $\sigma_1$ ) is

---

reached at which the rupture stops. Although it hasn't been tested, it is possible that this kind of frictional behaviour results in a dynamical non-similarity between different size earthquakes, in a similar way as presented in figure 5.

### References:

- Abercrombie, R.E., 1995. Earthquake source scaling relationships from -1 to 5  $M_L$  using seismograms recorded at 2.5 km depth. *J. Geoph. Res.*, submitted.
- Aki, K., 1979. Characterization of barriers on an earthquake fault. *J. Geoph. Res.*, 84, 6140 - 6148.
- Brune, J.N., 1970. Tectonic stress and the spectra of seismic shear waves from earthquakes. *J. Geoph. Res.*, 75, no. 26, 4997-5009.
- Boatwright, J., Fletcher, J.B., Fumal, T., 1991. A general inversion scheme for source, site and propagation characteristics using multiply recorded sets of moderate-sized earthquakes. *Bull. Seis. Soc. Am.*, 81, no 5, 1754-1782.
- Fletcher, J.B., Boatwright, J., 1991. Source parameters of Loma Prieta aftershocks and wave propagation characteristics along the San Francisco peninsula from a joint inversion of digital seismograms. *Bull. Seis. Soc. Am.*, 81, no 5, 1783-1812.
- Heaton, T.H., 1990. Evidence for and implications of self-healing pulses of slip in earthquake rupture. *Phys. Earth Plan. Int.*, 64, 1-20.
- Husseini, M.I., 1977. Energy balance for crack formation along a fault. *Geoph. J. R. Astron. Soc.*, 49, 699 - 714.
- Kanamori, H., Mori, J., Hauksson, E., Heaton, T.H., Hutton, L.K., Jones, L.M., 1993. Determination of earthquake energy release and  $M_L$  using TERRAScope. *Bull. Seis. Soc. Am.*, 83, no. 2, 330 - 346.
- Kikuchi, M., 1992. Strain drop and apparent strain for large earthquakes. *Tectonophysics*,
-

---

211, 107 - 113.

Kikuchi, M., Fukao, Y., 1988. Seismic wave energy inferred from long-period body wave inversion. *Bull. Seis. Soc. Am.*, 78, 1707-1724.

Kostrov, B.V., Das, S., 1988. Principles of earthquake source mechanics. *Cambridge University Press*, Cambridge, England, 286pp.

Madariaga, R., Cochard, A., 1994. Seismic source dynamics, heterogeneity and friction. *Ann. di Geof.*, 37, no 6, 1349-1375.

Ruff, L.J., Miller, A.D., 1994. Rupture process of large earthquakes in the Northern Mexico subduction zone. *Pageoph.*, 142, no 1, 101-171.

Singh, S.K., Ordaz, M., 1994. Seismic energy release in Mexican subduction zone earthquakes. *Bull. Seis. Soc. Am.*, 84, no 5, 1533-1550.

Thatcher, W., Hanks, T.C., 1973. Source parameters of Southern California earthquakes. *J. Geoph. Res.*, 78, no 35, 8547-8576.

Thio, H.K., Kanamori, H., 1995a. Moment tensor inversions for local earthquakes using surface waves recorded at TERRAScope. *Bull. Seis. Soc. Am.*, in press.

Thio, H.K., Kanamori, 1995b. Source complexity of the Northridge earthquake and its relation to aftershock mechanisms. *Bull. Seis. Soc. Am.*, submitted.

Thio, H.K., Kanamori, H., 1995c. Source complexity of large strike-slip earthquake: the 1990 Rudbar (Iran), Luzon (Philippines) and 1992 Landers earthquake. in prep.

---

## Appendix A.

Moment tensor solution for events during the years 1990 to 1995. Epicentral coordinates, origin times and local magnitudes ( $M_L$ ) were supplied by the Southern California Seismic Network. An up-to-date list of these solutions is accessible via the World-Wide-Web with the following link: "<http://www.gps.caltech.edu/terrascope/TerraMech.html>".

---

Date	Time	Moment		Mw	ML	Strike	Dip	Slip	Lat.	Lon.	Dep.
		exp									
12/17/90	17:44:21.2	2.4	21	3.5		-154.	56.	11.	34.21	-117.02	
12/18/90	16:56:43.0	1.1	22	4.0		15.	81.	10.	35.37	-118.85	15.
06/28/91	14:43:54.3	3.3	24	5.6		253.	52.	89.	34.26	-118.00	11.
06/28/91	15:37:58.8	4.1	21	3.7		27.	58.	29.	34.25	-117.98	20.
06/28/91	17:00:55.0	2.7	22	4.2		-110.	51.	65.	34.26	-118.00	10.
06/29/91	17:53:52.0	4.0	21	3.7		-115.	68.	-3.	34.91	-116.58	
07/05/91	17:41:57.1	4.8	21	3.7		-47.5	51.	101.	34.50	-118.55	10.
07/06/91	22:54:39.0	3.8	21	3.7		-126.	33.	58.	34.24	-118.00	
09/17/91	21:10:29.0	1.9	23	4.8		-60.	60.	125.	35.82	-121.33	4.
10/12/91	14:39:32.1	1.1	22	4.0		-109.	75.	-29.	33.89	-116.16	8.
10/27/91	20:54:05.8	1.8	21	3.4		-61.	37.	119.	33.67	-116.74	11.
12/03/91	17:54:37.0	8.4	23	5.2		25.	76.	350.	31.81	-115.81	15.
12/04/91	07:10:57.0	8.9	21	3.9		-111.	89.	3.	33.07	-116.80	
12/04/91	08:17:03.0	4.2	21	3.7		61.	73.	31.	34.18	-117.02	11.
12/20/91	10:38:29.0	8.9	21	3.9		-124.	60.	-14.	35.54	-117.35	7.
02/19/92	11:19:24.0	7.0	21	3.8		7.	67.	204.	36.03	-117.88	2.
02/19/92	12:24:39.9	2.6	21	3.5		-179.	88.	-152.	36.03	-117.88	4.
02/22/92	03:32:20.0	1.9	21	3.5	3.86	-173.	74.	178.	36.06	-117.82	5.
02/21/92	04:17:54.0	2.0	22	3.5		-103.	56.	-41.	36.01	-117.90	4.
03/03/92	08:07:48.4	3.1	21	3.6	3.77	178.	30.	149.	35.77	-118.03	7.
03/04/92	19:06:27.0	1.6	22	4.1		-99.	50.	56.	32.96	-118.80	
03/05/92	18:24:22.8	3.9	21	3.7	3.83	-107.	38.	82.	35.22	-119.37	23.
03/17/92	11:56:35.0	4.6	21	3.7	3.78	74.	89.	347.	36.00	-117.88	5.
04/10/92	20:13:23.0	4.0	21	3.7		-79.	54.	141.	33.39	-116.31	
04/15/92	19:05:47.2	1.0	21	3.3	3.42	-146.	69.	-11.	34.29	-117.57	7.
04/23/92	02:25:30.1	3.1	22	4.3	4.60	76.	86.	20.	33.94	-116.33	12.
04/23/92	04:50:22.9	1.9	25	6.1	6.11	83.	78.	6.	33.95	-116.32	10.
04/23/92	13:35:58.1	1.0	22	3.9		-115.	52.	-13.	33.92	-116.32	4.
04/23/92	18:06:41.9	3.3	21	3.6		87.	85.	7.	33.94	-116.30	13.
04/23/92	18:20:13.0	4.0	21	3.7		-120.	69.	-34.	34.03	-116.33	4.
04/23/92	18:56:03.0	1.1	22	4.0	4.08	-104.	77.	-14.	33.97	-116.29	6.
04/23/92	22:55:56.9	3.5	21	3.6	3.76	36.	85.	4.	33.99	-116.34	13.
04/23/92	23:52:40.0	3.5	21	3.6	3.75	-101.	75.	-28.	33.98	-116.26	4.
04/24/92	03:29:59.0	2.3	21	3.5	3.53	-111.	65.	-30.	34.01	-116.34	4.
04/25/92	09:34:41.0	5.3	21	3.8	3.68	-110.	78.	-22.	33.95	-116.30	7.

Date	Time	Moment		M <sub>w</sub>	M <sub>L</sub>	Strike	Dip	Slip	Lat.	Lon.	Dep.
		exp									
04/26/92	03:07:57.0	1.9	21	3.4	3.68	-147.	56.	-50.	34.02	-116.31	15.
04/26/92	06:26:08.0	4.9	22	4.4	4.23	-114.	50.	-21.	33.92	-116.33	4.
04/26/92	17:21:38.0	2.5	22	4.2	4.28	74.	89.	354.	34.05	-116.34	8.
04/27/92	03:11:19.0	2.6	22	4.2	4.17	-134.	62.	-51.	33.91	-116.32	4.
04/28/92	11:13:20.6	7.9	21	3.9	3.73	-151.	48.	-71.	33.92	-116.32	5.
04/28/92	11:33:27.0	1.3	22	4.0	3.87	-143.	47.	-56.	33.95	-116.30	4.
04/30/92	01:50:44.0	5.0	21	3.7	3.69	-101.	55.	-19.	34.02	-116.09	5.
05/01/92	13:38:42.5	5.2	21	3.7	3.79	-140.	39.	-69.	33.92	-116.33	10.
05/02/92	12:46:42.0	4.4	21	3.7	4.09	70.	89.	330.	33.99	-116.41	5.
05/02/92	19:10:24.1	2.2	21	3.5	3.40	76.	80.	18.	33.96	-116.31	9.
05/04/92	01:16:02.4	1.1	22	4.0	3.97	-138.	43.	-24.	33.93	-116.36	9.
05/04/92	16:19:49.9	1.5	23	4.7	4.75	79.	84.	359.	33.92	-116.32	12.
05/06/92	02:38:43.0	7.4	22	4.5	4.59	-104.	24.	-12.	33.92	-116.34	10.
05/12/92	02:31:29.0	3.9	22	4.3	4.35	-105.	83.	-20.	33.96	-116.28	9.
05/18/92	00:22:34.0	2.5	21	3.5	3.46	-135.	40.	-30.	33.95	-116.36	11.
05/18/92	15:44:17.8	1.3	23	4.7	4.87	-126.	40.	-23.	33.95	-116.35	
05/31/92	10:53:16.0	6.0	20	3.1		-114.	59.	2.	34.59	-116.82	13.
05/31/92	11:38:45.0	1.8	21	3.4		-101.	63.	12.	34.57	-116.85	13.
06/11/92	00:24:19.0	2.0	22	4.1		9.	47.	190.	34.16	-116.30	
06/28/92	12:36:41.0	1.2	24	5.3	5.26	-112.	72.	-28.	34.10	-116.38	16.
06/28/92	14:43:22.0	9.4	23	5.2	5.42	-76.	37.	130.	34.16	-116.85	11.
06/28/92	15:05:30.0	4.5	25	6.4	6.31	46.	81.	7.	34.17	-116.81	12.
06/28/92	17:48:32.0	3.0	22	4.3	4.28	-144.	57.	-12.	34.23	-116.73	7.
06/28/92	19:42:16.0	3.1	21	3.6	3.6	2.	81.	142.	34.00	-116.50	1.
06/28/92	20:23:19.0	2.2	21	3.5	3.42	156.	69.	-124.	34.07	-116.39	26.
06/28/92	22:13:11.0	5.3	21	3.7	3.90	48.	86.	25.	34.07	-116.38	9.
06/29/92	10:14:22.0	2.8	24	5.6		179.	36.	-135.	36.60	-116.30	12.
06/29/92	14:08:38.0	2.3	23	4.8		61.	60.	2.	34.11	-116.40	21.
06/29/92	14:13:38.0	1.1	24	5.3		56.	71.	352.	34.11	-116.40	17.
06/29/92	14:31:30.0	2.1	22	4.2	4.5	-165.	57.	-103.	34.09	-116.35	8.
06/29/92	14:41:26.0	8.3	22	4.5		-158.	76.	-5.	34.12	-117.00	11.
06/29/92	16:01:43.0	2.0	24	5.5		70.	85.	19.	33.86	-116.30	7.
06/29/92	19:10:31.0	5.1	21	3.7		-98.	89.	8.	33.85	-116.29	11.
06/29/92	22:52:16.0	9.1	21	3.9	3.70	92.	52.	15.	34.17	-118.18	1.
06/30/92	00:23:56.0	4.0	21	3.7		152.	63.	-134.	34.14	-116.45	10.

Date	Time	Moment		Mw	M <sub>L</sub>	Strike	Dip	Slip	Lat.	Lon.	Dep.
		exp									
06/30/92	05:33:47.0	5.9	21	3.8		-138.	44.	-12.	34.26	-116.69	10.
06/30/92	11:30:29.0	1.5	22	4.0	4.31	73.	87.	10.	34.07	-116.45	18.
06/30/92	12:14:50.0	9.5	21	3.9	4.1	45.	81.	356.	34.05	-116.47	16.
06/30/92	12:26:19.0	3.9	21	3.7	3.59	-131.	78.	-35.	34.01	-116.36	4.
06/30/92	12:34:55.0	4.9	21	3.7	4.12	-51.	43.	143.	34.26	-116.47	4.
06/30/92	13:05:36.0	1.0	23	4.6	4.48	29.	88.	354.	35.68	-117.61	5.
06/30/92	14:38:11.0	5.7	23	5.1	4.98	-45.	43.	112.	34.00	-116.37	15.
06/30/92	17:26:30.0	1.2	22	4.0	4.26	-177.	53.	-108.	34.64	-116.68	5.
06/30/92	20:05:06.0	7.5	21	3.9	3.89	-154.	57.	-85.	33.98	-116.37	4.
06/30/92	21:22:54.0	6.7	22	4.5	4.70	-136.	81.	-7.	34.13	-116.73	7.
06/30/92	21:49:01.0	7.5	22	4.5	4.34	-42.	45.	125.	34.06	-116.99	1.
07/01/92	00:14:27.0	7.6	21	3.9	3.46	6.	81.	345.	34.09	-116.98	13.
07/01/92	17:45:52.0	1.1	22	4.0		-84.	66.	64.	33.93	-116.71	8.
07/02/92	05:16:34.0	4.9	21	3.7	3.83	76.	58.	26.	34.34	-116.51	6.
07/02/92	12:17:42.0	1.2	21	3.3	3.48	-112.	39.	165.	34.61	-116.58	11.
07/02/92	15:11:58.0	3.8	20	3.0	3.22	46.	71.	13.	34.03	-116.35	13.
07/02/92	18:53:51.0	1.5	21	3.4		-109.	42.	106.	34.05	-116.58	13.
07/02/92	22:25:27.0	8.8	21	3.9	4.14	36.	71.	358.	35.77	-117.59	7.
07/03/92	02:40:52.0	3.5	21	3.6	3.52	-60.	67.	107.	33.16	-115.65	11.
07/03/92	04:10:49.0	7.9	20	3.2		52.	78.	11.	34.17	-116.35	9.
07/03/92	04:15:51.0	2.7	21	3.6	3.94	78.	60.	215.	34.18	-116.78	15.
07/03/92	04:19:41.0	9.9	20	3.3		-175.	42.	-86.	34.22	-116.64	11.
07/03/92	05:55:43.0	8.3	20	3.2	3.20	69.	53.	345.	34.01	-116.36	2.
07/03/92	10:40:08.0	3.1	21	3.6	3.68	20.	86.	18.	34.20	-116.86	13.
07/03/92	11:40:28.0	1.2	21	3.3		-118.	75.	1.	33.91	-116.38	8.
07/03/92	12:32:24.0	8.8	20	3.2	3.40	-143.	35.	-33.	34.63	-116.51	7.
07/03/92	17:17:02.0	6.6	21	3.8		39.	81.	4.	34.40	-116.56	16.
07/04/92	09:36:01.0	1.4	21	3.4	3.42	51.	82.	10.	34.30	-116.83	19.
07/05/92	05:49:39.0	1.4	22	4.0	3.85	-154.	49.	-86.	33.95	-116.39	5.
07/05/92	10:36:19.0	2.6	21	3.5		-131.	76.	-38.	34.61	-116.33	7.
07/05/92	10:55:45.0	3.2	22	4.3	4.57	-115.	80.	-9.	35.03	-116.98	9.
07/05/92	21:18:27.0	1.1	24	5.3	5.5	76.	72.	34.	34.58	-116.32	8.
07/05/92	22:33:47.0	3.5	22	4.3	4.25	-37.	50.	114.	34.57	-116.33	9.
07/06/92	12:00:58.0	2.8	22	4.2	4.36	-117.	82.	-29.	34.08	-116.31	8.
07/06/92	19:41:37.0	3.0	22	4.3	4.34	64.	78.	356.	34.07	-116.34	16.

Date	Time	Moment		Mw	ML	Strike	Dip	Slip	Lat.	Lon.	Dep.
		exp									
07/08/92	02:23:10.0	7.1	22	4.5	4.70	79.	77.	36.	34.57	-116.30	8.
07/09/92	01:43:58.0	9.5	23	5.3	4.88	-123.	47.	61.	34.23	-116.84	1.
07/10/92	01:29:41.0	3.6	22	4.3	4.12	-120.	37.	37.	34.24	-116.85	1.
07/10/92	02:41:15.0	1.4	22	4.0	3.92	127.	89.	266.	34.12	-116.40	2.
07/10/92	16:01:38.0	1.2	21	3.3	3.34	23.	88.	219.	34.48	-116.51	12.
07/11/92	07:21:37.0	6.2	21	3.8		-124.	84.	-72.	34.45	-116.50	1.
07/11/92	18:14:17.0	6.7	23	5.1		-147.	86.	-32.	35.21	-118.07	24.
07/12/92	05:35:14.0	5.2	21	3.7	3.77	173.	72.	-97.	34.51	-116.57	4.
07/13/92	05:00:01.0	2.0	21	3.5	3.64	-175.	46.	-103.	34.09	-116.41	11.
07/14/92	20:36:52.0	7.0	21	3.8	3.62	-27.	6.	5.	34.64	-116.65	1.
07/15/92	00:18:57.0	5.5	21	3.8	3.81	28.	53.	28.	34.34	-116.45	3.
07/15/92	12:45:22.0	2.8	21	3.6	3.57	-140.	68.	-57.	34.13	-116.37	8.
07/20/92	04:08:24.0	7.7	21	3.9	3.94	-135.	60.	-6.	34.20	-116.45	8.
07/20/92	04:48:02.0	5.3	22	4.4	4.40	-98.	83.	-15.	34.96	-116.95	9.
07/20/92	13:13:21.0	5.7	22	4.4	4.51	-112.	53.	-17.	34.98	-116.96	3.
07/24/92	18:14:37.0	2.5	23	4.9	4.74	-105.	84.	-28.	33.90	-116.28	8.
07/24/92	07:23:57.0	3.7	21	3.6	3.86	-163.	65.	-59.	34.48	-116.50	15.
07/25/92	04:32:00.0	1.5	23	4.7	4.67	-99.	32.	21.	33.94	-116.30	8.
07/25/92	17:02:19.	2.1	21	3.5		-93.	54.	4.	33.94	-116.31	15.
07/27/92	20:40:09.0	3.9	21	3.7	3.93	-138.	90.	29.	32.67	-115.62	2.
07/28/92	18:27:04.0	1.7	23	4.8	4.35	84.	76.	27.	34.09	-116.37	15.
08/04/92	19:06:12.0	1.0	22	3.9	3.76	64.	65.	345.	34.10	-116.38	3.
08/05/92	15:41:54.0	6.7	21	3.8	3.89	-165.	37.	-31.	34.67	-116.53	22.
08/08/92	15:37:43.0	2.5	22	4.2	4.23	-101.	71.	-15.	34.37	-116.45	7.
08/11/92	06:11:17.0	1.1	22	4.0	3.99	71.	67.	3.	34.06	-116.37	9.
08/15/92	18:18:05.0	5.4	21	3.8	3.49	-128.	73.	-12.	34.10	-116.99	4.
08/16/92	06:30:59.0	3.0	21	3.6	3.59	-86.	28.	115.	34.03	-116.68	11.
08/17/92	20:41:51.0	1.8	23	4.8	4.23	-102.	37.	107.	34.18	-116.87	15.
08/18/92	09:46:40.0	9.9	21	3.9	4.08	-100.	51.	98.	34.18	-116.86	4.
08/23/92	06:40:44.0	6.2	21	3.8	3.86	67.	85.	22.	35.02	-117.00	8.
08/24/92	13:51:46.0	1.8	22	4.1	4.13	-113.	86.	-30.	34.28	-116.78	8.
08/24/92	18:21:42.0	8.3	20	3.2	3.39	14.	78.	11.	34.28	-116.78	6.
08/26/92	13:21:56.0	5.0	21	3.7		73.	75.	8.	34.06	-116.36	4.
08/26/92	13:50:48.0	1.1	21	3.3	3.32	-117.	55.	-7.	34.11	-116.98	5.
08/30/92	08:15:12.0	2.6	21	3.5	3.36	-61.	50.	70.	34.01	-118.36	10.

Date	Time	Moment		Mw	M <sub>L</sub>	Strike	Dip	Slip	Lat.	Lon.	Dep.
		exp									
08/31/92	09:25:39.0	1.5	22	4.1	4.23	-115.	62.	-50.	34.50	-116.43	14.
09/03/92	06:17:38.0	2.5	21	3.5	3.63	2.0	76.	170.	34.38	-116.44	13.
09/05/92	03:29:27.0	3.6	21	3.6	3.79	35.	59.	18.	34.11	-116.40	9.
09/06/92	22:47:29.0	1.3	21	3.4	3.36	-128.	83.	-40.	35.03	-116.98	8.
09/08/92	03:44:49.0	6.5	21	3.8		-131.	65.	-2.	34.11	-116.98	7.
09/09/92	11:44:55.0	1.0	22	3.9	4.03	-119.	52.	8.	35.07	-116.99	2.
09/09/92	12:50:44.0	2.0	22	4.1	4.16	-127.	40.	4.	33.94	-116.33	8.
09/11/92	18:58:22.0	1.9	21	3.4	3.57	68.	87.	8.	35.03	-116.98	9.
09/15/92	08:47:11.0	8.0	23	5.2		63.	86.	11.	34.06	-116.37	11.
09/16/92	12:27:22.0	3.3	21	3.6	3.58	50.	85.	14.	34.06	-116.38	9.
09/18/92	12:53:35.0	7.3	21	3.8	3.72	-134.	80.	-47.	34.05	-116.38	8.
09/22/92	18:52:33.0	9.9	21	3.9	3.93	-134.	80.	-47.	34.05	-116.38	8.
10/02/92	07:19:57.0	4.2	22	4.4		-98.	72.	152.	34.61	-116.64	5.
10/11/92	12:38:13.0	4.1	22	4.3	4.37	-116.	88.	3.	34.93	-116.82	12.
10/20/92	05:28:09.0	5.7	22	4.4		52.	84.	349.	35.93	-120.47	13.
11/24/92	09:06:26.0	4.6	21	3.7		-150.	59.	-10.	34.14	-116.88	13.
11/25/92	02:40:25.0	4.3	21	3.7		-121.	82.	22.	35.04	-116.96	12.
11/25/92	07:50:35.0	9.7	21	3.9		-23.	29.	-179.	34.15	-116.43	2.
11/27/92	16:00:57.0	6.4	23	5.1	5.35	-146.	80.	24.	34.34	-116.89	3.
12/04/92	12:59:42.0	1.7	22	4.1		-50.	55.	137.	34.35	-116.90	1.
03/20/93	06:56:55.0	4.1	21	3.7		-176.	67.	-106.	34.01	-117.23	11.
04/29/93	08:21:01.0	1.1	24	5.3		-79.	73.	-96.	35.60	-112.10	8.
05/17/93	23:20:50.0	1.6	25	6.1		-173.	48.	-110.	37.20	-117.77	9.
05/18/93	23:48:55.0	4.1	23	5.0		84.	24.	13.	37.06	-117.76	5.
05/18/93	17:09:05.0	2.3	21	3.5		-76.	51.	80.	34.29	-117.48	12.
05/19/93	14:13:24.0	1.8	23	4.8		-179.	74.	-101.	37.14	-117.73	5.
05/20/93	20:14:14.0	1.4	23	4.7		33.	38.	347.	36.09	-117.69	1.
05/28/93	04:47:40.0	1.8	23	4.8		-149.	37.	-6.	35.13	-119.10	21.
05/31/93	08:55:30.0	2.4	22	4.2		-111.	42.	81.	34.12	-116.99	7.
07/26/93	21:29:49.0	2.1	21	3.5		-82.	52.	113.	33.99	-118.74	18.
08/11/93	05:48:20.0	7.7	22	4.5		132.	50.	-120.	37.52	-118.89	6.
08/11/93	22:33:04.0	1.9	23	4.8		-131.	83.	18.	37.31	-121.68	6.
08/21/93	01:46:38.0	6.2	22	4.5		-134.	46.	-60.	34.03	-116.32	15.
09/06/93	08:25:23.0	8.3	21	3.9		-88.	35.	99.	34.14	-116.84	7.
09/06/93	10:32:33.0	2.4	21	3.5		-156.	42.	-50.	36.00	-118.37	5.

Date	Time	Moment exp		Mw	M <sub>L</sub>	Strike	Dip	Slip	Lat.	Lon.	Dep.
09/06/93	22:30:15.0	6.1	21	3.8		21.	85.	2.	32.51	-115.41	3.
10/04/93	02:57:37.0	3.9	21	3.7		-68.	50.	100.	34.02	-116.34	4.
10/13/93	09:54:03.0	6.4	21	3.8		157.	42.	124.	34.82	-120.95	6.
10/18/93	21:49:46.0	1.3	23	4.7	4.04	-111.	69.	30.	31.98	-118.86	5.
10/21/93	14:37:12.0	5.6	21	3.8		170.	39.	-112.	36.18	-118.03	3.
10/22/93	16:30:53.0	3.6	21	3.6	3.72	9.	65.	182.	36.10	-117.94	6.
10/25/93	00:18:50.0	2.1	21	3.5		-159.	47.	-66.	34.92	-116.85	4.
11/04/93	00:36:54.0	7.7	20	3.2	3.45	-125.1	33.	-51.	33.81	-115.66	9.
11/14/93	12:25:35.0	2.0	23	4.8		51.	89.	341.	35.95	-120.51	14.
12/03/93	01:51:25.0	3.1	21	3.6	3.67	-171.	66.	166.	34.26	-116.72	19.
01/09/94	23:00:59.0	6.6	21	3.8		-98.	48.	82.	33.99	-118.5	6.
01/17/94	12:30:55.0	1.6	26	6.7	6.45	-69.	58.	85.	34.21	-118.55	11.
01/17/94	17:56:08.0	7.0	22	4.5	4.51	-73	58.	76.	34.23	-118.57	17.
01/17/94	18:20:24.0	1.6	21	3.4	3.45	-67.	46.	77.	34.28	-118.46	9.
01/17/94	18:32:09.0	5.0	21.	3.7	3.70	-59.	30.	88.	34.29	-118.51	21.
01/17/94	19:23:54.0	2.1	21	3.5	3.6	-63.	24.	127.	34.28	-118.58	17.
01/17/94	19:43:53.0	2.5	22	4.2	3.94	-43.	30.	139.	34.38	-118.64	17.
01/17/94	19:58:48.0	4.8	21	3.7	3.56	-59.	9.	146.	34.47	-118.63	1.
01/17/94	20:02:05.0	4.9	21	3.7	3.80	-48.	22.	107.	34.40	-118.52	9.
01/17/94	20:05:28.0	5.6	21	3.8	3.71	-131.	51.	-20.	34.35	-118.49	5.
01/17/94	20:11:49.0	1.9	21	3.4	3.61	153.	68.	101.	34.32	-118.52	10.
01/17/94	20:17:38.0	1.5	21	3.4	3.43	-170.	44.	-50.	34.33	-118.52	5.
01/17/94	20:38:25.0	4.8	21	3.7	3.66	-87.	85.	68.	34.31	-118.46	20.
01/17/94	20:46:03.0	3.5	23	5.0	4.94	-116.	88.	5.	34.32	-118.56	11.
01/17/94	22:07:43.0	1.7	21	3.4	3.50	139.	48.	-150.	34.35	-118.47	5.
01/17/94	22:19:24.0	8.1	21	3.9	3.81	65.	61.	357.	34.35	-118.64	15.
01/17/94	23:33:31.0	8.2	24	5.9	5.27	-30.	40.	148.	34.33	-118.69	3.
01/18/94	00:39:35.0	4.0	22	4.3		-74.	28.	82.	34.38	-118.56	13.
01/18/94	00:43:09.0	4.0	23	5.0	5.2	-56.	54.	145.	34.38	-118.70	12.
01/18/94	04:01:27.0	6.0	22	4.4	4.19	90.	58.	33.	34.34	-118.63	1.
01/18/94	04:31:20.0	5.7	21	3.8	3.66	-138.	53.	46.	34.35	-118.44	14.
01/18/94	06:29:02.0	3.1	21	3.6	3.68	-84.	61.	69.	34.30	-118.44	14.
01/18/94	09:41:48.0	3.5	21	3.6	3.7	-37.	59.	129.	34.22	-118.52	16.
01/18/94	11:35:10.0	1.5	22	4.1	4.2	-116.	89.	2.	34.22	-118.60	4.
01/18/94	13:24:44.0	2.6	22	4.2	4.33	-107.	60.	2.	34.28	-118.57	4.

Date	Time	Moment exp		Mw	M <sub>L</sub>	Strike	Dip	Slip	Lat.	Lon.	Dep.
01/18/94	15:19:54.0	9.4	21	3.9	3.81	73.	82.	314.	34.21	-118.59	5.
01/18/94	15:23:47.0	1.7	23	4.8	4.69	-95.	49.	43.	34.30	-118.59	9.
01/18/94	16:23:35.0	5.7	21	3.8	3.79	67.	88.	324.	34.36	-118.56	5.
01/19/94	04:40:48.0	2.6	22	4.2	4.23	176.	78.	136.	34.37	-118.55	1.
01/19/94	14:09:15.0	4.8	22	4.4	4.38	-68.	21.	106.	34.23	-118.50	11.
01/19/94	14:46:35.0	4.5	21	3.7	4.0	-56.	49.	93.	34.30	-118.48	11.
01/19/94	21:09:28.0	8.5	23	5.2	4.97	-76.	34.	97.	34.37	-118.70	13.
01/19/94	21:11:43.0	2.5	23	4.9	5.06	-53.	29.	142.	34.37	-118.70	11.
01/21/94	18:39:15.0	7.5	22	4.5	4.46	2.	54.	151.	34.30	-118.46	17.
01/21/94	18:53:44.0	2.4	22	4.2	4.27	-69.	44.	70.	34.32	-118.48	13.
01/23/94	08:41:41.0	3.7	21	3.6	3.8	-44.	58.	98.	34.29	-118.46	14.
01/23/94	08:55:09.0	5.4	21	3.8	3.98	-100.	93.	1.	34.30	-118.32	5.
01/24/94	04:15:19.0	2.5	22	4.2	4.49	-129.	31.	1.	34.28	-118.57	5.
01/24/94	05:50:24.0	2.2	22	4.2	4.23	77.	86.	38.	34.36	-118.63	20.
01/24/94	05:54:21.0	1.7	22	4.1	4.12	75.	87.	29.	34.37	-118.63	20.
01/27/94	17:19:59.0	3.2	22	4.3	4.46	-36.	26.	-66.	34.27	-118.56	20.
01/28/94	20:09:53.0	3.5	22	4.3	4.05	-88.	76.	82.	34.37	-118.48	2.
01/29/94	11:20:34.6	6.3	23	5.1	5.1	65.	58.	1.	34.38	-118.67	9.
01/29/94	12:16:56.0	1.7	22	4.1	4.19	-126.	73.	-3.	34.28	-118.61	5.
02/03/94	16:23:32.0	1.4	22	4.0	4.2	-66.	54.	90.	34.33	-118.41	10.
02/04/94	06:33:40.0	4.0	21	3.7	3.50	-91.	49.	30.	34.28	-118.62	1.
02/04/94	00:10:12.0	7.7	21	3.9	4.1	41.	88.	325.	36.37	-117.08	14.
02/06/94	13:19:27.0	7.7	21	3.9	4.07	-27.	30.	128.	34.28	-118.49	11.
02/06/94	13:21:45.0	5.1	21	3.8	3.7	-32.	40.	123.	34.35	-118.50	9.
02/11/94	14:07:53.0	3.0	21	3.6	3.56	-47.	61.	101.	34.34	-118.48	9.
02/18/94	09:13:28.0	4.4	21	3.7	3.64	138.	42.	69.	34.24	-118.57	13.
02/25/94	12:59:13.0	7.3	21	3.8	3.97	-102.	63.	62.	34.36	-118.38	5.
03/10/94	12:44:15.0	1.2	21	3.3	3.53	50.	53.	349.	34.23	-118.47	5.
03/20/94	21:20:10.0	1.2	24	5.3	5.35	-52.	40.	106.	34.28	-118.42	14.
03/23/94	02:59:18.0	3.8	23	5.0	4.8	20.	61.	14.	31.92	-116.05	16.
04/06/94	19:01:04.0	5.5	22	4.4	4.83	23.	67.	7.	34.19	-117.10	10.
04/07/94	04:19:29.0	2.8	21	3.6	3.47	-104.	74.	48.	34.34	-118.46	9.
04/21/94	16:37:16.0	5.8	22	4.4		-53.	57.	89.	36.26	-120.45	13.
04/27/94	12:33:10.0	7.5	21	3.9	3.49	-43.	35.	98.	34.26	-118.74	14.
05/04/94	04:09:13.0	1.3	21	3.3	3.64	-104.	89.	30.	34.33	-118.45	6.

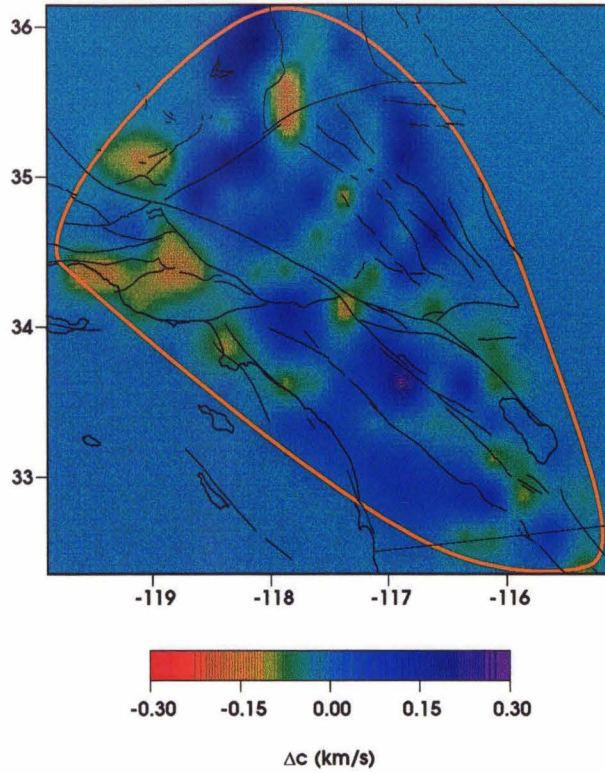
Date	Time	Moment		Mw	M <sub>L</sub>	Strike	Dip	Slip	Lat.	Lon.	Dep.
		exp									
05/16/94	08:40:47.0	2.9	21	3.6	3.73	-73.	35.	95.	34.31	-118.62	25.
05/25/94	12:56:57.0	4.6	22	4.4	4.18	-81.	31.	78.	34.31	-118.39	9.
05/28/94	17:15:12.0	4.3	21	3.7	3.60	71.	74.	40.	34.35	-118.68	20.
05/30/94	03:22:26.0	3.3	21	3.6	3.45	-157.	48.	-99	36.03	-117.85	5.
06/02/94	03:27:14.0	4.4	21	3.7	3.69	118.	50.	48.	34.27	-118.40	13.
06/08/94	09:02:29.0	1.5	21	3.4		162.	58.	64.	37.59	-118.85	1.
06/15/94	05:59:49.0	8.7	21	3.9	3.99	141.	43.	83.	34.31	-118.40	11.
06/16/94	16:24:28.0	1.5	23	4.7	4.91	-127.	69.	-7.	34.27	-116.41	6.
06/29/94	07:34:35.0	2.3	21	3.5	3.55	55.	63.	22.	34.27	-116.41	11.
07/11/94	06:50:50.0	5.8	21	3.8	3.72	-101.	56.	63.	34.26	-118.69	18.
08/01/94	21:34:31.0	4.3	23	4.4	4.77	-93.	80.	6.	34.64	-116.52	16.
08/07/94	15:10:26.0	1.2	22	4.0	4.00	-33.	41.	130.	33.99	-116.27	3.
08/11/94	02:22:54.0	2.4	22	4.2		168.	35.	-130.	32.40	-115.26	3.
08/19/94	06:56:10.0	3.4	21	3.6		-54.	30.	92.	34.26	-118.75	15.
12/06/94	03:36:24.0	4.0	21	3.7	3.58	-45.	55.	140.	34.30	-118.38	10.
12/06/94	03:48:35.0	3.4	22	4.3	4.30	-36.	45.	149.	34.29	-118.39	10.
12/12/94	13:05:31.0	5.9	21	3.8	3.66	131.	77.	-123.	33.17	-115.56	1.
04/04/95	05:08:16.0	2.4	21	3.5		-14.	56.	141.	34.27	-117.47	16.

## **Appendix B.**

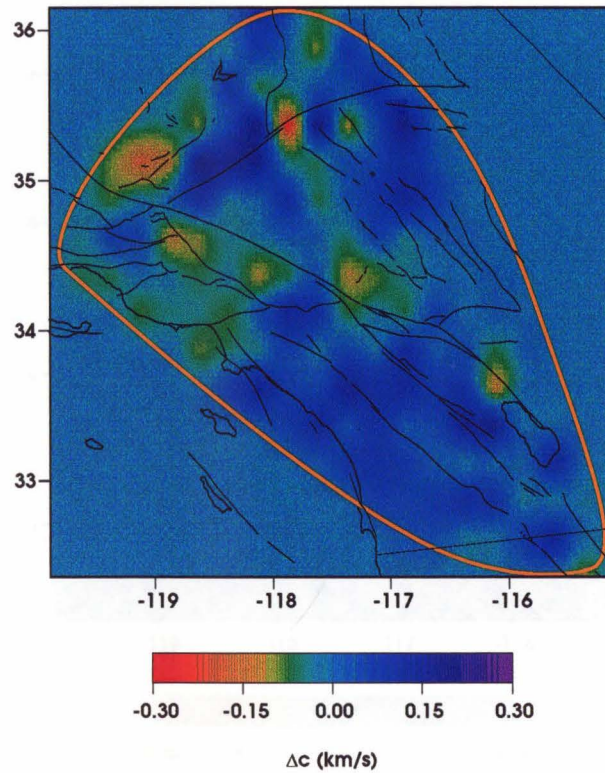
Maps of lateral phase velocity variations in Southern California. The orange line is the boundary of the area which is covered by our data.

---

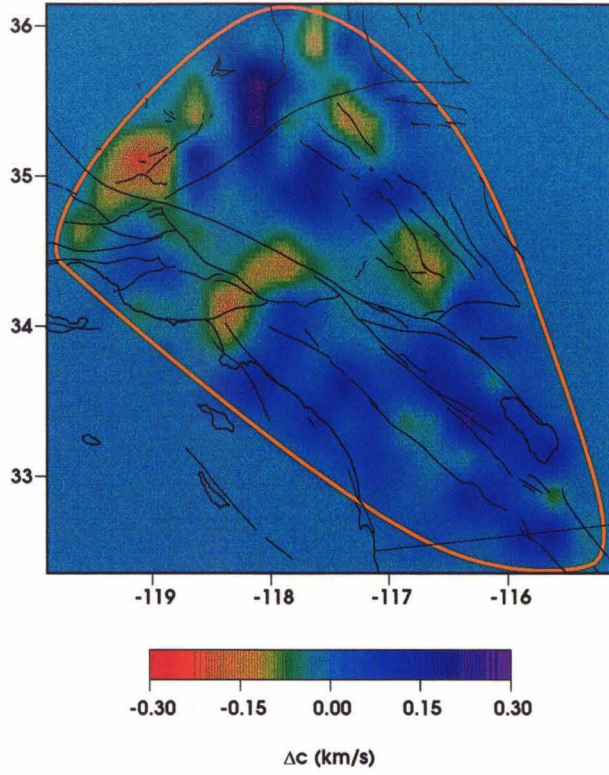
Rayleigh waves: T=10.24 sec



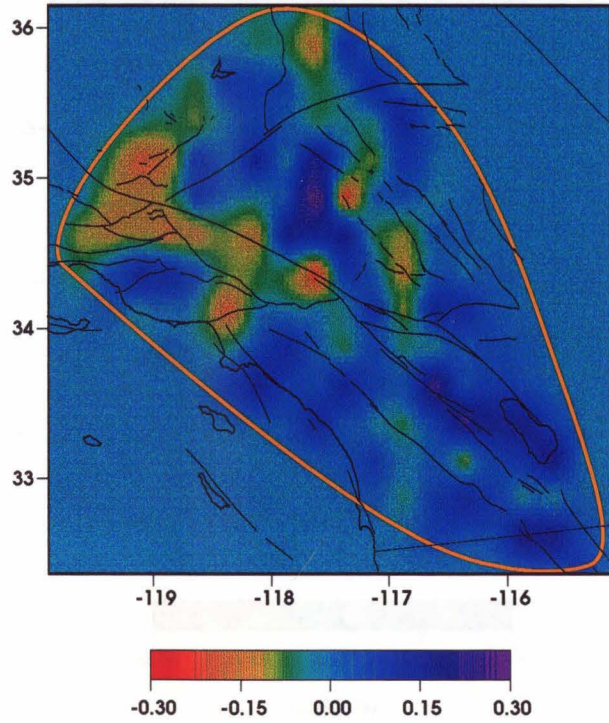
Rayleigh waves: T=11.38 sec



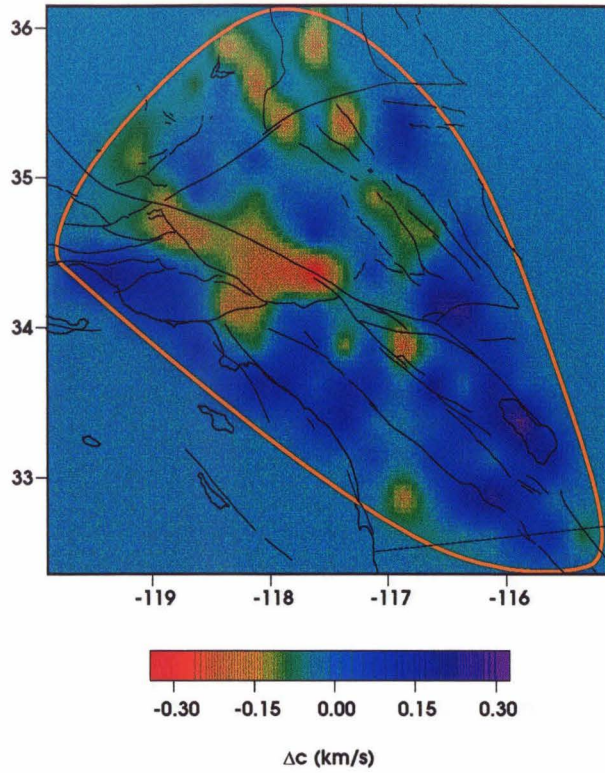
Rayleigh waves: T=12.80 sec



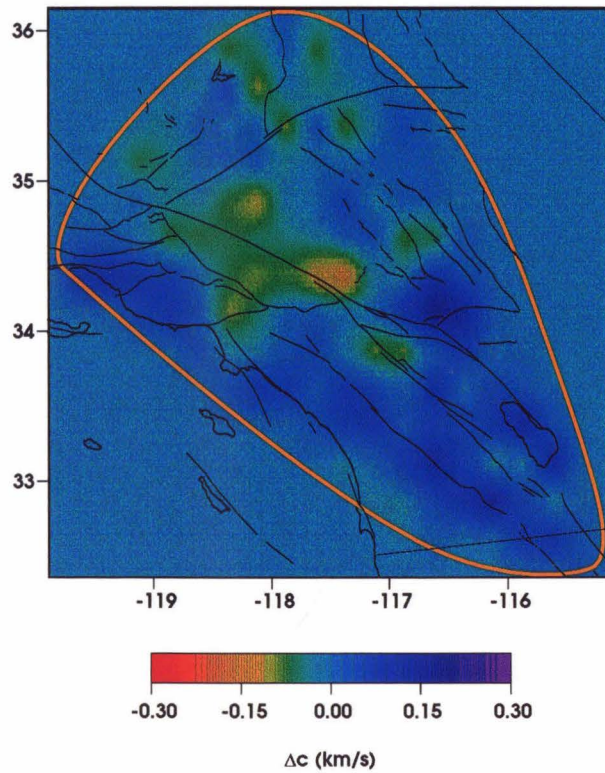
Rayleigh waves: T=14.63 sec



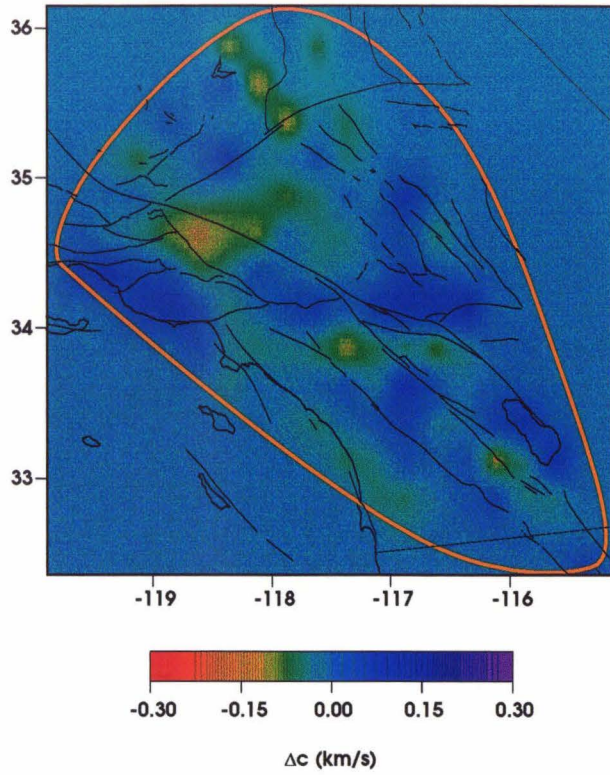
Rayleigh waves: T=17.07 sec



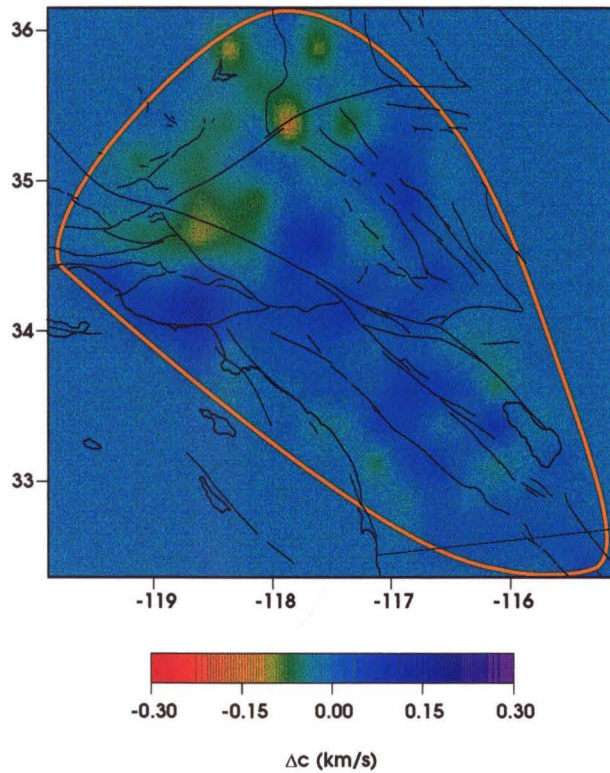
Rayleigh waves: T=20.48 sec



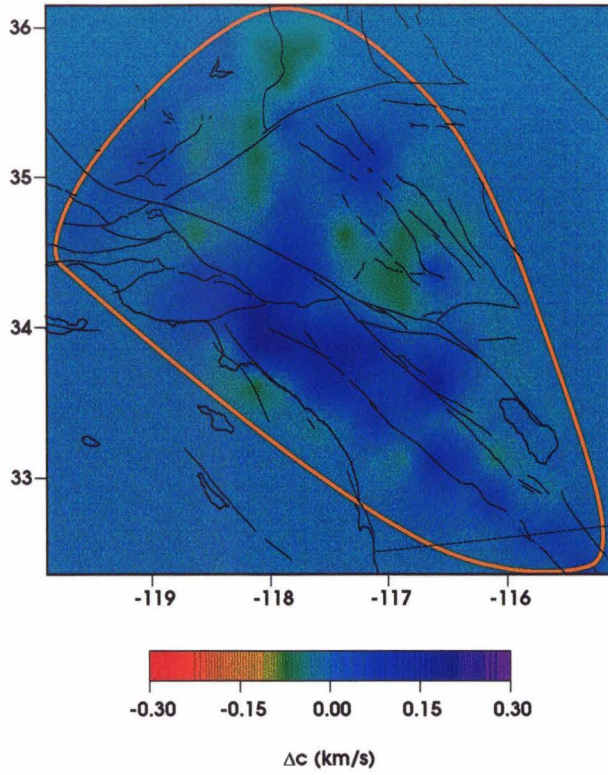
Rayleigh waves: T=25.60 sec



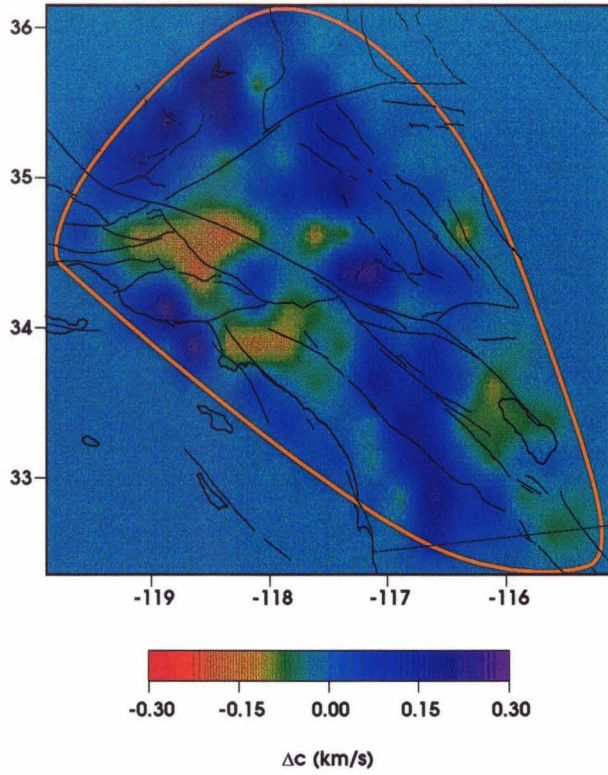
Rayleigh waves: T=34.13 sec



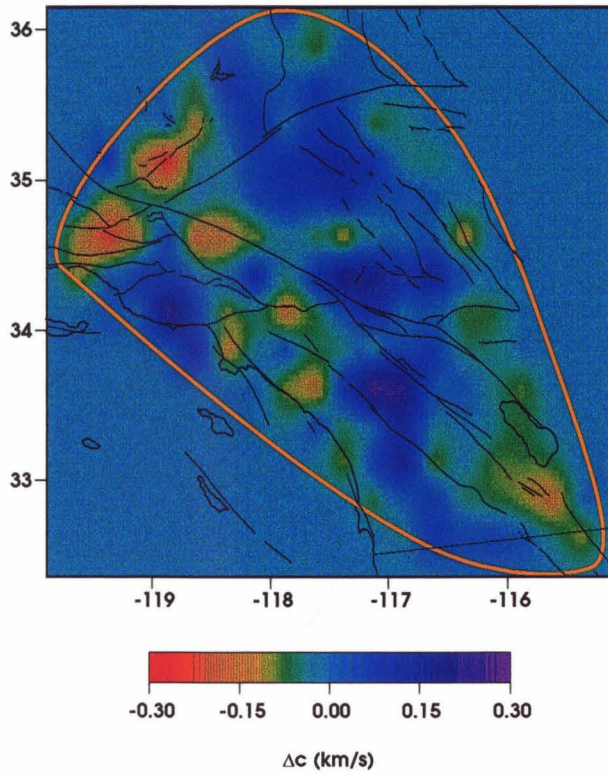
Rayleigh waves: T=51.20 sec

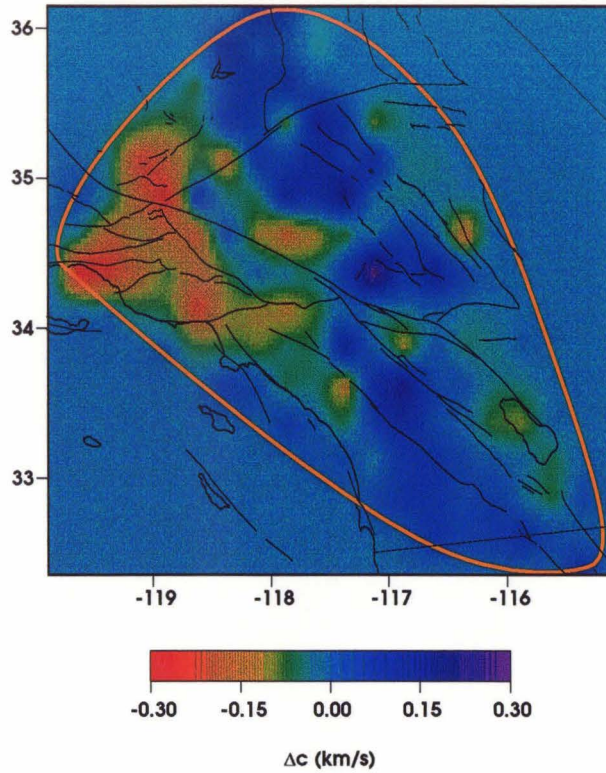
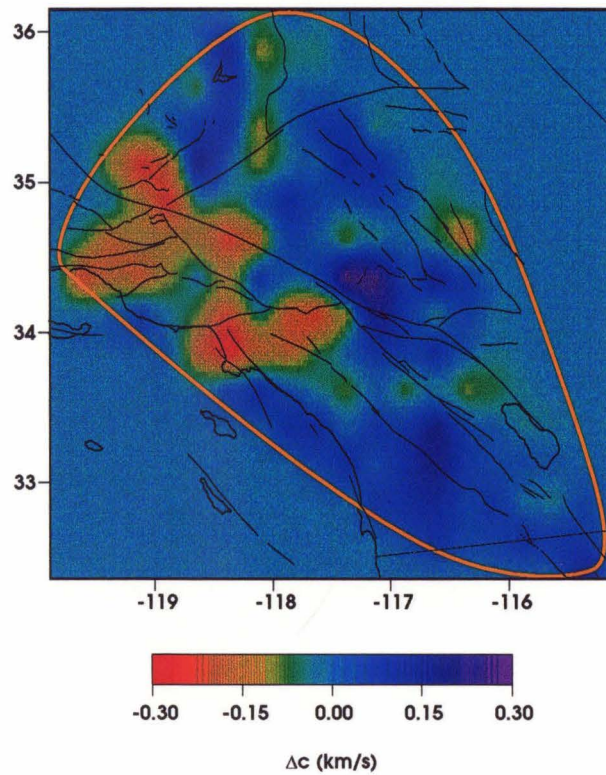


Love waves: T=10.24 sec

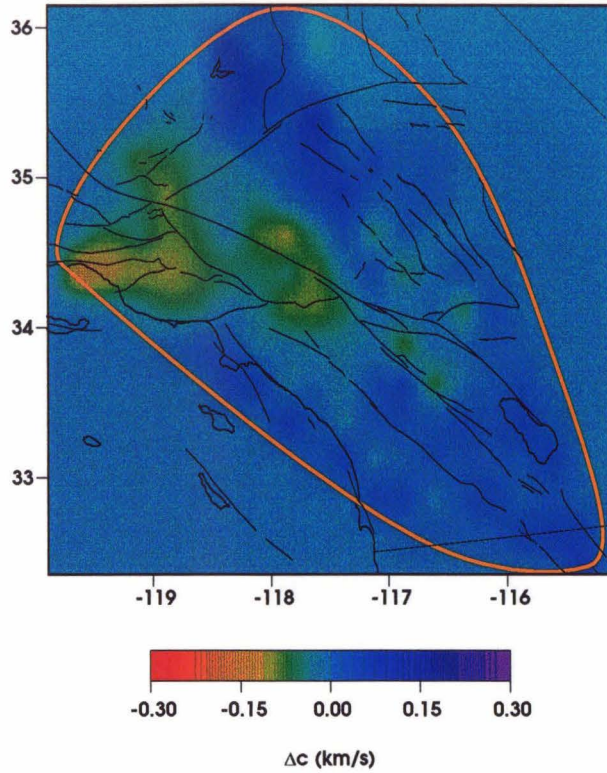


Love waves: T=11.38 sec

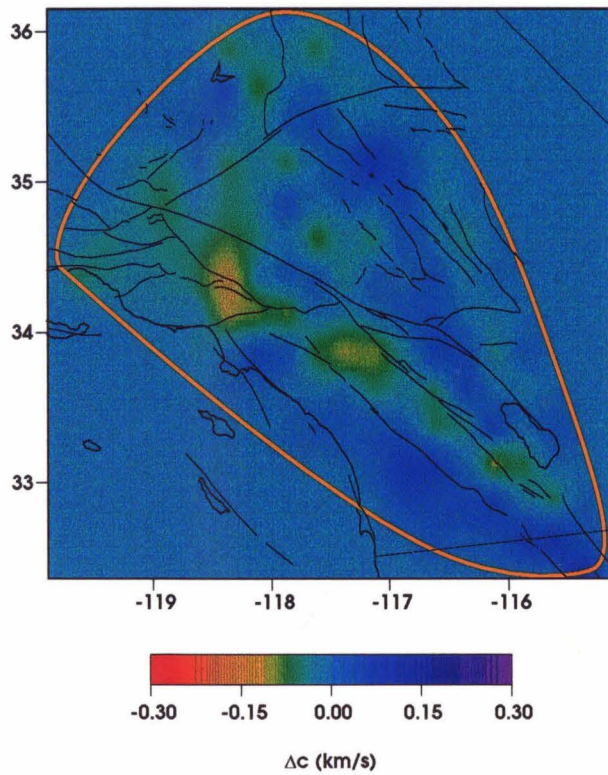


Love waves:  $T=12.80$  secLove waves:  $T=14.63$  sec

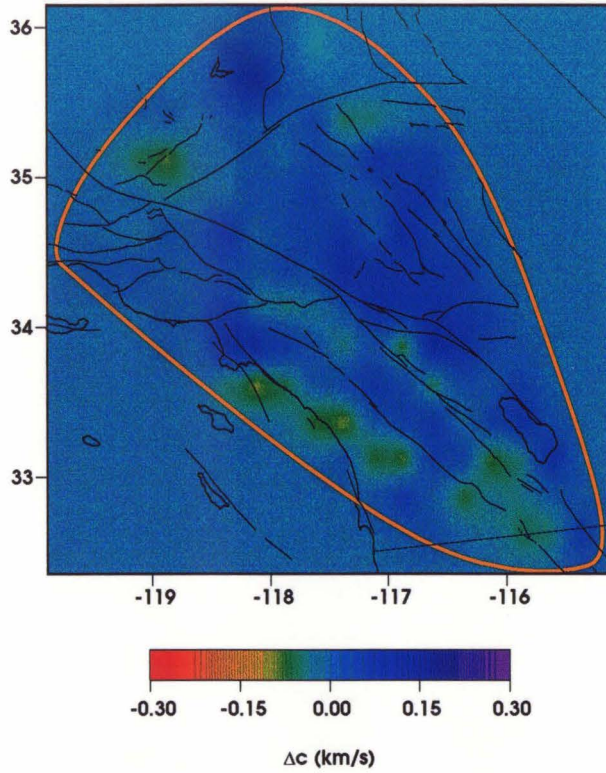
Love waves: T=17.07 sec



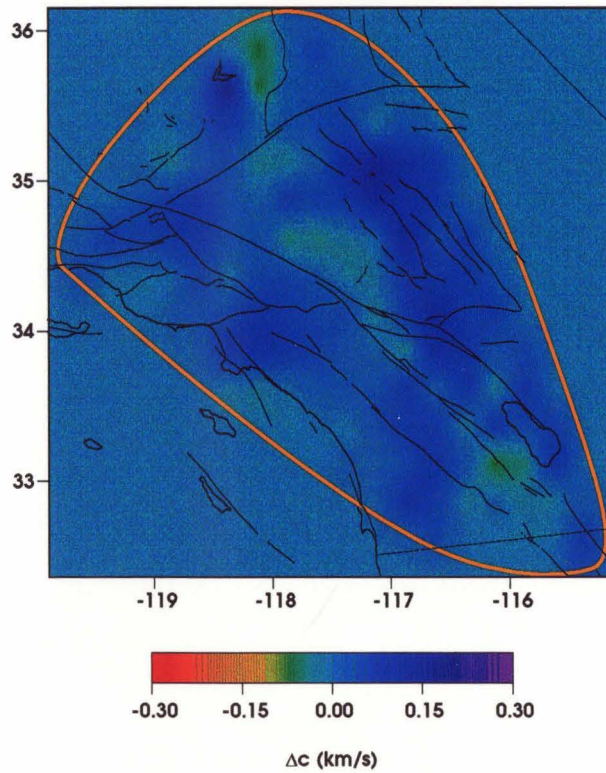
Love waves: T=20.48 sec



Love waves: T=25.60 sec



Love waves: T=34.13 sec



Love waves: T=51.20 sec

